Imaging Magnetic Nanostructures using Soft X-ray Fourier Transform Holography

vorgelegt von
Diplom-Physiker
Bastian Pfau
aus Frankfurt (Oder)

Von der Fakultät II – Mathematik und Naturwissenschaften
der Technischen Universität Berlin
zur Erlangung des akademischen Grades

Doktor der Naturwissenschaften
– Dr. rer. nat. –

genehmigte Dissertation

Promotionsausschuss:

Vorsitzender: Prof. Dr. Mario Dähne
1. Gutachter: Prof. Dr. Stefan Eisebitt
2. Gutachter: Prof. Dr. Manfred Albrecht

Tag der wissenschaftlichen Aussprache: 21. Oktober 2013

Berlin 2013

D83

Abstract

This thesis deals with the application of soft x-ray Fourier-transform holography (FTH) for imaging magnetic samples with nanometer structure size. FTH can be set up as a lensless method by exploiting the coherence properties of the illumination. An image of the sample is obtained by first recording a hologram which is the interference pattern of the light scattered at the sample with light originating from a reference structure. The hologram is then digitally reconstructed by a Fourier transform. The used x-ray probe facilitates nanometer spatial resolution of the images due to the small wavelength of the radiation and delivers magnetic contrast via the x-ray magnetic circular dichroism effect.

The first part of the thesis contains a theoretical investigation of the function and properties of soft x-ray FTH. The fundamental image formation process with focus on achieving magnetic contrast is deduced. Furthermore, the impact of the experimental apparatus on the image is studied in a formal way. In particular, the influence of the reference structure, the area detector, and the coherence of the radiation delivered by the x-ray source on the point spread function of the imaging system is considered. Finally, the conclusions of the findings for the actual FTH experiment are discussed.

In the second part of the thesis, an experimental application of FTH in the field of magnetic research on the nanometer scale is presented. The switching behavior of magnetic islands of a bit-patterned media (BPM) sample is studied via direct imaging of the islands' magnetic state under an applied magnetic field. The data analysis focuses on the switching field distribution of the island ensemble. The origins for the broadening of this distribution are found in an intrinsic variation, the magnetostatic interaction between the islands and thermal fluctuations. For the latter two effects, models describing the experimental findings were developed. The intrinsic variations were further investigated by structural analysis using transmission electron microscopy.

Zusammenfassung

Diese Arbeit befasst sich mit Anwendung von Fourier-Transformations-Holographie (FTH) mit weicher Röntgenstrahlung für die Abbildung magnetischer Proben mit Strukturen auf der Nanometer-Längenskala. FTH ist ein linsenloses Abbildungsverfahren, das die Kohärenzeigenschaften der Beleuchtung ausnutzt. Das Bild einer Probe wird gewonnen, indem zuerst ein Hologramm aufgenommen wird, das durch die Interferenz von Strahlung, die an der Probe gestreut wurde, und Strahlung, die von einer Referenzstruktur stammt, entsteht. Das Hologramm wird dann durch eine Fouriertransformation rekonstruiert. Die genutzte Röntgenbeleuchtung erlaubt aufgrund der kleinen Wellenlänge der Strahlung eine Auflösung im Nanometer-Bereich und liefert magnetischen Kontrast über den Röntgenzirkulardichroismus.

Der erste Teil der Arbeit enthält eine theoretische Untersuchung der Funktionsweise und der Eigenschaften von FTH mit weicher Röntgenstrahlung. Gezeigt wird der grundlegende Bildentstehungsprozess mit besonderem Fokus auf die Möglichkeit, magnetischen Kontrast zu erreichen. Weiterhin wird die Wirkung der experimentellen Apparatur auf das Bild formal abgeleitet. Insbesondere wird der Einfluss der Referenzstruktur, des Flächendetektors und der Kohärenzeigenschaften der Strahlung der Röntgenquelle auf das Abbildungssystem betrachtet. Zuletzt werden Rückschlüsse der Ergebnisse auf das eigentliche Experiment diskutiert.

Im zweiten Teil der Arbeit wird eine experimentelle Anwendung von FTH im Bereich der Magnetismusforschung auf Nanometer-Längenskala präsentiert. Das Schaltverhalten von magnetischen Inseln eines strukturierten Speichermediums wurde durch direktes Abbilden des magnetischen Zustandes der Inseln im äußeren Magnetfeld untersucht. Die Studie beschäftigt sich insbesondere mit der Verteilung der Schaltfelder im Insel-Ensemble. Die Ursachen für die Verbreiterung dieser Verteilung finden sich in intrinsischen Variationen, magnetostatischen Wechselwirkungen zwischen den Inseln und thermischen Fluktuationen. Für die letzten beiden Effekte wurden Modelle zur Beschreibung der experimentellen Befunde entwickelt. Die intrinsischen Variationen wurden zusätzlich durch Strukturuntersuchungen mittels Elektronentransmissionsmikroskopie analysiert.

Contents

List of Figures

Acronyms

BPM	bit-patterned media
CCD	charge-coupled device
CGM	continuous granular media
ECC	exchange coupled composite
FCC	face-centered cubic
FEL	free-electron laser
FIB	focused ion beam
FLASH	Free-electron Laser in Hamburg
FOV	field of view
FTH	Fourier-transform holography
FWHM	full width at half maximum
HAMR	heat-assisted magnetic recording
HERALDO	holography with extended reference by autocorrelation linear differential operation
LCLS	Linac Coherent Light Source
MAMR	microwave-assisted magnetic recording
MFM	magnetic force microscopy
MTF	modulation transfer function
OTF	optical transfer function
PSF	point-spread function
SAXS	small-angle x-ray scattering
SEM	scanning electron microscopy

SFD	switching-field distribution
Si_3N_4	silicon nitride
SNR	signal-to-noise ratio
SPD	switching probability distribution
SW	Stoner-Wohlfarth
TEM	transmission electron microscopy
UHV	ultra-high vacuum
URA	uniformly redundant array
VSM	vibrating-sample magnetometer
XMCD	x-ray magnetic circular dichroism

1 Introduction

Microscopy exerts a huge fascination on scientists as well as on the public by providing images of a world that is otherwise unaccessible to our eyes. The term *image* in this context refers to a visualization of the real-space distribution of a physical quantity describing a specimen, i.e. a data map spanned by real-space coordinates on a microscopic length scale. In the beginning of the evolution of microscopy, this quantity was always related to the specimen's transmission, reflection or dispersion properties in respect to optical light, and has been therefore closely connected to our human visual sense. Today, microscopy is extended to nearly every experimental method that records a physical quantity in a two- or even three-dimensional fashion.

The fascination of microscopic images may be facilitated by aesthetic aspects, but is particularly provoked by the special kind of how these images produce evidence. By directly coupling to our human sense of space and to our visual way of exploring space, images have the power of proving existence in the most intuitive way. Images give us the feeling of immediacy and authenticity. For example, the images of atoms on a surface first recorded by Binnig et al. using a scanning tunneling microscope[1] attracted and still attract a huge attention and finally have been awarded with the Nobel Prize, although the atomic structure of matter had been known a long time before.

As with great power comes great responsibility[2], images in a scientific context have to be handled very thoughtfully on the production side as well as on the recipient side. Images intended for a public audience may be produced under an aesthetic viewpoint in order to e.g. advertise or justify scientific research. However, images that address the scientific community have to be conceived as a representation of measured data. The viewer of an image should be aware that every image is an artifact and contains a lot of artifacts. An image is not reality. It is always mandatory to know what the image shows and what it does *not* show. For example, every image has a certain field of view which may be intentionally or arbitrarily chosen, every image exhibits a certain spatial resolution and a certain signal-to-noise ratio both hiding several object features, the space coordinates are often rescaled in combination with interpolating data, and for non-optically imaged quantities—as the majority of quantities on the nanometer scale—the colorscale is absolutely arbitrarily chosen.

Additionally, the situation is exacerbated by the digital revolution that took place in the last decades. On one hand, this revolution unprecedentedly improved the possibilities

1 See Ref. [Bin83].

2 This saying is attributed either to Voltaire or to Spider-Man.

of recording and viewing images. On the other hand, it became seductively easy to manipulate images. Image manipulation and image analysis became essential tools in the microscopy field, but the process has to be reproducible and well documented. At each step of the production process, the question of how much information is artificially added or removed has to be considered with a distinct sense of responsibility. Due to the digital reliefs in image processing, both the amount and the impact of images in the process of scientific reasoning have vastly increased in the recent past. As a result, the scientific image also came into the focus of the philosophy of science and the research of visual culture[1].

The first part of this thesis (Chap. 2) is a thorough investigation of the function of the imaging method called soft x-ray Fourier-transform holography (FTH). This imaging method employs x-rays as probe. In general, microscopy using x-rays instead of optical light is motivated by the fact that a probe with a smaller wavelength also allows for a smaller spatial resolution length of the images. Nevertheless, the x-ray image contrast is commonly created by absorption and dispersion of the sample analogously to the optical regime. Due to resonances of the photon energy with transitions of core electrons in the specimen, these optical properties may also provide an element selectivity. In addition, the x-rays are even sensitive to the magnetization of the element at certain resonances. In the last years, FTH imaging has been particularly successful in exploiting this magnetic contrast. Today, the method is routinely applied in the research of magnetic structures on a nanometer lengthscale.

Despite the routine application of soft x-ray FTH, the characterization of its imaging properties remains fragmentary in literature. The aim of the investigation in Chap. 2 is to provide the mathematical background of the imaging process. The background is absolutely mandatory to gain a better understanding and a more qualified physical meaning to the images produced by this method. For the scientist producing the image this knowledge will help to improve the analysis of the image data, for the scientist viewing the image this knowledge will help to interpret and evaluate the images in a more critical way.

After a more detailed introduction to FTH at the beginning of Chap. 2, the basic concept of the method and the principles of the image formation are reviewed. The focus of the chapter lies on the derivation of how magnetic contrast is obtained with FTH and of how the imaging apparatus fundamentally affects the image properties. The latter point is performed by calculating the point spread function of the imaging system. The chapter closes with a summary that explicitly refers to the practical implications of the previous findings.

The second part of this thesis (Chap. 3) presents an application of FTH imaging in the field of nano-magnetism. In this experiment, the switching of magnetic islands in a bit-patterned media (BPM) sample is observed via direct imaging. The islands have

1 An introduction to the field can be found in Ref. [Ade09].

a size of only 80 nm. The BPM technology is a leading candidate for the development of novel magnetic data storage devices. The presented study particularly focuses on the variation in the strength of an externally applied magnetic field needed to switch different islands from one magnetization state to the opposite one. This variation is called the switching-field distribution (SFD) and the goal of the study is to find the specific origins of that distribution. In general, the SFD is caused by the intrinsic properties of each island, by the magnetostatic interaction between the islands and by thermal fluctuations. Methodically, the study shall serve as an experimental example of how FTH images with magnetic contrast are produced and analyzed. The analysis contains a variety of methods and tools which help to gain more qualified information about the islands and their interaction from the direct images of the islands' magnetization state. In the last step, singular islands selected with the help of the FTH images were investigated using transmission electron microscopy in order to analyze the structure of these islands.

The last chapter (Chap. 4) intends to give an outlook for the future application of FTH in the field of nano-magnetism. The particular strengths and advantages of the imaging method are reviewed by presenting additional experimental applications of FTH the author of this thesis was involved in. From these examples, future application scenarios are anticipated.

2 Fourier-transform holography

The holography imaging method was invented by Dennis Gábor in 1948 [Gá48] and substantially developed further in the following years [Gá49; Gá51]. Initially, Gábor was searching for an alternative electron microscopy method circumventing the limits in spatial resolution set by the aberrations of the magnetic lenses. However, the method made its breakthrough in the optical regime with the advent of lasers as coherent light sources. In the optical regime, holography is particularly famous for being able to produce 3D images.

Holography is a two-step imaging process [Gá49]. In the first step, the *hologram* is recorded which is the superposition of the radiation diffracted by the object and a reference wave. Due to the interference of the object wave with the known, undisturbed reference wave, the information about the phase variations in the object wave are encoded as intensity variations in the hologram. If solely the object wave had been recorded, this phase information would have been lost in the detection process. In principle, every probe obeying a wave character (e.g. photons or electrons) can be used for recording a hologram under the restriction that the illumination is at least partially coherent.

The second imaging step is taken by the *reconstruction* of the hologram yielding the image of the object. The reconstruction is performed either optically or numerically. For an optical reconstruction, the hologram has to be recorded on a photographic plate. The hologram is then illuminated by the reference wave only, producing the image of the object. In addition, a second image, the so-called *twin image* is created which is an exact, but complex conjugated copy of the first one. The twin image arises due to the fact that the encoding of the phases in the intensities of the diffraction pattern is only determined up to a modulo of π. In other words, both the real image and the twin image have the same diffraction pattern.

Today, the numerical reconstruction is much more common as each optical system can be numerically simulated. The hologram has to be recorded digitally, e.g. by using a charge-coupled device (CCD) detector. For this reason, the method is also know as digital holography. This procedure has the advantages that (i) the reconstruction is free from aberrations of the optical reconstruction system, (ii) a reconstruction can already be generated at the same time the hologram is taken, and (iii) the data can be readily manipulated for different contrast mechanisms [Gue09] and further analyzed.

Gábors original idea of using holography as a microscopy alternative was revived in the field of x-ray microscopy where the availability of high-resolution and high-efficiency focusing optics is also very limited. The attempt of adapting holography to x-ray wavelength was particularly brought forward by Stroke and coworkers [Str65a; Str64; Str65b] and by Winthrop and Worthington [Win65; Win66]. This development finally led to the invention

of the completely *lensless* Fourier-transform holography (FTH) method. Here the reference wave is created by a point source in the sample plane and the reconstruction is yielded by a Fourier transform of the hologram giving the name to the method. The first serious experimental realization of the concept in the soft x-ray regime was demonstrated in 1992 by McNulty et al. [McN92] using radiation produced by a synchrotron. In this experiment, the point source is created by the focus of a Fresnel zone plate, resulting in a resolution of 60 nm clearly surpassing the capabilities of optical microscopy. Twelve years later, Eisebitt and coworkers presented the first completely lensless x-ray approach by applying a nano-fabricated optics mask with a tiny pinhole of only some tens of nanometer diameter as source for the reference wave. In the following years, the method became very popular, in particular in the field of nano-magnetism [Gü08; Gü10; Hau08; Pfa11; SN09] because of its easy implementation, high reliability and high flexibility.

In this chapter, the soft x-ray FTH method in its variant following the ideas of Eisebitt et al. is thoroughly reviewed. The first sections describe the basic concept and the general image formation process of the method. The latter is then applied to the case of imaging with magnetic contrast. It is explicitly treated how the magnetic information is encoded in the reconstruction and in which way it is properly extracted—an analysis that is missing in literature up to now. Another emphasis is laid on the problem of achievable image quality, in particular achievable spatial resolution. Although most of the problems have already been discussed in literature for optical holography, a new analysis and compilation of the effects with strong focus on soft x-ray FTH seems to valuable for the following reasons: (i) The FTH geometry only plays a minor role in the optical regime, (ii) the x-ray concept abandons any lenses, (iii) the x-ray hologram is always taken and reconstructed digitally, (iv) the setup geometry is very different due to the differences in the optical constants and the occurring scattering angles, and (v) the properties of the light sources are different, especially with respect to the coherence properties. In the last section of this chapter, these findings are summarized and applied to the experimental conditions of the study presented in the subsequent chapter of the thesis.

2.1 Basic soft x-ray concept

In the optical regime, a number of very different geometries for realizing a holography experiment exist. The main differences can be found in the way the light scattered from the object is detected (reflection or transmission geometry), in the shape of the reference wave (e.g. plane wave or spherical wave) and in the way the scattered object wave and the reference wave are optically brought to interference [Goo05]. For soft x-rays, however, the degree of freedom in the choice of possible holographic geometries drastically reduces due to, in particular, two properties of the radiation in the wavelength regime between 20 nm and 0.5 nm. First, the optical constants of matter equaling nearly unity in this regime result in generally low reflectivities and the small x-ray wavelength causes short absorption lengths on the order of micrometers [Att00]. The availability of x-ray optics is

therefore mainly limited to (shaped) grazing incidence mirrors and diffractive elements. The specimen are most conveniently inspected in transmission and have to be very thin. Second, the non-perfect coherence properties of all x-ray sources in combination with the very small wavelengths allow only for small pathlength differences in the interfering beams which restricts the experiment to an in-line geometry and to small scattering angles.

Consequentially, an x-ray holography experiment is, in principle, set up very similarly to a small-angle x-ray scattering (SAXS) experiment in transmission geometry, but with at least one additional optical element creating spatially coherent illumination and a reference wave. Figure 2.1 sketches the (coherent) SAXS geometry and introduces the basic quantities and the coordinate system as used throughout this thesis. The incoming x-rays travel along the z-direction and are elastically scattered in the sample. Under elastic scattering, the wavelength λ of the radiation stays unaltered and the magnitude of the incoming ($\boldsymbol{k}_i$) and outgoing ($\boldsymbol{k}_f$) wave vector is equal, i.e. $|\boldsymbol{k}_i| = |\boldsymbol{k}_f| = k = 2\pi/\lambda$. In general x-ray diffraction theory, the scattered radiation in the far-field is connected to the structure of the sample (more precisely to the electron density) via a Fourier transform [Ash76]. In Fourier space, the elastic scattering condition can be illustrated via the Ewald sphere that has the radius k [Ash76]. The Ewald sphere's surface section of the object's Fourier-space representation directly determines the observed scattering intensity under a certain scattering angle 2θ. The magnitude of the light's momentum transfer $\boldsymbol{q} = \boldsymbol{k}_f - \boldsymbol{k}_i$ in the scattering process is then calculated from the scattering angle as:

$$q = \frac{4\pi}{\lambda} \sin\theta \,. \tag{2.1}$$

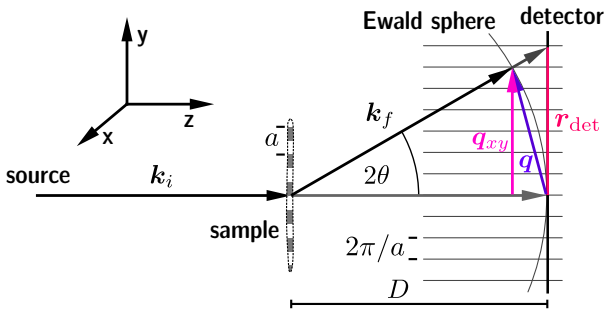

Figure 2.1: The SAXS geometry. The incoming light is elastically scattered under the scattering angle 2θ experiencing a momentum transfer of $\boldsymbol{q}$. The elastic scattering condition $|\boldsymbol{k}_i| = |\boldsymbol{k}_f|$ is represented by the Ewald sphere in Fourier space. For a quasi-2D sample, a real-space structure with an *in-plane* periodicity a, e.g. magnetic domains in a thin-film, will translate into $2\pi/a$-spaced reflexes in Fourier space that are elongated along the direction of the surface normal.[1] Due to the elongation, the Ewald sphere intersects with every reflex (as long as $k \geq 2\pi n/a$ with n being the diffraction order) where $q_{xy} = 2\pi n/a$ contains the information about the in-plane frequencies.

The samples that are considered in this thesis, in particular magnetic thin-film samples, have a very small thickness (on the order of tens of nanometers) compared to their lateral extent (a few micrometers). The sample is, thus, treated as a quasi two-dimensional (2D) object with the image obtained in the holography experiment being a projection of the sample along the beam direction (z-direction). The Fourier transform of an object that is very thin along the z-direction shows constant values along that direction. The lateral sample structure information is thus obtained from the intensity variations in dependence on the momentum transfer component parallel to the sample plane. The magnitude of this component is given by:

$$q_{xy} = \frac{2\pi}{\lambda} \sin 2\theta \,. \tag{2.2}$$

However, if a flat area detector in a distance D from the sample is used, the detector will not follow the Ewald sphere's surface. The radial position on the detector r_{det} is depending on the scattering angle as:

$$r_{\mathrm{det}} = D \tan 2\theta \,. \tag{2.3}$$

When comparing Eqs. 2.1, 2.2 and 2.3 one realizes that only in the case of small scattering angles, q and q_{xy} can be treated as equal and the position on the detector linearly scales with the momentum transfer. In the general case, the data from the 2D detector has to be non-linearly rescaled to the q_{xy}-scale [Sch13]. The experimental data in this work is exclusively recorded in the small-angle scattering regime and a correction is not applied.

The easiest way to transform a SAXS setup into a holography setup is to introduce a small aperture in a certain distance in front of the sample. The aperture creates a spherical coherent wave illuminating the sample. The radiation is partially scattered in the sample and partially transmitted through the sample. Both waves, the scattered and transmitted one, interfere and form the hologram on a detector behind the sample. This method is referred to as x-ray in-line holography [Bar10; Ros08]. Although being very simple to set up, the method has three major drawbacks. First, the photon efficiency is very low due to the small pinhole. This problem can be circumvented by using a beam focusing zone plate [Hei11]. Second, the method is very sensitive to instabilities in the setup, in particular the position of the optics pinhole with respect to the sample. Third, the reconstructed image overlaps with its unfocused twin image resulting in a distortion of the image.

A very elegant way to solve these problems was first realized by Eisebitt et al. [Eis04] in a soft x-ray compatible FTH setup. In the FTH geometry, the scattered light from the object is superimposed with a spherical reference wave that has its origin in the object plane with a certain lateral offset from the sample (Fig. 2.2). In the optical regime, the spherical wave can easily be created by a focusing lens, a concept which was also adapted

1 The elongated reflexes are also known as crystal truncation rods occurring in surface sensitive diffraction methods such as grazing incidence SAXS [Sta04].

for x-rays [McN92]. But the breakthrough of the method was reached by a completely lensless approach of using a small pinhole as reference wave source [Eis04].

In this approach, the FTH geometry is realized by integrating the specimen, the object aperture defining the field of view (FOV) as well as ensuring coherent illumination and the pinhole creating the reference wave into a single element. This element is commonly fabricated by covering one side of an x-ray transparent substrate membrane with a metal film that is opaque to soft x-rays. The metal film is nano-structured with the object and the reference apertures. On the opposite side of the membrane, the object is placed.[1] Due to the integrated, fixed sample design, the method is very insensitive to drift or vibration in the setup. Any drift or vibration present will not compromise the resolution, but only affect the contrast of the reconstruction. In addition, the absence of any further optical elements enables a certain amount of empty space around the sample and, therefore, allows for a high flexibility in the sample environment.

The particular charm of the FTH method lies in the way the image is reconstructed from the hologram: an unambiguous reconstruction is obtained by a single Fourier transform of the hologram which makes the reconstruction very robust against noise. Due to the offset between the sample and the reference wave origins, the twin images in the reconstruction are spatially separated from each other. A detailed description of the image formation and reconstruction process will be given in the following sections.

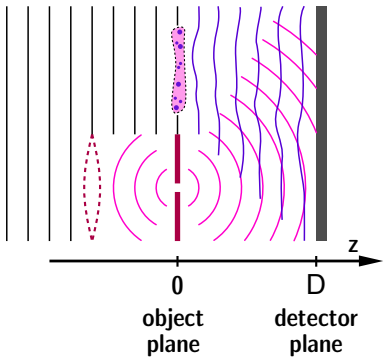

Figure 2.2: Schematic FTH geometry. The origin of the spherical reference wave lies in the object plane. The reference wave is either created by a focusing lens or a small pinhole.

1 A detailed description of such a fabrication process is given in Sec. 3.2.1.

2.2 Image formation

X-ray imaging as it is perceived in this thesis is based on elastic scattering of photons at the electrons in the sample. This light–matter interaction is in principle described by the differential scattering cross-section $\mathrm{d}\sigma(\omega)/\mathrm{d}\Omega$ giving the probability of finding a scattered photon with frequency ω within the solid angle $\mathrm{d}\Omega$ under a scattering angle 2θ. In particular, the scattering cross-section contains the Thomson scattering cross-section of a single electron, the atomic scattering factor describing the atoms' electron shell and the structure factor with information about the arrangement of the atoms, e.g. the lattice structure. However, for soft x-ray radiation as solely considered in this thesis, the wavelength of the radiation is much longer than the intra-atomic distances and even longer than the nearest neighbor inter-atomic distances. It is therefore more convenient to use a continuous description of the medium the light is passing through, i.e. to employ the medium's refractive index $n(\omega)$. In the soft x-ray regime, the refractive index is smaller than one, but deviates from unity only by a small amount and is therefore commonly written as [Att00]:

$$n(\omega) = 1 - \delta + \mathrm{i}\beta\,. \tag{2.4}$$

The elastic light–matter interaction is based on the driven oscillation of bound electrons in the radiation's electric field and is thus characterized by resonances and damping of the oscillation. The refractive index reflects the interaction by containing a dispersive part δ and an absorptive part β. The dispersion relation in a medium with refractive index n reads:

$$\frac{\omega}{k} = \frac{c}{n} = \frac{c}{1-\delta+i\beta}\,, \tag{2.5}$$

where c defines the vacuum speed of light. A plane wave $\boldsymbol{E} = \boldsymbol{E_0}\exp(\mathrm{i}(\boldsymbol{kr} - \omega t))$ passing along the z-direction ($\boldsymbol{kr} = kz$) through the medium, i.e. a specimen, is influenced as [Att00]:

$$\begin{aligned}
\boldsymbol{E} &= \boldsymbol{E_0}\exp[\mathrm{i}(kz-\omega t)] && (2.6)\\
&= \boldsymbol{E_0}\exp\left[\mathrm{i}\left(\frac{\omega n z}{c} - \omega t\right)\right] = \boldsymbol{E_0}\exp\left[\mathrm{i}\frac{\omega}{c}(1-\delta+\mathrm{i}\beta)z - \mathrm{i}\omega t\right] && (2.7)\\
&= \boldsymbol{E_0}\exp\left[\mathrm{i}\omega\left(\frac{z}{c} - t\right)\right]\exp\left[-\mathrm{i}\frac{2\pi\delta}{\lambda}z\right]\exp\left[-\frac{2\pi\beta}{\lambda}z\right]\,. && (2.8)
\end{aligned}$$

The first term in Eq. 2.8 describes the vacuum propagation, the second term gives a phase shift due to the medium and the last term is responsible for the decay of the amplitude, i.e. the absorption of the radiation in the medium.

In FTH and all other x-ray imaging techniques that operate in transmission mode, the finite specimen in vacuum is confined along the light's propagation direction (z) to a

thickness d. Consequentially n is equal to unity except for $0 < z < d$ and the last two terms of Eq. 2.8 are combined in the (complex) transmission function $t(x, y)$ of a sample:

$$t(x,y) = \exp\left[\frac{2\pi}{\lambda}\int_0^d \left(-\mathrm{i}\delta(x,y,z) - \beta(x,y,z)\right)\,\mathrm{d}z\right]\,. \tag{2.9}$$

The sample is illuminated by a probe wave $\psi_0(x, y)$ (also called illumination function) which after propagation through the sample has changed into the exit wave $\psi(x, y)$. In the easiest (linear) case, one would assume that the exit wave is given by:

$$\psi(x,y) = t(x,y)\,\psi_0(x,y)\,. \tag{2.10}$$

The validity of this wave factorization assumption has been analyzed in the supporting online material of Ref. [Thi08]. The authors end up with the following condition for the validity:

$$\frac{R}{d} \gg \frac{\lambda}{l}\,, \tag{2.11}$$

where R is the spatial resolution of the experiment and l the extend of the illumination function which in the special case of FTH imaging is most often confined by an object aperture. There are two practical cases that can be derived from this condition. First, for a sample with similar longitudinal as transversal size, the experimentally feasible resolution length will be much longer than the wavelength. And second, if high resolution is desired one has to use a very thin sample compared to its transversal extend. As already pointed out, this thesis solely treats the latter case.

Assuming the validity of the wave factorization relation (Eq. 2.10) and assuming plane-wave illumination, the exit wave behind the sample is given by the transmission function. In turn this means, by reconstructing the exit wave, one obtains the transmission function of the sample, which is then called the *image* of the sample.

Continuing with the assumption of thin samples, Eq. 2.9 simplifies to

$$t(x,y) \simeq 1 - \mu(x,y) - \mathrm{i}\phi(x,y)\,, \tag{2.12}$$

since the absorption and dispersion parts are small in the x-ray range, i.e. $\beta, \delta \approx 10^{-3}$, and λ and d have similar values in the nanometer range. The quantities $\mu(x, y)$ and $\phi(x, y)$ are the z-integrated properties of the sample:

$$\mu(x,y) = \frac{2\pi}{\lambda}\int_0^d \beta(x,y,z)\,\mathrm{d}z\,, \quad \phi(x,y) = \frac{2\pi}{\lambda}\int_0^d \delta(x,y,z)\,\mathrm{d}z\,. \tag{2.13}$$

The image obtained in a transmission x-ray geometry is always a *projection* image of

the sample.

In a typical FTH experiment, the exit wave freely propagates from the back sample plane to the area detector which is placed in the far-field region. The far-field region is reached when the Fresnel number F is much smaller than unity:

$$F = \frac{l^2}{D\lambda} \ll 1\,, \tag{2.14}$$

with l being again the object or illumination extend and D the sample–detector distance. In other words, for a given wavelength λ one has to observe a small object from a large distance. The scattered wave field in the far-field region is described by the Fraunhofer diffraction integral which is the 2D spatial Fourier transform of the exit wave:

$$\Psi(q_x, q_y) = \iint_{-\infty}^{\infty} \psi(x, y) \exp[-\mathrm{i}(q_x x + q_y y)]\,\mathrm{d}x\mathrm{d}y \tag{2.15}$$

In the following, the 2D Fourier integral will be abbreviated with $\mathcal{F}\{\}$ and the inverse transform with $\mathcal{F}^{-1}\{\}$. Commonly, the forward Fourier transformation points from the direct space to reciprocal space, while the inverse transformation points into the opposite direction. A point in the sample plane is defined by $\boldsymbol{r} = (x, y)$ and for the detector plane the reciprocal space coordinates $\boldsymbol{q} = (q_x, q_y)$ are used:

$$\Psi(\boldsymbol{q}) = \mathcal{F}\{\psi(\boldsymbol{r})\}\,, \quad \psi(\boldsymbol{r}) = \mathcal{F}^{-1}\{\Psi(\boldsymbol{q})\}\,. \tag{2.16}$$

The detector records an intensity signal, i.e. the magnitude squared of the wave's amplitude with the consequence that the phase information is lost. Assuming fully coherent illumination of the sample, the scattering pattern, which in case of a holography experiment is referred to as a *hologram*, is expressed as:

$$P(\boldsymbol{q}) = |\Psi(\boldsymbol{q})|^2 = \mathcal{F}^*\{\psi(\boldsymbol{r})\}\mathcal{F}\{\psi(\boldsymbol{r})\}\,. \tag{2.17}$$

The complex conjugate Fourier transform is denoted by $\mathcal{F}^*$. Due to the loss of phase information, the exit wave cannot be easily retrieved from the scattering pattern. A Fourier transform of the scattering pattern only yields the spatial auto-correlation of the exit wave which is also called the *Patterson map*:

$$p(\boldsymbol{r}') = \mathcal{F}^{-1}\{\mathcal{F}^*\{\psi(\boldsymbol{r})\}\mathcal{F}\{\psi(\boldsymbol{r})\}\} \tag{2.18}$$

$$= \psi^*(-\boldsymbol{r}) * \psi(\boldsymbol{r}) \tag{2.19}$$

$$= \iint_{-\infty}^{\infty} \psi^*(-\boldsymbol{r})\psi(\boldsymbol{r} + \boldsymbol{r}')\,\mathrm{d}\boldsymbol{r}\,. \tag{2.20}$$

The auto-correlation is formed by convolution (indicated with the $*$ symbol) of the exit

wave ψ with its complex conjugate ψ^*.

The coordinate system of p is generated by the relative vectors $\boldsymbol{r}'$. In holography the so-called *phase problem* is solved by coherently superimposing a reference wave to the exit wave. In the soft x-ray FTH geometry, the reference wave originates from a small source point in the object plane. The exit wave is then composed of a reference wave $\rho(\boldsymbol{r})$ and a spatially separated object wave $o(\boldsymbol{r}-\boldsymbol{r}_0)$:

$$\psi(\boldsymbol{r}) = b\rho(\boldsymbol{r}) + o(\boldsymbol{r}-\boldsymbol{r}_0)\,. \tag{2.21}$$

The complex factor b accounts for deviations from the plane wave illumination. It is dependent on the separation vector $\boldsymbol{r}_0$ and, in particular, contains the phase difference in the illumination function between the object and reference location, i.e. $b(\boldsymbol{r}_0) = |b(\boldsymbol{r}_0)|\exp(\mathrm{i}\beta(\boldsymbol{r}_0))$. As these phase variation are assumed to happen on a length scale much longer than the object and reference extends, b is treated as a constant in the following. The Patterson map of the combined sample becomes:

$$\begin{aligned} p(\boldsymbol{r}') &= [b^*\rho^*(-\boldsymbol{r}) + o^*(-\boldsymbol{r}-\boldsymbol{r}_0)] * [b\rho(\boldsymbol{r}) + o(\boldsymbol{r}-\boldsymbol{r}_0)] && (2.22)\\ &= b^*b\rho^*(-\boldsymbol{r}) * \rho(\boldsymbol{r}) + o^*(-\boldsymbol{r}) * o(\boldsymbol{r}) \\ &\quad + b^*\rho^*(-\boldsymbol{r}) * o(\boldsymbol{r}-\boldsymbol{r}_0) + bo^*(-\boldsymbol{r}-\boldsymbol{r}_0) * \rho(\boldsymbol{r})\,. && (2.23)\end{aligned}$$

The first two terms of Eq. 2.23 again describe the auto-correlation of both waves.[1] The cross-correlations between object and reference are relevant for the image formation. If $\rho(\boldsymbol{r})$ is a delta-like reference object, i.e. $b\rho(\boldsymbol{r}) = b\delta(\boldsymbol{r})$, the terms reduce to $b^*o(\boldsymbol{r}'-\boldsymbol{r}_0)$ and $bo^*(-\boldsymbol{r}'-\boldsymbol{r}_0)$, respectively. In other words, the object exit wave field, i.e. both the real and the imaginary part, is reconstructed at position $\boldsymbol{r}_0$ and its complex conjugate and point-mirrored copy, the twin image, at position $-\boldsymbol{r}_0$ in the Patterson matrix (Fig. 2.3). If a (forward) Fourier transform instead of an inverse transform is used for the reconstruction of the hologram, the image and its twin image flip their positions. Identifying $o(\boldsymbol{r})$ with the sample's transmission function (Eq. 2.9), one obtains for the image reconstruction p_i and the twin image p_i^*:[2]

$$p_i(x,y) = b^*(1-\mu(x,y) - i\phi(x,y)) \tag{2.24}$$

$$p_i^*(x,y) = b(1-\mu(x,y) + i\phi(x,y)) \tag{2.25}$$

The phase of the factor b is given by the phase difference in the illumination of the object and reference. In case of a perfect plane-wave illumination this difference vanishes and b reduces to the reference amplitude.

For a successful reconstruction, two implications for the experiment can already be derived from Eq. 2.23: (i) The separation vector $\boldsymbol{r}_0$ has to be large enough to ensure

1 In the auto-correlation the object offset can be omitted.

2 The formal coordinate change and the $\boldsymbol{r}_0$ offset are omitted.

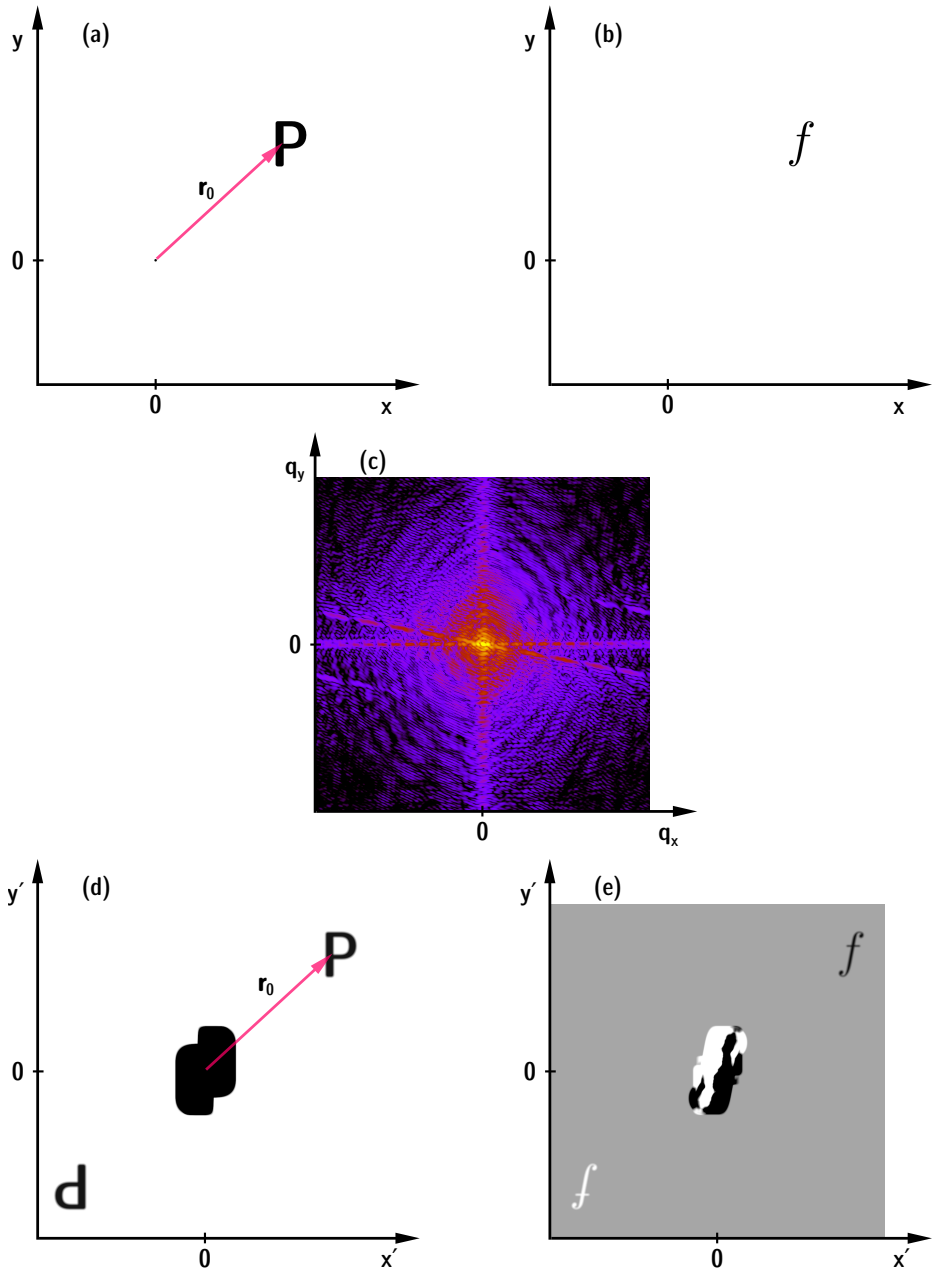

Figure 2.3: Simulation of the FTH imaging process. **(a)** Real part of the exit wave with the reference structure in the space origin and the object which is offset by $\boldsymbol{r}_0$. **(b)** Imaginary part of the object. **(c)** Calculated hologram, i.e. far-field diffraction pattern, of (a) and (b). Only the magnitude squared of the light field is recorded. **(d)** Real part and **(e)** imaginary part of the reconstruction of the hologram. The whole exit wave is reconstructed at the position $\boldsymbol{r}_0$. The complex conjugate twin image is formed at $-\boldsymbol{r}_0$.

that the auto-correlations and the reconstructions do not overlap in the Patterson matrix. Since the extent of the auto-correlation is twice as large as the object itself, this criterion is fulfilled if the magnitude of $\boldsymbol{r}_0$ is larger than 1.5 times the sample diameter. (ii) The resolution of the image is limited by the radius of the reference hole, because the reconstruction is obtained by the convolution of the object with the reference. The latter point is discussed in more detail in Sec. 2.4.

2.3 Object and reference multiplexing

In general imaging theory, an imaging system is represented by a mathematical operator $\mathcal{S}\{\}$ that operates on an input function and returns the output function, the image [Goo05]. Using the nomenclature from the previous section, the object exit wave $o(x, y)$ represents the input and $p_i(x', y')$ represents the output:

$$p_i(x', y') = \mathcal{S}\{o(x, y)\}\,. \tag{2.26}$$

An important class of systems are *linear* systems. A system is said to be linear, if the superposition principle holds for all input functions ψ and χ, and for all complex constants a and b:

$$\mathcal{S}\{a\psi(x, y) + b\chi(x, y)\} = a\mathcal{S}\{\psi(x, y)\} + b\mathcal{S}\{\chi(x, y)\}\,. \tag{2.27}$$

In the following, it will be shown that FTH imaging obeys this principle and can be treated as being linear. This finding is not purely academic, as it directly implies the experimental possibility of simultaneously using multiple objects and reference structures in the illuminated area, a method which is therefore called object and reference multiplexing [Pfa10a; Sch07b; Sch06; Sch07c].

The coherently illuminated sample is assumed to consist of two objects $o_1(\boldsymbol{r} - \boldsymbol{r}_{o1})$ and $o_2(\boldsymbol{r} - \boldsymbol{r}_{o2})$, and two references $\rho_1(\boldsymbol{r} - \boldsymbol{r}_{\rho1})$ and $\rho_2(\boldsymbol{r} - \boldsymbol{r}_{\rho2})$ located at the positions $\boldsymbol{r}_{o1}$, $\boldsymbol{r}_{o2}$, $\boldsymbol{r}_{\rho1}$, and $\boldsymbol{r}_{\rho2}$ in the same plane. By analogy with Eq. 2.21, the full sample is mathematically formed by the sum of these four structures with the complex constants a_1, a_2, b_1, and b_2 again reflecting amplitude and phase variation in the illumination.

$$\psi(\boldsymbol{r}) = a_1 o_1(\boldsymbol{r} - \boldsymbol{r}_{o1}) + a_2 o_2(\boldsymbol{r} - \boldsymbol{r}_{o2}) + b_1 \rho_1(\boldsymbol{r} - \boldsymbol{r}_{\rho1}) + b_2 \rho_2(\boldsymbol{r} - \boldsymbol{r}_{\rho2}) \tag{2.28}$$

The Patterson map (Eq. 2.18) will then contain all auto-correlations (p_a), the cross-correlations between different objects (p_c) and the desired cross-correlations between objects and references forming the images (p_i) and twin images (p_i^*):

$$\begin{aligned} p = {} & [a_1^* o_1^*(-\boldsymbol{r} - \boldsymbol{r}_{o1}) + a_2^* o_2^*(-\boldsymbol{r} - \boldsymbol{r}_{o2}) + b_1^* \rho_1^*(-\boldsymbol{r} - \boldsymbol{r}_{\rho1}) + b_2^* \rho_2^*(-\boldsymbol{r} - \boldsymbol{r}_{\rho2})] \\ & * [a_1 o_1(\boldsymbol{r} - \boldsymbol{r}_{o1}) + a_2 o_2(\boldsymbol{r} - \boldsymbol{r}_{o2}) + b_1 \rho_1(\boldsymbol{r} - \boldsymbol{r}_{\rho1}) + b_2 \rho_2(\boldsymbol{r} - \boldsymbol{r}_{\rho2})] \qquad (2.29) \\ = {} & p_a + p_c + p_i + p_i^* \qquad (2.30) \end{aligned}$$

$$p_a = a_1^* a_1 o_1^*(-\boldsymbol{r}) * o_1(\boldsymbol{r}) + a_2^* a_2 o_2^*(-\boldsymbol{r}) * o_2(\boldsymbol{r}) + b_1^* b_1 \rho_1^*(-\boldsymbol{r}) * \rho_1(\boldsymbol{r}) + b_2^* b_2 \rho_2^*(-\boldsymbol{r}) * \rho_2(\boldsymbol{r}) \tag{2.31}$$

$$p_c = a_1^* a_2 o_1^*(-\boldsymbol{r}) * o_2(\boldsymbol{r} - \boldsymbol{r}_{o2} + \boldsymbol{r}_{o1}) + a_2^* a_1 o_2^*(-\boldsymbol{r}) * o_1(\boldsymbol{r} - \boldsymbol{r}_{o1} + \boldsymbol{r}_{o2}) + b_1^* b_2 \rho_1^*(-\boldsymbol{r}) * \rho_2(\boldsymbol{r} - \boldsymbol{r}_{\rho 2} + \boldsymbol{r}_{\rho 1}) + b_2^* b_1 \rho_2^*(-\boldsymbol{r}) * \rho_1(\boldsymbol{r} - \boldsymbol{r}_{\rho 1} + \boldsymbol{r}_{\rho 2}) \tag{2.32}$$

$$p_i = b_1^* a_1 \rho_1^*(-\boldsymbol{r}) * o_1(\boldsymbol{r} - \boldsymbol{r}_{o1} + \boldsymbol{r}_{\rho 1}) + b_1^* a_2 \rho_1^*(-\boldsymbol{r}) * o_2(\boldsymbol{r} - \boldsymbol{r}_{o2} + \boldsymbol{r}_{\rho 1}) + b_2^* a_1 \rho_2^*(-\boldsymbol{r}) * o_1(\boldsymbol{r} - \boldsymbol{r}_{o1} + \boldsymbol{r}_{\rho 2}) + b_2^* a_2 \rho_2^*(-\boldsymbol{r}) * o_2(\boldsymbol{r} - \boldsymbol{r}_{o2} + \boldsymbol{r}_{\rho 2}) \tag{2.33}$$

$$p_i^* = a_1^* b_1 o_1^*(-\boldsymbol{r} - \boldsymbol{r}_{o1} + \boldsymbol{r}_{\rho 1}) * \rho_1(\boldsymbol{r}) + a_2^* b_1 o_2^*(-\boldsymbol{r} - \boldsymbol{r}_{o2} + \boldsymbol{r}_{\rho 1}) * \rho_1(\boldsymbol{r}) + a_1^* b_2 o_1^*(-\boldsymbol{r} - \boldsymbol{r}_{o1} + \boldsymbol{r}_{\rho 2}) * \rho_2(\boldsymbol{r}) + a_2^* b_2 o_2^*(-\boldsymbol{r} - \boldsymbol{r}_{o2} + \boldsymbol{r}_{\rho 2}) * \rho_2(\boldsymbol{r}) \tag{2.34}$$

For each sample, independent reconstructions using both references and their associated twin images are obtained, yielding eight images altogether (Fig. 2.4). This calculation can be easily extended to more objects and/or references as it is shown for many references in Refs. [Gü12; Gü11]. The separation vectors $\boldsymbol{r}_{o1}$,$\boldsymbol{r}_{o2}$, $\boldsymbol{r}_{\rho 1}$, and $\boldsymbol{r}_{\rho 2}$ have to be carefully chosen, in order to avoid an overlap of an image with cross-correlations or other images. Since all objects and references usually have a small extent compared to the distances between them, the positions of the cross-correlations and images in the reconstruction can be readily obtained from the equations above, e.g. object $o_1(\boldsymbol{r})$ is reconstructed at $\boldsymbol{r}_{o1} - \boldsymbol{r}_{\rho 1}$ and $\boldsymbol{r}_{o1} - \boldsymbol{r}_{\rho 2}$. If the distance between the samples is increased and becomes

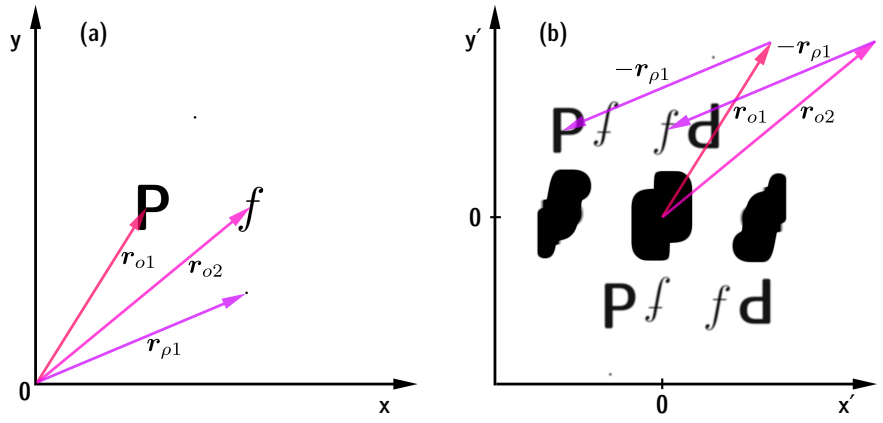

Figure 2.4: Object and reference multiplexing in an FTH experiment. **(a)** Real-space sample consisting of two objects and two references. **(b)** Reconstruction resulting in two images of each object and associated twin images. In both cases only the real part is shown. Two examples for the position of the images in the reconstruction matrix are selected. If $\boldsymbol{r}_{o1}$ and $\boldsymbol{r}_{o2}$ denote the position of the first and the second object and $\boldsymbol{r}_{\rho 1}$ denotes the position of the first references, the images are reconstructed at positions corresponding to the differences of these vectors, i.e. $\boldsymbol{r}_{o1} - \boldsymbol{r}_{\rho 1}$ and $\boldsymbol{r}_{o2} - \boldsymbol{r}_{\rho 1}$.

much longer than the x-ray coherence length, the diffraction patterns of the samples will add up incoherently on the detector and the cross-correlation terms will vanish in the reconstruction [Sch07c]. Of course, a reference pinhole should be associated to each sample within the coherence length in order to achieve an image reconstruction with high contrast.

Coming back to the question of the linearity of the imaging process, the above calculations show that FTH fulfills the principle in Eq. 2.27. Although the complete reconstruction matrix also contains cross-talk terms of the two objects and also quadratic terms, the actual images p_i are formed by a convolution with the reference structure, which is a linear operation. Furthermore, in the coherent case, when both objects and the references are located within the coherence area of the illumination[1] as well as in the incoherent case, where the two object–reference pairs are independent from each other, the imaging process is linear and each object is independently imaged from the other object. In the latter case, one has to be aware of the fact, that due to the incoherent superposition of the holograms on the detector, the contrast of every individual reconstruction reduces and a longer acquisition time is needed to achieve the same signal-to-noise ratio (SNR) as in a separate measurement of both objects.

The advantage of the object multiplexing method clearly lies in the possibility of simultaneously imaging different areas on the sample under exactly the same external conditions. This advantage was already exploited in a few studies of nano-magnetic systems [Gü10; Pfa11] and is also demonstrated in the experiments presented in the second part of this thesis.

On the other hand, reference multiplexing is a standard procedure in recent x-ray FTH imaging and is employed in many studies, e.g. Refs. [Cam11; Gü08; Gü10; Sta08; Sti11; SN09]. The most important reason for reference multiplexing is the benefit in image quality. There are two different strategies: either the images independently created by each reference are summed up in order to increase the SNR of the reconstruction [Sch06] or the image showing the best quality is selected [Sch07b]. The quality of the reconstruction is strongly connected to the fabrication quality of the reference structure which is varying due to the complexity of producing nanometer-sized apertures.

Another application of the multiplexing capabilities of FTH was proposed in the field of ultra-fast time-resolved imaging [Gü12; Gü11; Pfa10a; Sch07c]. These methods rely on the facts that spatial separation can be translated to time differences and that FTH is able to produce spatially separated images although the holograms taken at different time steps overlap on the detector.

2.4 The point-spread function

Another striking consequence of the linearity of the FTH process as shown in Sec. 2.3 is the possibility of describing the function of the imaging system by the *point-spread*

1 A thorough explanation of coherence with respect to FTH imaging is given in Sec. 2.7.

function (PSF) [Goo05]. The PSF $h(x', y'; x_0, y_0)$ is defined as the response of a system at point (x', y') in the output space to a point source, i.e. a δ-function, at the position (x_0, y_0) in the input space. By using the operator definition in Eq. 2.26, one obtains:

$$h(x', y'; x_0, y_0) = \mathcal{S}\{\delta(x - x_0, y - y_0)\} . \tag{2.35}$$

The general input–output relation of the imaging system is then given by the simple equation [Goo05]:

$$p_i(x', y') = \iint_{-\infty}^{\infty} o(x_0, y_0) h(x', y'; x_0, y_0) \, \mathrm{d}x_0 \mathrm{d}y_0 . \tag{2.36}$$

If in addition to the linearity, the imaging system is *space-invariant*, the PSF only depends on the distances $(x' - x_0)$ and $(y' - y_0)$ and the above equation turns into a convolution of the input function with the PSF:

$$p_i(x', y') = \iint_{-\infty}^{\infty} o(x_0, y_0) h(x' - x_0, y' - y_0) \, \mathrm{d}x_0 \mathrm{d}y_0 \tag{2.37}$$

$$= o * h . \tag{2.38}$$

In a space-invariant system, the image of a point source object changes only the position, but not its functional form if the point source is moved across the object plane. FTH imaging and most other imaging systems are space invariant only within a certain region being smaller than the full object field [Goo05]. In particular, under realistic experimental conditions when considering the nature of the detection (Sec. 2.6) or the influence of partial coherence (Sec. 2.7), space invariance in FTH is only valid in sub-regions of the reconstruction matrix, that is for small objects.

In order to obtain the PSF of the FTH imaging system, one has to apply the image formation process as described in Sec. 2.2 on a delta-like object at the position $\boldsymbol{r}_0 = (x_0, y_0)$, that is replacing $o(\boldsymbol{r} - \boldsymbol{r}_0)$ by $\delta(\boldsymbol{r} - \boldsymbol{r}_0)$ in Eq. 2.21. Using only the real image term of Eq. 2.23, the PSF is determined by:

$$h(\boldsymbol{r}'; \boldsymbol{r}_0) = \delta(\boldsymbol{r} - \boldsymbol{r}_0) * b^*(\boldsymbol{r}_0) \rho^*(-\boldsymbol{r}) \tag{2.39}$$

$$= b^*(\boldsymbol{r}_0) \rho^*(-\boldsymbol{r} - \boldsymbol{r}_0) , \tag{2.40}$$

where $\rho(\boldsymbol{r})$ is the transmission function of the reference structure. If the factor $b^*(\boldsymbol{r}_0)$, which reflects the illumination function, can be treated as constant—at least over the size of the object—, the imaging system is space invariant and can be described by a convolution with the reference. The PSF also serves as a measure for the spatial resolution of the imaging system. In the FTH case, the resolution is directly set by the size of the reference aperture.

Due to the convolution theorem, it is very simple to describe space-invariant systems also in Fourier space. A Fourier transform of Eq. 2.38 simply results in:

$$P_i(\boldsymbol{q}) = H(\boldsymbol{q})O(\boldsymbol{q})\,. \tag{2.41}$$

Here, $O(\boldsymbol{q})$ and $H(\boldsymbol{q})$ are the Fourier transforms of the object exit wave and the PSF, respectively. The function $H(\boldsymbol{q})$, called the *(amplitude) transfer function* of the imaging system[1], is identified with the Fourier transform of the reference exit wave. Hence, Eq. 2.41 states that the Fourier transform of the image (P_i) is formed by the superposition of exit waves of the object and the reference in the far-field. This statement is nothing else than the basic principle of Fourier-transform holography.

2.5 Magnetic contrast

One of the main application of x-ray FTH lies in the field of imaging magnetic samples with structure sizes between 50 nm and 1 µm. Magnetic contrast with x-rays is usually provided by the x-ray magnetic circular dichroism (XMCD). This effect describes a change of the resonant atomic scattering factor near absorption edges of a magnetized material in dependence on the helicity of the incident circularly polarized photons. Fundamentally, the XMCD goes back to a difference in the transition probability of a core electron to the first unoccupied spin-polarized states above the Fermi level when absorbing a left or right circularly polarized photon. The spin-polarization of the valence band, e.g. the $3d$ band in case of the elements Fe, Co, and Ni, is caused by the Stoner energy splitting of the spin-up and spin-down states which in fact is the origin of the material's magnetization. A very thorough explanation of the XMCD effect can be found in the book of Stöhr and Siegmann [Sto06]. Here, the influence on the radiation is again described in terms of absorption and phase shift. The definition of the refractive index (Eq. 2.4) for right (n_+) and left (n_-) circularly polarized light is therefore modified for the influence of the XMCD effect in the way:

$$n_\pm(\omega) = 1 - (\delta_0 \pm (\boldsymbol{\varepsilon}_k \cdot \boldsymbol{m})\,\Delta\delta) + \mathrm{i}(\beta_0 \pm (\boldsymbol{\varepsilon}_k \cdot \boldsymbol{m})\,\Delta\beta)\,. \tag{2.42}$$

Here, δ_0 and β_0 denote the optical constants for unpolarized or linearly polarized light, where the XMCD effect is not present. The sign of the corrections for circular polarization $\pm\Delta\delta$ and $\pm\Delta\beta$ to these constants depends on the helicity of the incident radiation. Similar to the usual optical constants, the correction constants are strongly dependent on the

1 It is very common to describe optical imaging system via transfer functions [Goo05]. As most imaging systems, e.g. microscopes and photo-cameras, rely on incoherent imaging and, thus, on the transport of intensity, usually the *optical transfer function (OTF)* is used which is the normalized auto-correlation of the amplitude transfer function. The modulus of the OTF is called the *modulation transfer function (MTF)*.

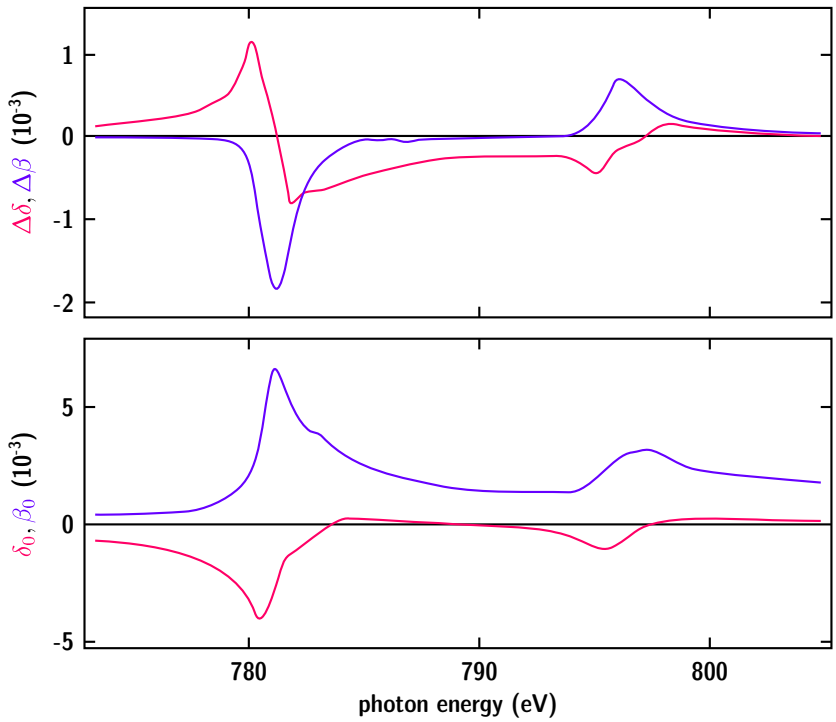

Figure 2.5: The optical constants δ_0 and β_0 of Co in the vicinity of the L_2 and L_3 absorption edges and the dichroic corrections $\Delta\delta$ and $\Delta\beta$ for magnetized media. The figure was reproduced from Ref. [Mer04].

photon energy (Fig. 2.5). The strength of the XMCD effect is additionally given by the orientation of the light's propagation direction $\boldsymbol{\varepsilon}_k = \boldsymbol{k}/|\boldsymbol{k}|$ (which is usually identified with the z-direction in this thesis) and the sample's magnetization direction $\boldsymbol{m}$. The orientations are connected with the scalar product, i.e. the effect is maximized for parallel or anti-parallel orientation and vanishes if the magnetization is perpendicular to the light propagation. Using Eq. 2.42 it is straight forward to obtain the transmission function for magnetic samples, following the consideration for Eq. 2.9:

$$t_\pm(x,y) \simeq 1 - \mu_\pm(x,y) - \mathrm{i}\phi_\pm(x,y)\,, \tag{2.43}$$

with the helicity dependent constants:

$$\mu_{\pm}(x,y) = \mu_0(x,y) \pm \Delta\mu(x,y) \tag{2.44}$$

$$= \frac{2\pi}{\lambda} \int_0^d \left[\beta_0(x,y,z) \pm (\boldsymbol{\varepsilon}_z \cdot \boldsymbol{m}(x,y,z))\, \Delta\beta(x,y,z)\right] \mathrm{d}z\,, \tag{2.45}$$

$$\phi_{\pm}(x,y) = \phi_0(x,y) \pm \Delta\phi(x,y) \tag{2.46}$$

$$= \frac{2\pi}{\lambda} \int_0^d \left[\delta_0(x,y,z) \pm (\boldsymbol{\varepsilon}_z \cdot \boldsymbol{m}(x,y,z))\, \Delta\delta(x,y,z)\right] \mathrm{d}z\,. \tag{2.47}$$

The constants $\mu_0(x,y)$ and $\phi_0(x,y)$ cover non-magnetic contributions, e.g. the height or material topology, whereas $\Delta\mu(x,y)$ and $\Delta\phi(x,y)$ provide the magnetic morphology of the sample. Usually the magnetic signal is weak compared to the non-magnetic variation. For this reason, it is favorable to remove all non-magnetic contributions by recording holograms with both positive and negative helicity of the light. The images showing magnetic contrast are then reconstructed from the difference of both holograms:

$$p = \frac{1}{2}\mathcal{F}^{-1}\left\{(\mathcal{F}\{b\rho + o_-\})^*\mathcal{F}\{b\rho + o_-\} - (\mathcal{F}\{b\rho + o_+\})^*\mathcal{F}\{b\rho + o_+\}\right\} \tag{2.48}$$

$$p = \frac{1}{2}\left(o_-^* * o_- - o_+^* * o_+ + b^*\rho^* * o_- + bo_-^* * \rho - b^*\rho^* * o_+ - bo_+^* * \rho\right)\,, \tag{2.49}$$

where o_+ and o_- characterize the sample's exit wave for positive and negative helicity of the light, respectively. The reference exit wave ρ shall be independent on the photon polarization.[1] Focusing on the image reconstruction formed by the reference–object cross-correlation and putting in the transmission function yields by analogy with Eq. 2.24:

$$p_i(x,y) = \frac{1}{2}\left\{b^*(1 - \mu_-(x,y) - \mathrm{i}\phi_-(x,y)) - b^*(1 - \mu_+(x,y) - \mathrm{i}\phi_+(x,y))\right\} \tag{2.50}$$

$$= \frac{1}{2}\left\{b^*(\mu_+(x,y) + \mathrm{i}\phi_+(x,y) - \mu_-(x,y) - \mathrm{i}\phi_-(x,y))\right\} \tag{2.51}$$

$$= b^*(\Delta\mu(x,y) + \mathrm{i}\Delta\phi(x,y))\,. \tag{2.52}$$

And analogously, the twin image:

$$p_i^*(x,y) = b(\Delta\mu(x,y) - \mathrm{i}\Delta\phi(x,y))\,. \tag{2.53}$$

1 The case of using a "magnetic" reference, i.e. a reference wave that is subjected to the XMCD effect, is of special interest when imaging with linearly polarized light, but still searching for magnetic contrast [Sac12].

The reconstruction of the difference hologram, thus, outputs an image containing purely magnetic information without any cross-talk from the sample topography. The magnetic contrast is observed either in the real part or the imaginary part of the reconstructed image:[1]

$$\operatorname{Re} p_i(x,y) = |b|\,\Delta\mu(x,y)\,, \tag{2.54}$$
$$\operatorname{Im} p_i(x,y) = |b|\,\Delta\phi(x,y)\,. \tag{2.55}$$

The magnitude $|p_i(x,y)| = |b|\,\sqrt{\Delta\mu^2(x,y) + \Delta\phi^2(x,y)}$ is not an appropriate channel as the sign of $\Delta\mu$ and $\Delta\phi$ reflecting the magnetization orientation is lost. The same holds for the phase $\arg p_i(x,y)$ as it only reflects the sign of the magnetization and—under experimental conditions including noise—becomes imprecise or even undefined for positions with low or zero magnitude. In the real and imaginary part, the reconstructed intensity values are *proportional to the z-component of the material's magnetization.*

Nevertheless using the real or imaginary part for magnetic contrast still has a number of drawbacks: (i) Since the dichroic parts of optical constants are heavily changing with the photon energy (Fig. 2.5), the magnetic contrast found either in the real or imaginary part is changing as well or may even vanish [Sch07a]. (ii) Real part and imaginary part are sensitive to an exactly known position of $\boldsymbol{q} = \mathbf{0}$ in the hologram in order to avoid any artificial phase modulation in the reconstruction. In a digital hologram, the position must be known with sub-pixel accuracy. (iii) If the illumination of the sample is not a plane wave, the reference wave will have a certain phase difference β [Sta08], i.e. $b = |b|\exp(\mathrm{i}\beta)$. The reconstruction will be affected by this phase shift and the observed magnetic contrast in the real and imaginary part is altered.

The way to analyze magnetic FTH images proposed in this work is to use a *signed magnitude*—a property which is insensitive to the implications above stated. The value is calculated either by rotating the reconstructed wave by an angle $-\alpha$ in the complex plane in a way that the real part shows the maximum contrast:

$$\mathcal{M}\{p_i(x,y)\} = \operatorname{Re}\{p_i(x,y)\exp(-\mathrm{i}\alpha)\} \tag{2.56}$$
$$= |b|(\Delta\mu(x,y)\cos\alpha + \Delta\phi(x,y)\sin\alpha) \tag{2.57}$$

or by calculating the magnitude signed by the sign of the real part:

$$\mathcal{M}\{p_i(x,y)\} = \operatorname{sgn}\Delta\mu(x,y)\,|p_i(x,y)| \tag{2.58}$$
$$= |b|\frac{\Delta\mu(x,y)}{|\Delta\mu(x,y)|}\,\sqrt{\Delta\mu^2(x,y) + \Delta\phi^2(x,y)}\,. \tag{2.59}$$

In the ideal case, the angle α in Eq. 2.57 is simply given by the phase of the reconstructed image at a certain position (x,y), i.e. $\alpha(x,y) = \arg p_i(x,y)$. In most cases, it is sufficient

1 It is assumed that b has only a small phase difference, i.e. $|b| \simeq \operatorname{Re} b$.

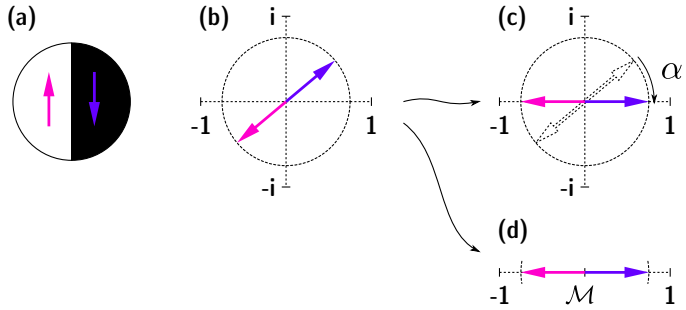

Figure 2.6: Illustration of the signed magnitude. **(a)** Model sample consisting of one up and one down magnetized region (domain). **(b)** Reconstructed exit wave values presented in the complex plane. Magnetic contrast is observed in the real and in the imaginary part of the reconstruction. The non-zero phase shift can be caused by (i) energy dependence of the optical constants, (ii) imprecise centering of the hologram, or (iii) a non-plane-wave illumination of the sample. The real and the imaginary parts have opposite signs, but equal magnitude in oppositely magnetized regions. The signed magnitude is calculated **(c)** by either rotating the reconstructed image by an angle α in the complex plane or **(d)** by using the magnitude together with the sign of the real part.

to choose a constant angle ($\alpha(x,y) = \alpha_0$) for the whole reconstructed image. In the second procedure (Eq. 2.59), the signed magnitude is always calculated locally.[1] Taking the real part as the reference for choosing the sign of the magnitude is motivated by the fact, that $\Delta\beta$ retains its sign over the L_2 or L_3 absorption edge whereas $\Delta\delta$ flips its sign where $\Delta\beta$ reaches its maximum magnitude (Fig. 2.5). It is important to note that the linearity between reconstructed intensity and z-component of the magnetization is not affected by the signed magnitude procedure.

If the illumination function features a certain phase difference β between the positions of the object and the reference source, the reconstructed image (Eq. 2.52) is affected by an additional phase term:

$$p_i(x,y) = |b| \exp(-\mathrm{i}\beta)(\Delta\mu(x,y) + \mathrm{i}\Delta\phi(x,y)) \,. \tag{2.60}$$

This phase difference can be removed by the signed magnitude procedure as well. In the case of procedure Eq. 2.57, one has to additionally rotate by the angle β, i.e. to multiply with $\exp(\mathrm{i}\beta)$. In Eq. 2.59, the phase term is already effectively removed by calculating the magnitude of $p_i(x,y)$.

In principle, the signed magnitude also removes phase gradients in the reconstructed image due to an improper centering of the hologram. But in practice, it turns out that it is more favorable to first remove the phase gradient as described in Ref. [SN09] and then take the signed magnitude using a constant angle α_0 for the whole reconstructed image.

1 In practice, "locally" refers to a single pixel in the digital reconstruction matrix.

In order to promote a better understanding of the signed magnitude contrast, a special, but experimentally important case of sample system shall be considered in the following. The sample shall consist of a thin-film, laterally uniform magnetic layer. Thus, the sample does not exhibit any element or topological contrast. Also the magnitude of the magnetization shall be considered as constant with the direction of magnetization mainly pointing out-of-plane, i.e. either parallel or anti-parallel to the $\boldsymbol{k}$-vector of the light with normal incidence to the film surface. At the boundary between oppositely magnetized domains, the magnetization direction gradually rotates by 180° over the width of the so-called domain wall. In this model case, the dichroic part of the constants in Eq. 2.45 and Eq. 2.47 and the magnetic contrast in Eq. 2.52 is solely varying with the cosine of the angle $\gamma(x, y)$ enclosed by the magnetization and the light propagation vector.

$$p_i(x, y) = b^* \frac{2\pi d}{\lambda} (\Delta\beta + \mathrm{i}\Delta\delta) \cos\gamma(x, y) \,. \tag{2.61}$$

When only considering the oppositely magnetized domains ($\cos\gamma = \pm 1$) and neglecting the domain walls, one obtains:

$$p_i(x, y) = \pm b^* \frac{2\pi d}{\lambda} (\Delta\beta + \mathrm{i}\Delta\delta) \,. \tag{2.62}$$

In Fig. 2.6 this situation is illustrated by considering a model sample consisting of two oppositely magnetized domains denoted by black and white color and by up and down arrows. The reconstructed complex exit wave values presented in the complex plane have equal magnitude but opposite sign. The strongest contrast is found when using the values for the magnitude, but provided with different sign in order to distinguish the differently magnetized regions.

The advantage of the signed-magnitude contrast representation becomes particularly apparent when monitoring the reconstructed magnetic information using different photon energies which is shown in Fig. 2.7. The energy-dependent values for $\Delta\delta$ and $\Delta\beta$ have been taken from Ref. [Mer04] (Fig. 2.5). The calculation of the reconstructed magnetic contrast of the model sample reveals that the contrast vanishes in the real or imaginary part of the reconstructed exit wave for certain energies and in case of the imaginary part even switches the sign. On the other hand, the signed magnitude always gives the best combined contrast.

Experimentally, the new signed magnitude procedure was first applied in Ref. [Pfa11]. In the next chapter all images presented have been processed in this way.

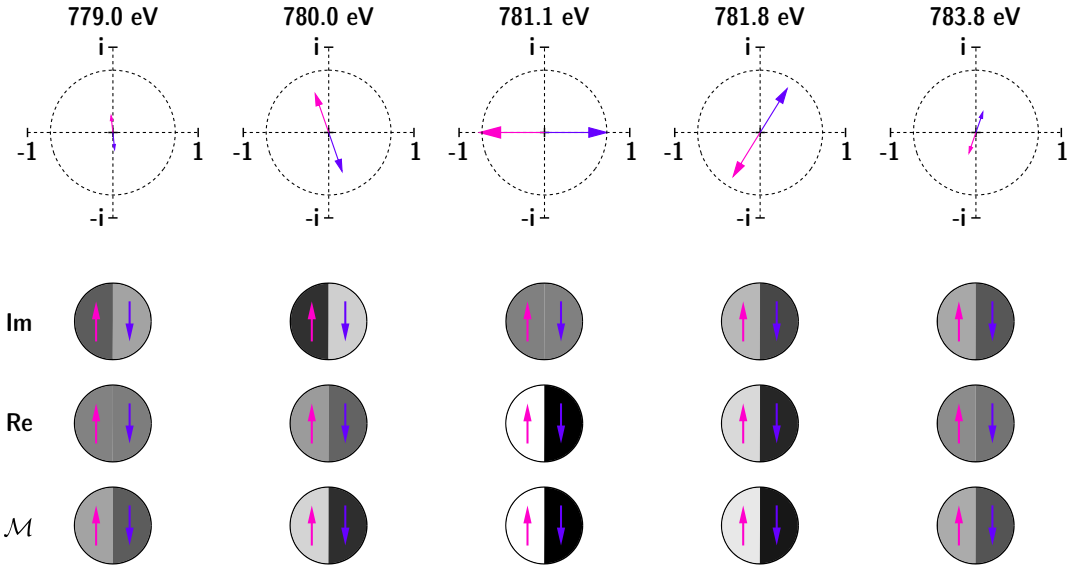

Figure 2.7: Calculated magnetic contrast as observed in the imaginary part, in the real part and in the signed magnitude of the reconstruction at different photon energies around an absorption edge, in this case the Co L_3-edge. The values for the optical constants were taken from Ref. [Mer04] as presented in Fig. 2.5. The model sample is the same as used in Fig. 2.6. The first image row shows the reconstructed values for two oppositely magnetized regions in the complex plane. The images beneath illustrate the reconstruction contrast yielded in the different channels. At every energy, the signed magnitude gives the highest contrast with consistent sign.

2.6 Digital holography

In traditional optical holography, the hologram is recorded on a photosentive material. In the x-ray range, on the other hand, today nearly exclusively CCD cameras are used with the advantage that the digitally stored hologram can be numerically reconstructed and manipulated in real time. In the lensless x-ray FTH technique, the CCD is the only "optical element" besides the optics mask in front of the sample. Therefore, the detection properties of the CCD have a large impact on the image formation. In particular, the influence of the CCD on the PSF, the FOV and the image contrast will be discussed in the following.

This section is based on Refs. [Guo03; Kel09; Kre02a; Kre02b] which deal with the problem of using CCDs and digital reconstruction in general holography with emphasis on the optical regime. In the following these findings will be applied to the case of soft x-ray FTH imaging.

For convenience, the notation of the three coordinate systems used in the last sections is also kept in the following calculation, i.e. (x, y) denotes the sample plane, (q_x, q_y) the

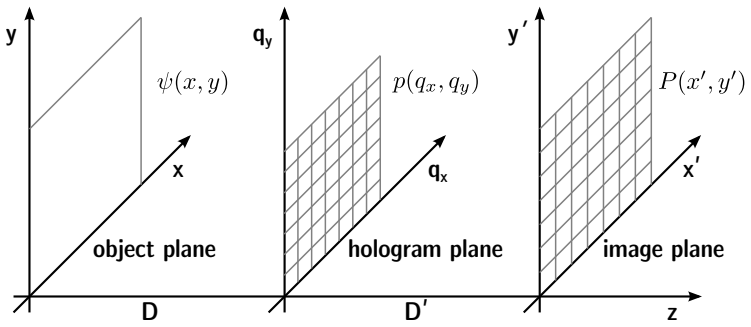

Figure 2.8: Coordinate systems and geometry of digital FTH. Adapted from [Kre02a].

hologram or detector plane and (x', y') the reconstruction coordinate system (Fig. 2.8). In particular, one should note that the CCD is described in reciprocal space units and the real space dimensions (ξ, η) of the device have to be translated into Fourier space. Although this description is less intuitive, it has the advantage that the geometry of the experiment, i.e. detector–sample distance and light wavelength, is already included.

A CCD of $N \times M$ pixels can be mathematically represented by a two-dimensional array

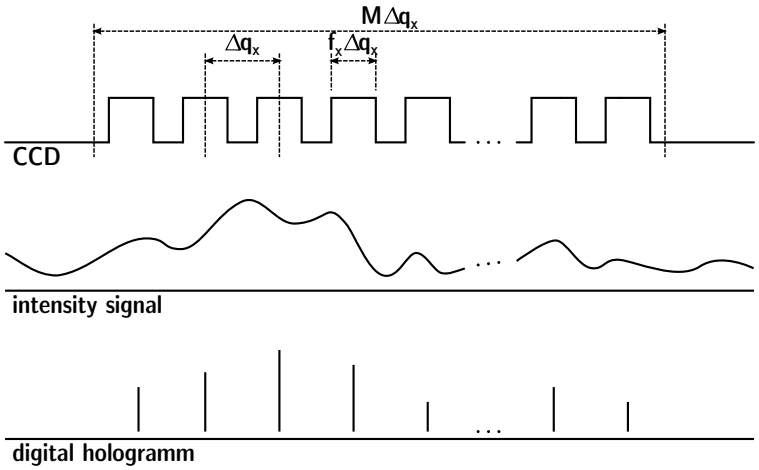

Figure 2.9: Mathematical (one-dimensional) representation of a pixelated CCD detector as a series (comb) of rect functions. The continuous intensity distribution is integrated over the area of each pixel and is then represented by a comb of delta functions scaled by the integrated intensity.

of rect functions [Kre02a]:

$$\left[\frac{1}{\Delta q_x\,\Delta q_y}\,\mathrm{rect}\left(\frac{q_x}{f_x\Delta q_x},\frac{q_y}{f_y\Delta q_y}\right) * \frac{1}{\Delta q_x\,\Delta q_y}\,\mathrm{comb}\left(\frac{q_x}{\Delta q_x},\frac{q_y}{\Delta q_y}\right)\right] \times \frac{1}{\Delta q_x\,\Delta q_y}\,\mathrm{rect}\left(\frac{q_x}{N\Delta q_x},\frac{q_y}{M\Delta q_y}\right). \tag{2.63}$$

The two-dimensional rect and comb functions are given by:

$$\mathrm{rect}(x,y) = \begin{cases} 0 & |x| > \frac{1}{2} \text{ or } |y| > \frac{1}{2} \\ 1 & |x| \le \frac{1}{2} \text{ and } |y| \le \frac{1}{2} \end{cases} \tag{2.64}$$

$$\mathrm{comb}(x,y) = \sum_{n,m=-\infty}^{\infty} \delta(x-n)\,\delta(x-m) \quad \text{with } n,m \in \mathbb{Z}\,. \tag{2.65}$$

The first rect term in Eq. 2.63 represents a single pixel with the dimensions $(f_x\Delta q_x, f_y\Delta q_y)$, where (f_x, f_y) are the fill factors of the CCD in q_x and q_y direction, respectively, with possible values between 0 and 1. The convolution (indicated by the $*$ symbol) with the comb function produces a periodic array of these pixels with a periodicity of $(\Delta q_x, \Delta q_y)$. The periodicity in Fourier space can be calculated from the real periodicity of the pixels $(\Delta\xi, \Delta\eta)$—which in the case of $f_x = f_y = 1$ is identical to the pixel size—by using Eq. 2.1 for very small diffraction angles, where $\theta \simeq \sin\theta$:

$$\Delta q_x = \frac{2\pi}{\lambda D}\,\Delta\xi\,, \qquad \Delta q_y = \frac{2\pi}{\lambda D}\,\Delta\eta\,. \tag{2.66}$$

The multiplication (indicated with the $\times$ symbol) with the second rect function in Eq. 2.63 limits the array to the total size of the detector. The pre-factors of the rect and comb functions are needed for the normalization. In this representation, each pixel has a weight of $f_x f_y$ and a sum over the whole CCD would give the total number of pixels if $f_x = f_y = 1$. In Fig. 2.9 this mathematical representation is illustrated for the one-dimensional case.

An intensity signal, i.e. the hologram $P(q_x, q_y)$, detected by the CCD is periodically sampled as a two-dimensional array of discrete intensity values. In each pixel the intensity is integrated over the pixel size $(f_x\Delta q_x \times f_y\Delta q_y)$. This integration can be performed as a convolution with the rect function representing a detector pixel and the *digital* hologram P' is expressed as [Guo03]:

$$P'(q_x,q_y) = \frac{1}{\Delta q_x\,\Delta q_y}\,\mathrm{rect}\left(\frac{q_x}{N\Delta q_x},\frac{q_y}{M\Delta q_y}\right)\frac{1}{\Delta q_x\,\Delta q_y}\,\mathrm{comb}\left(\frac{q_x}{\Delta q_x},\frac{q_y}{\Delta q_y}\right) \times P(q_x,q_y) * \frac{1}{\Delta q_x\,\Delta q_y}\,\mathrm{rect}\left(\frac{q_x}{f_x\Delta q_x},\frac{q_y}{f_y\Delta q_y}\right). \tag{2.67}$$

The influence of the digital sampling of the hologram on the image reconstruction is investigated by determination of the PSF (Sec. 2.4) in the image domain. Note that this calculation is different from determining the detector's $\overline{\text{PSF}}$ for direct imaging purposes.[1] In this case the $\overline{\text{PSF}}$ is the response of the CCD on a single-photon event and has to be determined experimentally. In the following calculation, fully coherent and monochromatic light is assumed and the noise of the CCD detection is excluded.

To determine the PSF, the sample function consists of a delta-like object $o(x, y; x_0, y_0)$ located at the position (x_0, y_0) and a delta-like reference $\rho(x, y)$ located at the origin of the sample plane:

$$o(x, y; x_0, y_0) = \delta(x - x_0, y - y_0) \tag{2.68}$$

$$\rho(x, y) = \delta(x, y). \tag{2.69}$$

Assuming Fraunhofer diffraction (Eq. 2.14), the hologram $P(q_x, q_y, x_0, y_0)$ is expressed as the magnitude squared of the Fourier transform of the sample function which is the sum of the object and the reference (Eq. 2.17):

$$\begin{aligned} P(q_x, q_y; x_0, y_0) &= \mathcal{F}[o(x, y; x_0, y_0) + \rho(x, y)]\mathcal{F}^*[o(x, y; x_0, y_0) + \rho(x, y)] && (2.70)\\ &= (\exp[-\mathrm{i}(q_x x_0 + q_y y_0)] + 1)(\exp[\mathrm{i}(q_x x_0 + q_y y_0)] + 1) && (2.71)\\ &= 2 + \exp[-\mathrm{i}(q_x x_0 + q_y y_0)] + \exp[\mathrm{i}(q_x x_0 + q_y y_0)]\,. && (2.72) \end{aligned}$$

If this hologram is reconstructed by an inverse Fourier transform, the first term will lead to the auto-correlation term in the image plane origin, the second term gives the separated real image of the delta-like object and the third term the corresponding twin image. For the calculation of the image PSF, it is sufficient to focus on the second term producing the real image. Using Eq. 2.67, the digital sampling of this part is expressed as:

$$\begin{aligned} P'_{\text{real}}(q_x, q_y; x_0, y_0) = {} & \frac{1}{\Delta q_x\, \Delta q_y} \operatorname{rect}\left(\frac{q_x}{N\Delta q_x}, \frac{q_y}{M\Delta q_y}\right) \frac{1}{\Delta q_x\, \Delta q_y} \operatorname{comb}\left(\frac{q_x}{\Delta q_x}, \frac{q_y}{\Delta q_y}\right) \\ & \times \exp[-\mathrm{i}(q_x x_0 + q_y y_0)] * \frac{1}{\Delta q_x\, \Delta q_y} \operatorname{rect}\left(\frac{q_x}{f_x \Delta q_x}, \frac{q_y}{f_y \Delta q_y}\right). \end{aligned} \tag{2.73}$$

1 Unfortunately, the terminology of *point spread function* is equally used in both domains, but with different meaning. In this work, the difference is made clear by using the overline in the hologram domain (reciprocal space). The same holds for the *transfer function* term.

The inverse Fourier transform of P'_{real} gives the PSF in the real image:

$$h_{\text{real}}(x', y'; x_0, y_0) = \mathcal{F}^{-1}[P'_{\text{real}}(q_x, q_y; x_0, y_0)] \tag{2.74}$$

$$= f_x f_y \operatorname{sinc}\left(\frac{f_x}{2\pi}\Delta q_x\, x', \frac{f_y}{2\pi}\Delta q_y\, y'\right) \delta(x' - x_0, y' - y_0)$$
$$* MN \operatorname{sinc}\left(\frac{N}{2\pi}\Delta q_x\, x', \frac{M}{2\pi}\Delta q_y\, y'\right)$$
$$* \operatorname{comb}\left(\frac{1}{2\pi}\Delta q_x\, x', \frac{1}{2\pi}\Delta q_y\, y'\right) . \tag{2.75}$$

Here, the normalized, two-dimensional sinc function is used:

$$\operatorname{sinc}(x, y) = \frac{\sin(\pi x)}{\pi x}\frac{\sin(\pi y)}{\pi y} \tag{2.76}$$

The last term in Eq. 2.75 causes a periodic continuation of the reconstruction and generates multiple identical images. This periodicity is a result of the finite sampling by the CCD detector. For the first copy[1]—as it is computed by all numerical Fourier transform functions—the term is replaced by $\delta(x', y')$. Finally, the PSF becomes:

$$h_{\text{real}}(x', y'; x_0, y_0) = f_x f_y MN \operatorname{sinc}(\frac{f_x}{2\pi}\Delta q_x\, x', \frac{f_y}{2\pi}\Delta q_y\, y')$$
$$\times \operatorname{sinc}(\frac{N}{2\pi}\Delta q_x\,(x' - x_0), \frac{M}{2\pi}\Delta q_y\,(y' - y_0)) . \tag{2.77}$$

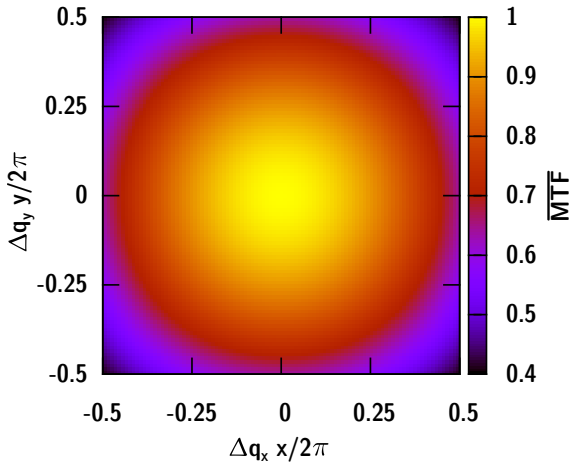

Figure 2.10: $\overline{\text{MTF}}$ of the CCD with $f_x = f_y = 1$, corresponding to the first sinc term in Eq. 2.77. The presented region corresponds to the full reconstruction area.

1 By analogy with x-ray crystallography, the first copy can be identified with the first Brillouin zone of the reciprocal lattice of the CCD pixel array.

The first sinc function varies only slowly over the reconstruction area and influences the intensity of the reconstruction or—when related to a noise background—contrast of the reconstruction. Especially towards the edges and corners of the reconstruction matrix, this contrast is rapidly decreasing (Fig. 2.10). The contrast reduction is the result of the decreasing ability of the detector to sample high-frequency intensity modulations that arise from large sample–reference distances. Hence, this term is called the modulation transfer function ($\overline{\text{MTF}}$) of the CCD [Pfa10a]. Following the Nyquist-Shannon-Theorem [But06; Pre07], the smallest intensity period that can be sampled by the CCD is $2\Delta q_x$ or $2\Delta q_y$ corresponding to a real space distance of:

$$x_{\max} = \frac{\lambda D}{2\Delta\xi}\,, \qquad y_{\max} = \frac{\lambda D}{2\Delta\eta}\,. \tag{2.78}$$

Note, that due to the additional copies of the reconstruction given by the comb function in Eq. 2.75, also data with higher frequency is projected from the second Brillouin zone into the first one. This effect is known as *aliasing* [But06; Pre07] and can be frequently observed in simulations of FTH experiments. In general, the $\overline{\text{MTF}}$ is given by the Fourier transform of the detector's $\overline{\text{PSF}}$. In the simplest case the $\overline{\text{PSF}}$ is identified with the shape and size of a single CCD pixel resulting in the sinc function obtained in Eq. 2.77.

The second term in Eq. 2.77 results from the size and the shape of the whole detector which is rectangular as well and again produces a sinc function in its Fourier transformation. This part of Eq. 2.77 gives the main contribution to the PSF caused by the detector. The

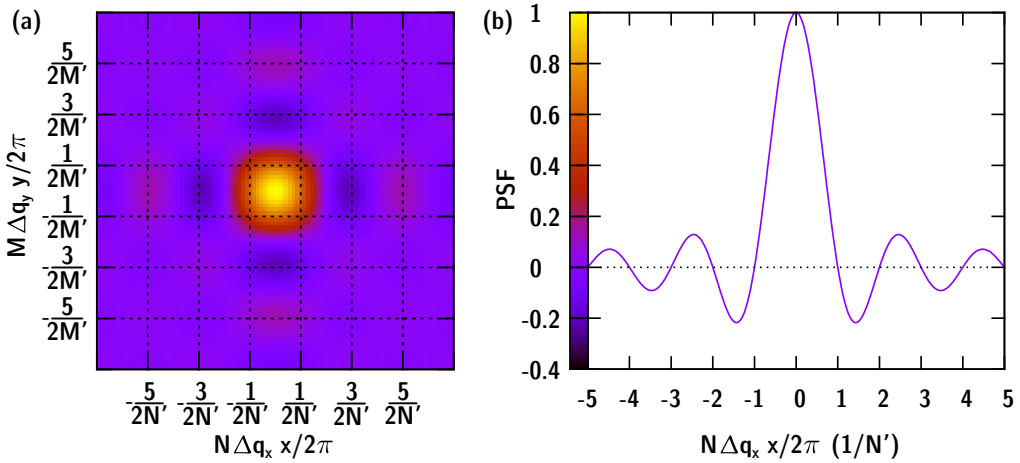

Figure 2.11: PSF in the image domain caused by the size of the CCD corresponding to the second sinc term in Eq. 2.77. **(b)** Slice along the x-direction at $y = 0$ of the 2D data as presented in **(a)**. The offset (x_0, y_0) in Eq. 2.77 was omitted. The mesh in (a) corresponds to the pixel resolution in the image plane when zero-padding is not applied, i.e. $N' = N$ and $M' = M$. In this case, the main part of the PSF is confined within a single pixel, a finding that is related to Nyquist-Shannon sampling theorem.

sinc function constitutes the reconstructed image of the delta-like object $o(x, y; x_0, y_0)$ and is, therefore, found at the position (x_0, y_0). As depicted in Fig. 2.11, the delta-like object appears broadened due to the limited size of the detector. The broadening directly affects the spatial resolution that can be achieved in the experiment. In addition to the broadening, side maxima and minima appear.

In Eq. 2.75 the Fourier transformation of the hologram was carried out via the unbounded Fourier integral. In practice, the reconstruction $p'(x', y')$ is computed numerically using the discrete 2D Fourier transform [But06; Pre07] as an $N \times M$ matrix:

$$p'(n\Delta x', m\Delta y') = \sum_{k=0}^{N-1} \sum_{l=0}^{M-1} H'(k\Delta q_x, l\Delta q_y) \exp[\mathrm{i}(k\Delta q_x\, n\Delta x' + l\Delta q_y\, m\Delta y')] \,, \tag{2.79}$$

where the scaling lengths $\Delta x' = 2\pi/(N\Delta q_x)$, $\Delta y' = 2\pi/(M\Delta q_y)$ define the sampling in the image plane. Omitting the scaling lengths one can write:

$$p'_{m,n} = \sum_{k=0}^{N-1} \sum_{l=0}^{M-1} H'_{k,l} \exp[2\pi\mathrm{i}(kn/N + lm/M)] \,. \tag{2.80}$$

The summation is carried out at least over all CCD pixels ($N \times M$), but the range can be also increased to a larger matrix of $N' \times M'$ elements leading to a finer sampling in the image plane (Fig. 2.11). This process is called *zero-padding* [But06]. One has to be aware that this procedure will only influence the sampling, but not the detector resolution i.e. the width of the PSF. The unbounded integral in Eq. 2.75 can be seen as the limit of infinite zero-padding and, hence, infinitesimal small (continuous) sampling in the image plane. In Fig. 2.11 the PSF due to an $M \times N$ pixel CCD detector is shown together with the pixel size in the image plane when the hologram is not zero-padded. Obviously, the main part of the PSF fits exactly within one pixel. This result is well known in a way that the resolution of an optical system is limited by the maximum detected scattering angle which in the present case is given by the size of the CCD ($N\Delta q_x \times M\Delta q_y$). Considering that two features (e.g. two δ-functions) must have a distance of at least two pixels in the reconstruction in order to be distinguished, the CCD resolution is calculated as:

$$x_{\min} = \frac{4\pi}{N\Delta q_x} = \frac{2\lambda D}{N\Delta\xi} \,, \qquad y_{\min} = \frac{4\pi}{M\Delta q_y} = \frac{2\lambda D}{M\Delta\eta} \qquad . \tag{2.81}$$

Eq. 2.78 and Eq. 2.81 treating the largest and the smallest real-space distance that can be sampled, respectively, can be combined to:

$$\frac{x_{\max}}{x_{\min}} = \frac{N}{4} \,, \qquad \frac{y_{\max}}{y_{\min}} = \frac{M}{4} \,. \tag{2.82}$$

The ratio between the maximum distance that can be sampled (and this gives an upper limit for the sample–reference distance) and the resolution in an FTH experiment cannot

exceed $N/4$ (or $M/4$ in the y-direction). In particular, this ratio is independent of the wavelength, sample–detector distance and detector pixel size, although for a particular wavelength and a particular detector a proper distance has to be chosen to achieve the optimum ratio in the experiment.

2.7 X-ray coherence

In the previous sections, it was assumed that the incoming x-ray beam is fully coherent. In general, coherence is the condition for observing a stationary interference pattern of two overlapping waves on a detector. Under full coherence, the light is assumed to be perfectly monochromatic and produced by a point source infinitely far away from the sample. Obviously, this is not the case for real x-ray beams, as all x-ray sources rely on spontaneous emission and therefore have a certain spectral width and a certain extent over which the radiation is emitted [Len01]. Due to this reason, the interference pattern, i.e. the hologram, is at least partially "washed out" on the detector and the quality of the image reconstruction is degraded.

The coherence properties of a light source are usually discussed in terms of *temporal* and *spatial* coherence. The temporal, also called longitudinal, coherence is given by the spectral width of the radiation while the spatial (or transversal) coherence is connected with the size of the source. In a very basic description, both properties are quantified by a coherence length. In an x-ray holography experiment, the temporal coherence length mainly translates into the maximum diffraction angle which interference can be observed under. The spatial coherence length gives a measure for the maximum distance between sample and reference wave origin that can be used. Although this description of coherence might be sufficient to design a proper experimental setup, the influence of partial coherence on the image quality can not be treated with this concept. For this task, one has to employ a more sophisticated concept namely a description via correlation functions of the light field. An extensive treatment of this topic can be found e.g. in [Bor99; Goo85] but also in every other textbook on advanced optics. The following considerations therefore focus on the main results and in particular on the implications on an FTH experiment. As already done before (Sec. 2.4, 2.6), these implication will be quantified by the influence of partial coherence on the PSF.

2.7.1 The general interference law

By analogy with the complex representation of a plane wave, the polychromatic light field at a fixed point in space Q may be expressed in form of a Fourier integral:

$$\psi(Q,t) = \int_{-\infty}^{\infty} \tilde{\psi}(Q,\omega)\exp(-\mathrm{i}\omega t)\,\mathrm{d}\omega \tag{2.83}$$

where the complex $\tilde{\psi}(Q,\omega)$ describe the amplitude and phase of each spectral component. As polarization effects should be omitted for now $\tilde{\psi}$ is treated as a scalar. The intensity of the light field at the position Q is given by:

$$I(Q) = \langle \psi^*(Q,t)\psi(Q,t)\rangle \,, \tag{2.84}$$

where the angle brackets denote an averaging over times much longer than the temporal fluctuations of the electromagnetic field.

It is now assumed that the light reaches Q through two point-like apertures at the positions P_1 and P_2 (Fig. 2.12). The light field in Q is then expressed by a superposition of the light field at the positions P_1 and P_2, each suitably propagated and delayed:

$$\psi(Q,t) = K_1\psi\left(P_1, t-t_1\right) + K_2\psi\left(P_2, t-t_2\right) \,. \tag{2.85}$$

K_1 and K_2 are complex constants called the propagators. Basically, they are dependent on the size of the pinholes and on the distances (r_i) between the points P_i and Q. The time delays t_i are readily calculated from these distances as $t_i = r_i/c$. At this point, it shall already be noted that this arrangement of two pinholes and a screen (detector) will not only serve as a model for deriving the coherence properties of the light field as done in the following, but this model is already suitable for also obtaining the influence of partial coherence on the optical system's PSF.

Using Eq. 2.84, the intensity of the light at Q becomes:

$$\begin{aligned} I(Q) =& K_1^* K_1 \langle \psi^*\left(P_1, t-t_1\right)\psi\left(P_1, t-t_1\right)\rangle + K_2^* K_2 \langle \psi^*\left(P_2, t-t_2\right)\psi\left(P_2, t-t_2\right)\rangle \\ &+ K_1^* K_2 \langle \psi^*\left(P_1, t-t_1\right)\psi\left(P_2, t-t_2\right)\rangle \\ &+ K_2^* K_1 \langle \psi^*\left(P_2, t-t_2\right)\psi\left(P_1, t-t_1\right)\rangle \end{aligned} \tag{2.86}$$

The first two terms can be identified by the intensities ($I_i(Q)$) each pinhole would separately generate at the position Q. Additionally, for the cross-correlation terms the definition of the *mutual coherence function* is introduced:

$$\Gamma_{12}(\tau) = \langle \psi^*\left(P_1, t+\tau\right)\psi\left(P_2, t\right)\rangle \,, \tag{2.87}$$

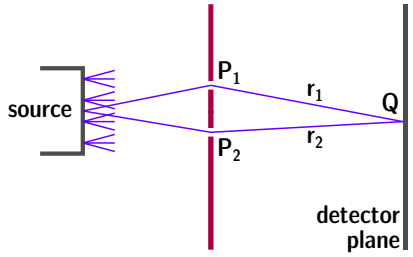

Figure 2.12: Geometry for deriving the general interference law. Reproduced from Ref. [Goo85].

with τ being the time delay between both beams in Q. Eq. 2.86 can be now written as:

$$I(Q) = I_1(Q) + I_2(Q) + 2|K_1 K_2| \mathrm{Re}\, \Gamma_{12}(\tau)\,. \tag{2.88}$$

If both pinholes coincide ($P_1 = P_2$) one obtains the self-coherence of the light field:

$$\Gamma_{11}(\tau) = \langle \psi^*\,(P_1, t+\tau)\,\psi\,(P_1, t)\rangle\,, \tag{2.89}$$

and one further realizes that:

$$\Gamma_{11}(0) = I_1(P_1) \qquad \text{and} \qquad I_1(Q) = |K_1|^2 I_1(P_1) = |K_1|^2 \Gamma_{11}(0)\,. \tag{2.90}$$

It is thus common to normalize the mutual coherence function in such a way that:

$$\gamma_{12}(\tau) = \frac{\Gamma_{12}(\tau)}{\sqrt{\Gamma_{11}(0)\Gamma_{22}(0)}}\,. \tag{2.91}$$

The correlation function γ_{12} is called the *complex degree of coherence*. Now Eq. 2.88 turns into the *general interference law for stationary optical fields*:

$$I(Q) = I_1(Q) + I_2(Q) + 2\sqrt{I_1(Q) I_2(Q)}\,\mathrm{Re}\,\gamma_{12}(\tau)\,. \tag{2.92}$$

Both, the temporal and spatial coherence properties are included in the single factor $\gamma_{12}(\tau)$. In order to point out the impact of $\gamma_{12}(\tau)$ on the interference pattern, it is convenient to use a somewhat different expression. Let $\bar{\omega}$ be the center frequency of the light spectrum; one can always write:

$$\gamma_{12}(\tau) = |\gamma_{12}(\tau)| \exp\{-\mathrm{i}[\bar{\omega}\tau - \alpha_{12}(\tau)]\}\,, \tag{2.93}$$

if

$$\alpha_{12}(\tau) = \bar{\omega}\tau + \arg \gamma_{12}(\tau)\,, \tag{2.94}$$

and the interference law becomes:

$$I(Q) = I_1(Q) + I_2(Q) + 2\sqrt{I_1(Q) I_2(Q)}|\gamma_{12}(\tau)| \cos[\bar{\omega}\tau - \alpha_{12}(\tau)]\,. \tag{2.95}$$

When considering a sufficiently narrow spectrum of the light, the phase factor $\exp(-\mathrm{i}\bar{\omega}\tau)$ will produce the well known cosine-shaped interference fringes due to the time delay between the two beams. The remaining part $|\gamma_{12}(\tau)|$ will limit the contrast between the maxima and minima of the interference pattern by an slowly varying envelope which is directly related to the spectrum of the radiation and to the spatial coherence between the points P_1 and P_2. Thus, by measuring the interference contrast commonly known as the visibility, it is possible to directly determine $\gamma_{12}(\tau)$ experimentally. For a fully coherent beam $|\gamma_{12}(\tau)|$ equals unity, for partially coherence it is smaller and it vanishes

for incoherent conditions.

In order to gain a better understanding of $\gamma_{12}(\tau)$ it is useful to separately discuss the temporal and spatial coherence properties.

2.7.2 Temporal coherence

For the analysis of the temporal coherence, the previously discussed arrangement is first reduced to the case were the position of the two pinholes coincides, but a certain time delay betweens the beams is introduced. This arrangement is known as the Michelson interferometer. In this case the interference law in Eq. 2.92 reduces to:

$$I(Q) = 2I_1(Q)\,(1 + \mathrm{Re}\,\gamma(\tau)) \tag{2.96}$$

where $\gamma(\tau)$ is the normalized time-correlation function of the light field, called the *normalized self-coherence function*, and is given by

$$\gamma(\tau) = \frac{\Gamma(\tau)}{\Gamma(0)} \qquad \text{with} \qquad \Gamma(\tau) = \langle \psi^*\,(Q, t+\tau)\,\psi\,(Q,t)\rangle\,. \tag{2.97}$$

Via a Fourier transform both quantities are connected to spectral properties of the light field:

$$\Gamma(\tau) = \int_{-\infty}^{\infty} S(\omega)\exp(-\mathrm{i}\omega\tau)\mathrm{d}\omega \qquad \text{and} \qquad \gamma(\tau) = \int_{-\infty}^{\infty} s(\omega)\exp(-\mathrm{i}\omega\tau)\mathrm{d}\omega\,. \tag{2.98}$$

$S(\omega)$ is called the *spectral density* or *power spectrum* of the light field, $s(\omega)$ is the *normalized spectral density*. Eq. 2.98 is known as the Wiener-Khintchine theorem. Using Eq. 2.83 one also finds $S(\omega) = |\tilde{\psi}(\omega)|^2$. Thus, the spectral density can be also seen as a frequency-space analogue to the intensity and the interference law (Eq. 2.92) exists for the spectral density as well:

$$S(Q,\omega) = S_1(Q,\omega) + S_2(Q,\omega) + \sqrt{S_1(Q,\omega)S_2(Q,\omega)}w_{12}(\omega)\,, \tag{2.99}$$

where $w_{12}(\omega)$ is called the *spectral degree of coherence*. It is the normalized version of the *cross-spectral density* given by the Fourier transform of the mutual coherence function:

$$w_{12} = \frac{W_{12}(\omega)}{\sqrt{S_1(Q,\omega)S_2(Q,\omega)}} \qquad \text{with} \qquad W_{12} = \int_{-\infty}^{\infty} \Gamma_{12}(\tau)\exp(-\mathrm{i}\omega\tau)\mathrm{d}\omega\,. \tag{2.100}$$

Although the following discussion will focus on narrow-band light, it shall be briefly commented also on interference of broad-band illumination as it is described by the spectral interference law in Eq. 2.99. While in a double slit experiment using monochromatic light, the intensity is modulated on the detector as expressed by Eq. 2.92, in the case of a white

illumination the spectrum of the light is affected. This effect is well known from, e.g., the dispersion of light at a diffraction grating. There have been attempts to use a white x-ray illumination together with an energy-dispersive detector for coherent diffraction experiments as well [Pie05].

Coming back to the case of a narrow light spectrum $s(\omega)$ with a center frequency $\bar{\omega}$, one can transform Eq. 2.96 analogously to Eq. 2.95:

$$I(Q) = 2I_1(Q)\{1 + |\gamma(\tau)| \cos[\bar{\omega}\tau - \alpha(\tau)]\} \,. \tag{2.101}$$

When scanning the delay τ between the two beams the intensity oscillates according to $\cos(\bar{\omega}\tau)$. In addition the amplitude of the oscillation is modulated by $|\gamma(\tau)|$ which is given by the Fourier transform of the spectral density (Eq. 2.98). Depending on the shape of the spectrum, e.g. Gaussian, Lorentzian or rectangular, the envelope of the oscillation also changes its appearance. However, the width of the envelope is always on the order of $\tau_\mathrm{c} \simeq 1/\Delta\nu$ with $\Delta\nu$ being the frequency bandwidth of the light spectrum. τ_c is called the *coherence time*. From the coherence time the longitudinal coherence length is obtained as:

$$l_\mathrm{l} = c\tau_\mathrm{c} \simeq \bar{\lambda}^2/\Delta\lambda \,. \tag{2.102}$$

At a soft x-ray synchrotron beamline where the light is delivered with a spectral purity $(E/\Delta E)$ of more than 1000 the longitudinal coherence lengths are on the order of 1 µm to 10 µm.

2.7.3 Spatial coherence

The spatial coherence properties of a light source are best investigated under quasi-monochromatic conditions. These conditions are fulfilled if the spectrum of the illumination is so narrow that the coherence time is much longer than the maximum time delay occurring in the experiment. In this case, the complex degree of coherence can be rewritten as:

$$\gamma_{12}(\tau) \cong \mu_{12} \exp(\mathrm{i}\bar{\omega}\tau) \,, \tag{2.103}$$

with

$$\mu_{12} = \gamma_{12}(0) = \frac{\langle \psi^*(P_1,t)\, \psi(P_2,t) \rangle}{\sqrt{I_1(P_1) I_2(P_2)}} \,, \tag{2.104}$$

which is the normalized spatial correlation function of the light field, called the *complex coherence factor*. In general, μ_{12} depends on the nature of the source and its properties. But for the case of an incoherent (chaotic) source which consists of an extended collection of independent radiators, the complex coherence factor is related to the intensity distribution

of the source $I(u, v)$ by the van Cittert-Zernicke theorem:

$$\mu(\Delta x, \Delta y) = \frac{\exp(-\mathrm{i}\phi) \iint_{-\infty}^{\infty} I(u, v) \exp\left[\mathrm{i}\frac{2\pi}{\bar{\lambda} z}(\Delta x\, u + \Delta y\, v)\right] \mathrm{d}u\mathrm{d}v}{\iint_{-\infty}^{\infty} I(u, v)\, \mathrm{d}u\mathrm{d}v} \,. \tag{2.105}$$

The theorem states that for a chaotic source (i) the coherence factor depends only on the relative position $(\Delta x, \Delta y)$ of the two points P_1 and P_2 in the sample plane and not on their absolute positions[1] and (ii) the coherence factor is given by the normalized Fourier transform of the source's spatial intensity distribution $I(u, v)$. By analogy with the coherence time, one can also define a transversal coherence area A_{tr} at the distance z from the source which covers the transverse area A_{S}:[2]

$$A_{\mathrm{tr}} = \frac{\bar{\lambda}^2 z^2}{A_{\mathrm{S}}} \,. \tag{2.106}$$

Experimentally, the coherence factor was determined only for very few synchrotron beamlines [Pat01; Sin08; Tra05; Tra07]. The spatial coherence strongly depends on the beamline slit settings defining the source size, on the photon energy [Len01], and on the overall geometry. The relative distance of two points P_1 and P_2 where the coherence factor falls below 0.5 is typically on the order of 20 µm for a synchrotron beamline operated at 1 keV to 2 keV.

2.7.4 Implications for holographic imaging

In the following, the principles of partial coherence as outlined in the previous sections shall be applied to the case of FTH imaging. By analogy with Sec. 2.6, the influence of partial coherence on the PSF (Sec. 2.4) of the imaging system is investigated. Again, the reference source as well as the object are assumed to be δ-like transmission structures separated by the vector $\boldsymbol{r}_0$. Following the general interference law (Eq. 2.92) the signal measured on the detector is then given by:

$$I(\boldsymbol{q}) = I_1\{2 + \gamma_{12}(\tau) + \gamma_{12}^*(\tau)\} \,. \tag{2.107}$$

The intensity I_1 is identified with the intensity of the light field propagated from the pinhole to the detector. For a δ-like pinhole the intensity is constant over the whole $\boldsymbol{q}$-space. Due to the interference of the light emitted by the two pinholes, the intensity distribution is modulated according to the coherence properties of the light expressed in γ_{12}. The occurring time delays τ depend on the position on the detector which is, in turn,

1 The phase factor $\exp(-\mathrm{i}\phi)$ arises due to a path length difference from the source to the points P_1 and P_2 and can be neglected for large distances from the source.

2 In one dimension, it is possible to define the transversal coherence length as: $l_{\mathrm{tr}} = \bar{\lambda} z / l_{\mathrm{S}}$ where l_{S} denotes the source size in this dimension.

represented by the momentum transfer $\boldsymbol{q}$. The FTH reconstruction is obtained via a Fourier transform of the intensity pattern. As already outlined (Eq. 2.23), the cross-correlations $\gamma_{12}(\tau)$ and $\gamma_{12}^*(\tau)$ form the image and the twin image, respectively, while the constant offset $2I_1$ results in the object's auto-correlation. The PSF of the real image is thus given by:

$$h_{\mathrm{real}}(\boldsymbol{r}';\boldsymbol{r}_0) = \mathcal{F}^{-1}\{\gamma_{12}(\tau)\}\,. \tag{2.108}$$

Under certain conditions, in particular including a narrow spectrum of the light, one finds that the coherence factor $\gamma_{12}(\tau)$ separates into a temporal and a spatial part as discussed in Secs. 2.7.2 and 2.7.3. This separation called *reducibility* of the coherence factor is in detail treated in Ref. [Goo85] and is assumed to be valid for the following calculation:

$$\gamma_{12}(\tau) = \mu_{12}\gamma(\tau)\,. \tag{2.109}$$

In addition, it is assumed that μ_{12} only depends on the separation $\boldsymbol{r}_0$ of both pinholes, but not on their absolute positions, i.e. $\mu_{12} = \mu(\boldsymbol{r}_0)$, as it is suggested by the van Cittert-Zernicke theorem (Eq. 2.105). Expanding the Fourier transform gives:

$$h_{\mathrm{real}}(\boldsymbol{r}';\boldsymbol{r}_0) = \mu(\boldsymbol{r}_0)\iint_{-\infty}^{\infty}\gamma(\tau)\exp(\mathrm{i}\bar{\boldsymbol{q}}\boldsymbol{r}')\,\mathrm{d}\bar{\boldsymbol{q}}\,. \tag{2.110}$$

Of course, one has to be aware that τ depends on the position on the detector, i.e. on $\boldsymbol{q}$:

$$\bar{\omega}\tau = \bar{\boldsymbol{q}}\boldsymbol{r}_0\,. \tag{2.111}$$

Quantities tagged by a bar again represent the properties of the light in the center the light spectrum. It appears to be favorable to use a coordinate system aligned to the vector $\boldsymbol{r}_0$, where $\boldsymbol{e}_{\shortparallel}$ denotes the unit vector parallel to $\boldsymbol{r}_0$, and $\boldsymbol{e}_\perp$ denotes the perpendicular direction:

$$\bar{\boldsymbol{q}} = \bar{q}_{\shortparallel}\boldsymbol{e}_{\shortparallel} + \bar{q}_\perp\boldsymbol{e}_\perp\,, \quad \boldsymbol{r}' = r'_{\shortparallel}\boldsymbol{e}_{\shortparallel} + r'_\perp\boldsymbol{e}_\perp \quad \text{and} \quad \boldsymbol{r}_0 = r_0\boldsymbol{e}_{\shortparallel}\,, \tag{2.112}$$

which leads to:

$$h_{\mathrm{real}}(r'_{\shortparallel}, r'_\perp;\boldsymbol{r}_0) = \mu(\boldsymbol{r}_0)\iint_{-\infty}^{\infty}\gamma(\tau)\exp(\mathrm{i}(\bar{q}_{\shortparallel}r'_{\shortparallel} + \bar{q}_\perp r'_\perp))\,\mathrm{d}\bar{q}_{\shortparallel}\,\mathrm{d}\bar{q}_\perp\,. \tag{2.113}$$

As τ only depends on $\bar{q}_{\parallel}$ the integration over $\bar{q}_{\perp}$ trivially ends up in a δ-function $\delta(r'_{\perp})$. The integration over $\bar{q}_{\parallel}$ is changed to an integration over τ by using Eq. 2.111:

$$h_{\mathrm{real}}(r'_{\parallel}, r'_{\perp}; \boldsymbol{r}_0) = \mu(\boldsymbol{r}_0)\frac{\bar{\omega}}{r_0}\delta(r'_{\perp}) \iint_{-\infty}^{\infty} \gamma(\tau) \exp\left(\mathrm{i}\frac{r'_{\parallel}}{r_0}\bar{\omega}\tau\right) \mathrm{d}\tau\,. \tag{2.114}$$

Using the Wiener-Khintchine theorem (Eq. 2.98) readily gives:

$$h_{\mathrm{real}}(r'_{\parallel}, r'_{\perp}; \boldsymbol{r}_0) = \mu(\boldsymbol{r}_0)\,\frac{\bar{\omega}}{r_0}\,s\left(\frac{r'_{\parallel}}{r_0}\bar{\omega}\right)\delta(r'_{\perp})\,. \tag{2.115}$$

This result describes the FTH reconstruction of a δ-like object under partial coherence conditions. The spatial coherence is reflected by the factor $\mu(\boldsymbol{r}_0)$.[1] A reduction of the spatial coherence only reduces the contrast of the reconstruction, but is not acting on the resolution.

The influence of the temporal coherence in Eq. 2.115 on the reconstruction is much more severe, as it also affects the spatial resolution. Along the direction of the vector $\boldsymbol{r}_0$,

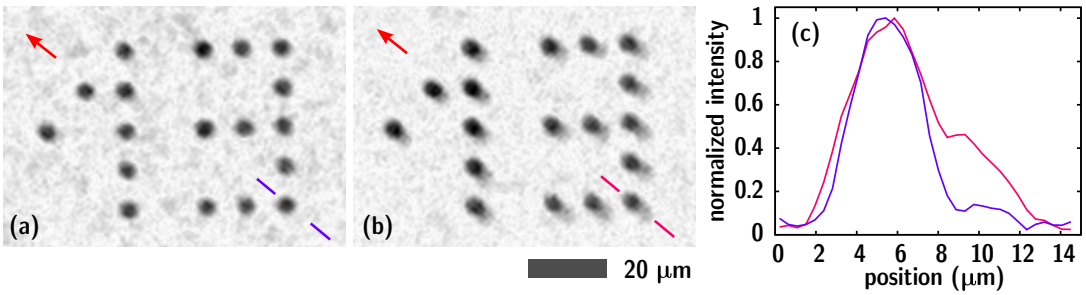

Figure 2.13: Influence of spectral broadening at an FEL source. The images in **(a)** and **(b)** were recorded using the same test object, but with different single pulses of the x-ray source. As the spectrum of the the pulses is varying from shot to shot also the image quality changes. Due to the broad spectrum of the radiation, the reconstruction is smeared out along the direction defined by the vector connecting object and reference aperture. The red arrows point in that direction. **(c)** Intensity slices through a single object dot for both reconstructions as indicated in panels (a) and (b). The data have been already published in [Pfa10a].

1 The factor $\bar{\omega}/r_0$ in Eq. 2.115 appears as a dimensional scaling factor. As the coherence factor $\gamma_{12}(\tau)$ can be interpreted as the fringe visibility in the hologram, it is dimensionless. Its Fourier transform (from reciprocal space to direct space) will thus need to have the dimension of 1/m. However, the spectral density $s(\omega)$ has the unit "per Hertz", i.e. seconds.

the reconstruction is modulated with the spectrum of the light $s(\omega)$.[1] When assuming a peak-like spectrum around the center frequency $\bar{\omega}$ with the width $\Delta\omega$, the object is still reconstructed at the position $r'_{\shortparallel} = r_0$ but the reconstruction is broadened by the factor $\Delta r' = \frac{\Delta\omega}{\omega} r_0$ [Pfa10a]. At a synchrotron beamline with a typical energy resolution $E/\Delta E = \omega/\Delta\omega$ better than 1000, the broadening is on the order of 1 nm to 5 nm for object–reference spacings below 10 µm. This situation changes when performing experiments at non-monochromatized beamlines at FEL sources with a spectral bandwidth of up to 1 %. In this case, the expected broadening of a few tens of nanometers is comparable to the resolution limits set by the reference aperture and the detector size.

Such an example is presented in Fig. 2.13 from experiments performed at the FEL FLASH in Hamburg [Pfa10a]. The figure shows two reconstructions of the same object—a test object consisting of the number "13" written in a dot matrix.[2] The images were recorded with different single pulses from the source. Due to the variation in the spectrum of the x-ray pulses [Ack07], the reconstructions differ from each other. The influence of the spectral width becomes visible by a one-dimensional broadening of the dots in the direction of the vector connecting reference and sample position. Note that this effect could be used for a single-shot compatible analysis of the wavelength spectrum of the source when the geometry of the sample is optimized for this purpose [Fle11].

2.8 Other effects influencing the point-spread function

There is, of course, a number of other effects that influence the PSF of the FTH imaging system. But when compared to the three contributions that have already been discussed in more detail, these effects have much lower impact, in particular in terms of spatial resolution.

2.8.1 Mechanical vibrations and drift

One of the major difficulties in *direct* high-resolution imaging methods is caused by mechanical instabilities of the setup components. On a nanometer scale, mechanical vibrations and drift due to, e.g., temperature fluctuations, can be prevented only by an enormous effort regarding the mechanical components such as the support structures and the stages. Nearly every displacement of the optics, the sample or the detector directly translates to a deterioration of the spatial resolution in the images.

At the same time, soft x-ray FTH imaging is particularly insensitive against such mechanical instabilities. The most sensitive parameter is the relative position between

1 For small objects compared to the object–reference distance, $\boldsymbol{r}_0$ can be treated as constant and the influence of the PSF is obtained by a convolution with the object as described in Sec. 2.4, since $s(r'_{\shortparallel}\bar{\omega}/r_0) = s(\bar{\omega}(r'_{\shortparallel} - r_0)/r_0 + \bar{\omega})$ and the PSF depends only on the relative distance $r'_{\shortparallel} - r_0$.

2 The sample foil was produced with the direct ultra-violet *Lithographie, Galvanoformung, Abformung* (LIGA) process.

the object and the reference which is absolutely fixed when choosing the sample design integrating object and optics mask on the same substrate. Movements of the whole sample arrangement only result in a reduction of the fringe visibility in the hologram. As this reduction takes place equally over the whole detector, i.e. independently on the momentum transfer, only the contrast of the reconstructed image is reduced as well, but the resolution is not affected. Therefore, vibrations or drift act very similarly as a reduced transversal coherence expressed by the coherence factor μ_{12} (Sec. 2.7.3). The contrast of the reconstructed image will only vanish completely, if the occurring position changes of the integrated sample become larger than the half fringe periodicity on the detector caused by the interference between object and reference wave. Commonly, this periodicity length corresponds to a few (4–10) detector pixels and each pixel has a size of 10 µm to 20 µm depending on the CCD model used. As a result, mechanical instabilities on a length scale three orders of magnitude larger than the spatial resolution can be easily tolerated in the FTH experiment.

2.8.2 Beamstop

The method of recording reciprocal-space information rather than a direct image has several advantages, such as redundancy, combined amplitude and phase information, a lensless setup, and drift insensibility, but there exists also a major drawback: The intensity differences, also called the *dynamic range*, in diffraction patterns are orders of magnitude higher than in a direct image. In many cases, the transmission function of an object is very smooth and the transmissivity differences rarely exceed a factor of 10. For object features exceeding the dynamic range limits of the imaging experiment, one tends to declare these feature as either being "opaque" or "empty". However, the scattered intensity I in the small-angle regime decays with the second to fourth power of the momentum transfer q, i.e. $I \sim 1/q^{2\ldots4}$ [Gla82], resulting in a dynamic range in the hologram that is typically on the order of 10^4 up to 10^6. When working with x-rays, the matter is further complicated by the fact, that the dynamic range of the CCD detectors is very limited in the x-ray range (10^2 to 10^3) as each x-ray photon creates a lot more electron–hole pairs than a photon in the visible spectrum.

There are two solutions to that problem which are usually applied simultaneously: First, the number of acquisitions of the hologram is increased and all acquisitions are summed up post-experimentally. Due to the finite readout time of the detector of typically a few seconds, more than 10^1 to 10^2 acquisitions are often impractical. Second, the most intense part of the hologram at low q is blanked out by a central beamstop. In principle, the missing information can be obtained in a separate measurement, but often it is omitted. In the latter case, the reconstruction is significantly affected by this filtering process. Due to the missing low q information, the image is high-pass filtered with respect to spatial frequencies. This kind of filter is well known from visible light microscopy producing the so-called dark-field image. A dark-field image is characterized by an artificial enhancement of edge features in the object. The resolution is barely influenced as the high-frequency

information is retained.

Mathematically, the beamstop impact is described by a filter acting as a multiplication mask to the hologram that either transmits or blocks the light. Using the convolution theorem of Eq. 2.41, the PSF of that filter is readily obtained by a Fourier transform of the mask. Due to irregularities in the shape and the sharp edges in the beamstop transmission function, the reconstruction is often deteriorated by fringes produced by the beamstop. It is therefore common practice to apply a numerical mask to the hologram data that is slightly larger than the actual beamstop and optimized to the data in way of hardly producing artifacts in the reconstruction [SN09]. In Fig. 2.14 such a mask with softened edges and the corresponding Fourier transform, that is the PSF, is shown by using parameters of a typical experimental scenario. The PSF is predominately characterized by a δ-function[1] with a hardly reduced magnitude of 0.998. The surrounding modulations are weaker by a factor of 10^{-3} and, hence, do not affect the spatial resolution.

1 In this case, the term δ-function is justified by the fact that the intensity is solely concentrated in the central pixel of the matrix used for the calculation. By increasing the size of the matrix via zero-padding, the physical extend of that pixel can be further reduced without any influence on the beamstop filter function.

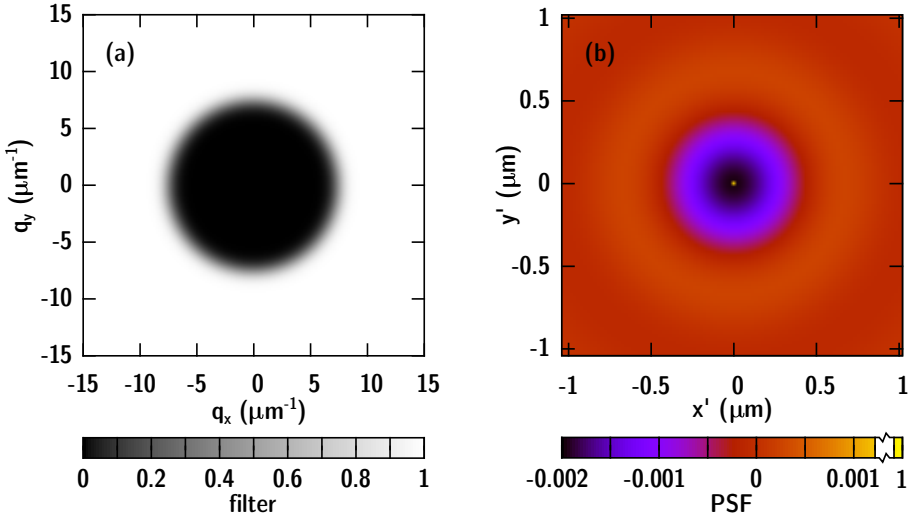

Figure 2.14: PSF of the beamstop mask. The calculations were made by using parameters of a typical soft x-ray FTH experiment. In this case, these parameters were taken from the experiment presented in the next chapter. A complete parameter list is found in Tab. 2.2. **(a)** The numerical mask as it is applied to the experimental hologram data. The figure displays the central part of the mask for better visibility. The whole hologram and the whole mask are ten times larger in each of both dimensions. **(b)** Calculated PSF (real part) by Fourier transforming the mask from (a). The intensity scale is linear, but has a gap since the intensity of the central peak and the surrounding background differs by three orders of magnitude. The intensity at $q = 0$ equals 0.998.

2.9 Summary

Since the invention of the integrated design combining optical mask and sample by Eisebitt et al. in 2004 [Eis04], FTH imaging found an ever increasing application in the field of x-ray imaging. On one hand, the method benefits from the common advantages in x-ray imaging such as high spatial resolution and high penetration depth, on the other hand, the design of the FTH experiment has some additional advantages over other x-ray imaging methods. In particular, the FTH integrated design is inherently very tolerant against drift and vibrations and the lensless setup allows for a flexible sample environment. As FTH is a coherent imaging method, the reconstruction of the image retrieves the complete exit wave field, i.e. amplitude and phase information. In the case of FTH, this reconstruction is an unambiguous process, obtained by a single Fourier transform.

A particularly broad application of the method is found in the field of imaging magnetic nano-structures. In this thesis, the image formation process for magnetic samples was thoroughly analyzed. As a result, a proposal for a new channel for detecting the magnetic contrast was made, which is called the *signed magnitude*. Compared to the commonly used real part of the reconstruction, this channel turns out to be more robust against

variation in the photon energy and illumination function. It was shown that the signed magnitude is proportional to the component of the magnetization being parallel to the x-ray-beam propagation axis.

The main part of this chapter was dedicated to the imaging properties of FTH, i.e. to the PSF of the imaging system as this question has not been treated in literature for the case of soft x-ray FTH so far. Three main contributions influencing the PSF were identified: (i) the structure of the reference object, (ii) the properties of the area detector, and (iii) the coherence properties of the x-ray illumination. In the following the effects of these contributions will be summarized and compared.

In the previous sections each component was investigated independently from the other two contributions. When reviewing the results of these investigations given in Eq. 2.40, Eq. 2.77, and Eq. 2.115 and summarized in Tab. 2.1, one realizes the following similarities:

1. Each of the PSFs independently predicts the position of the image in the reconstruction matrix determined by the reference–object separation vector $\boldsymbol{r}_0$.

2. All three PSFs depend on the position of the object $\boldsymbol{r}_0$ or on the position in the reconstruction matrix $\boldsymbol{r}'$ and not only on the relative distances $(\boldsymbol{r}' - \boldsymbol{r}_0)$ with the result that the imaging system is not space invariant in general. However, in the case of a small object extent compared to the distance $\boldsymbol{r}_0$, the dependence on $\boldsymbol{r}_0$ and $\boldsymbol{r}'$ is weak and the system can be treated as space invariant with the possibility of finding the image via a convolution of the object with the PSF.

3. In the context with the previous point, it becomes apparent that the PSFs can be separated into two different parts. First, there is always a term that is smoothly depending on $\boldsymbol{r}_0$ or $\boldsymbol{r}'$ and therefore affecting the contrast of the reconstruction. The second term is always a localized broadening of the delta peak object which is therefore acting on the spatial resolution. In Tab. 2.1, these two parts are separately listed for each PSF component.

	contrast	**resolution**
reference	$\lvert b(x_0, y_0)\rvert \exp(-\mathrm{i}\beta(x_0, y_0))$	$\rho^*(-x - x_0, -y - y_0))$
detector	$f_x f_y \operatorname{sinc}(\frac{f_x}{2\pi}\,\Delta q_x\, x', \frac{f_y}{2\pi}\,\Delta q_y\, y')$	$\operatorname{sinc}(\frac{N}{2\pi}\,\Delta q_x\,(x' - x_0), \frac{M}{2\pi}\,\Delta q_y\,(y' - y_0))$
coherence	$\mu(x_0, y_0)$	$\frac{\bar{\omega}}{r_0}\, s\left(\frac{r'_{\shortparallel}}{r_0}\bar{\omega}\right) \delta(r'_{\perp})$

Table 2.1: Overview over the PSFs derived for the influence of the reference, the pixelated area detector and the coherence properties of the x-rays. The PSFs are split into a part influencing the contrast of the image and a part mainly affecting the spatial resolution.

object aperture		1.5 µm
object diameter		100 nm
reference diameter		60 nm
object–reference spacing	r_0	8 µm along the x-direction
beamline focus–sample distance	F	35 cm
x-ray wavelength	λ	1.59 nm
energy resolution (FWHM)	$E/\Delta E$	1625 (synchrotron), 200 (FEL)
spatial coherence (FWHM) (horz. × vert.)	μ	15 µm × 30 µm
beam divergence (FWHM) (horz. × vert.)		6 mrad × 1 mrad
sample–CCD distance	D	35 cm
number of pixels of CCD	$N \times M$	2048 × 2048
pixel size of CCD	$\Delta\xi \times \Delta\eta$	13.5 µm × 13.5 µm
fill factor of CCD	$f_x \times f_y$	1 × 1

Table 2.2: Parameters of the model FTH experiment used for the calculations.

Having said all that, one question for the reader may remain: Which implications will these considerations have for the actual x-ray holography experiment? This question already refers to the next chapter where FTH is applied in a study of magnetic nanostructures. It is, thus, natural to use the experimental parameters of this study as an example to illustrate the actual impact of the PSFs on an x-ray imaging experiment. The impact of the different contributions will be simulated in the following. All parameters used in this illustration simulation are listed in Tab. 2.2. The defined object diameter of 100 nm shall correspond to the typical size of magnetic nanostructures in order to show the influence of the PSF on these structures such as magnetic domains or magnetic islands. The spatial coherence properties of the beamline are unknown and the values given in the table have to be considered as conservative estimates. In addition to the energy resolution of the synchrotron beamline, the energy resolution of a non-monochromatized and non-seeded FEL beam is also considered [Ack07] as it turns out that the influence of energy spread of the x-rays pulses is much more severe at FEL sources.

In Fig. 2.15 the results for the contrast terms from Tab. 2.1 are presented. The phase and the intensity of the illumination function reflected by the factor b are calculated assuming a spherical wave emerging from a point-like focus, with the given divergence while the actual extent of the focus was neglected. It turns out, that the phase variation—even at distances from the focus on the order of tens of centimeters—is still considerable, but the intensity variation stays below 0.1 % and can be neglected. However, the $\overline{\text{MTF}}$ of the CCD chip and the spatial coherence already have an appreciable influence on the reconstruction contrast. Although the contrast is still high (in both cases more than 80 %) at the position of the image in the matrix, it drastically reduces towards the edges of the reconstruction field, i.e. for larger $\boldsymbol{r}_0$.

Figure 2.16 summarizes the impact of the PSFs on the spatial resolution. For visualization, a model object being a sphere with 100 nm diameter is investigated by calculating its

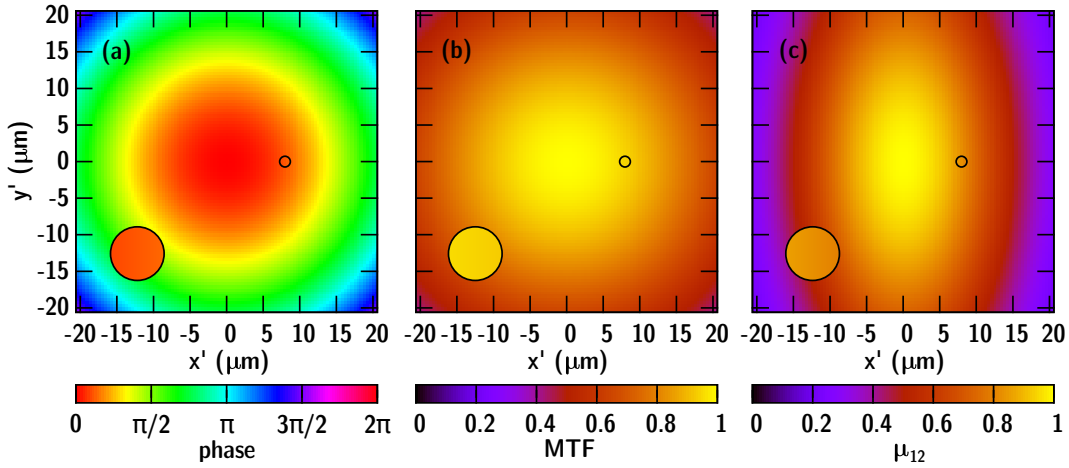

Figure 2.15: Visualization of the contrast terms of the PSFs given in Tab. 2.1 using the experimental parameters from Tab. 2.2. The figures show the whole reconstruction matrix and the black circle marks the position and size of the reconstructed real image defined by the object aperture with 1.5 µm diameter. The circle in the bottom-left edge of each panel is a five-fold magnification of that area, that additionally illustrates the variation of the contrast within the object area. This variation is nearly indistinguishable in all cases. **(a)** The phase variation in the illumination due to focusing of the light when assuming a spherical wave. The intensity variations (not shown) corresponding to the given beam divergence are small (below 0.1 %). **(b)** Influence from the pixelated detector. **(c)** Influence from the light's spatial coherence properties.

convolution with the reference, the Fourier-transformed detector window, and with the scaled energy spread. The reference is also modeled by a circle of 50 nm diameter. The square detector window results in a sinc-like convolution kernel. The spectrum of the light is assumed to be Gaussian and the calculations are performed with a spectral width corresponding to a synchrotron beamline, as well as to an FEL beamline. In the modeled experimental geometry, the influence of the reference and the CCD are similar with a broadening (10 %–90 %) of the imaged object edges of $d_{\mathrm{ref}} = 42\,\mathrm{nm}$ and $d_{\mathrm{CCD}} = 21\,\mathrm{nm}$, respectively. At a synchrotron beamline the smearing of the edges in the images due to the photon energy spread can be neglected ($d_{\mathrm{spec}} = 5\,\mathrm{nm}$), but it becomes considerably large when using FEL pulses (41 nm). The expected resolution for the FTH experiment in the next chapter is estimated by $(d_{\mathrm{ref}}^2 + d_{\mathrm{CCD}}^2 + d_{\mathrm{spec}}^2)^{0.5} = 47\,\mathrm{nm}$ which fits well to the images presented in that chapter. As already depicted in Fig. 2.13, the influence of the spectral broadening at FEL sources based on self-amplified spontaneous emission cannot be neglected anymore [Pfa10a]. Moreover, the spectrum, i.e. the peak position, the width and the number of modes, is fluctuating from pulse to pulse [Ack07] with the result that the image obtained from the same object changes with the pulse properties. The solution for this problem is either to additionally monochromatize the pulses at the expense of

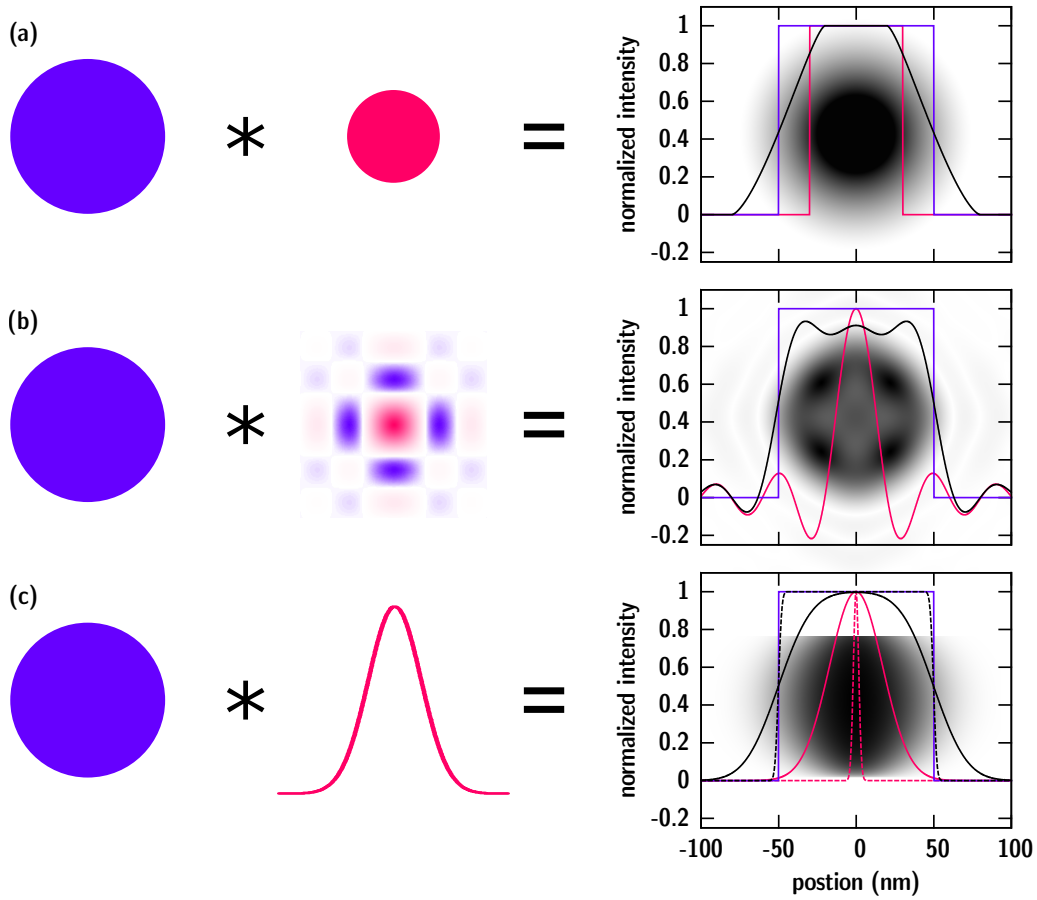

Figure 2.16: Impact of the PSFs on the resolution. The calculations were made using the equations given in Tab. 2.1 and the experimental parameters listed in Tab. 2.2. The first column shows the test object, a sphere (100 nm diameter) with unity in the real part and zeros in the imaginary part. The second column is a representation of the PSF the object was convolved with. The last column shows the result of the convolution as a x'–y'-map (magnitude) in the background and a slice (real part) along the x'-direction at $y' = 0$ in the line plot (black line). The blue line is a slice through the object (real part) and the red line is a slice through the PSF (real part). The three rows illustrate the influence from **(a)** the size of the reference aperture, **(b)** the size of the area detector, and **(c)** the spectral width of the radiation. The solid lines in (c) show the FEL case, the dashed lines show the situation at a monochromatized synchrotron beamline.

loosing photons and temporal resolution or by repeating the experiment several times and using a "lucky shot" consisting of only one narrow spectral mode. For the future, it is highly desirable to operate these FEL sources in a seeded mode, where the spectrum of the emitted light is supposed to be much more narrow [Ama12].

With a very practical point of view on the investigated PSFs, it turns out that the precise experimental origins limiting the achievable spatial resolution in FTH are very easily identified. Consequentially, it should by straight forward to further improve the resolution commonly achieved in FTH experiments. As already pointed out, the photon energy resolution ($E/\Delta E$) at synchrotron beamlines is on the order of several thousands and does not limit the FTH resolution. As the influence of the detector system on the resolution is simply given by the maximum detected scattering angle, a higher resolution is achieved by using a larger detector having more pixels or by moving the existing detector closer to the sample. In the latter case, this will compromise the available FOV.

The most severe limitation is set by the size of the reference structure. First of all, one has to able to produce nanometer-sized apertures with high aspect ratio. As outlined in Sec. 3.2.1, focused ion beam (FIB) devices are capable to produce apertures with sub-100 nm diameter and with an aspect ratio of more than 10. Anticipating a continuation of the tremendous development of these devices, structure sizes on the order of 10 nm with even higher aspect ratios will become realizable. On the other hand, one has to be aware that the photon transmission through a simple aperture decreases with the square of its diameter while the achievable resolution scales linearly with the size. As a result, it will become impossible to detect the necessary amount of photons in order to obtain a reconstruction with an adequate signal to noise ratio for ever decreasing reference sizes. There are two options for pushing the limit to smaller reference structure sizes and, thus, smaller resolution lengths: first, by increasing the available photon flux, and second, by using more sophisticated reference structures.

The evolution of synchrotron sources and beamlines is a still ongoing process. In the last years, new synchrotrons have been opened and more sources are going to be built. At the same time, existing beamlines are improved with newly developed optics. As coherent imaging methods become more and more fashioned, the number of beamlines specialized in delivering a high photon flux with high degree of coherence is also increasing. Undoubtedly, the evolution in the x-ray sources will have a huge impact on the FTH imaging perspectives.

On the reference side, three approaches for improving the photon efficiency of the reference aperture have been proposed in the last years. The idea behind all of these approaches is to find a structure that mathematically can be transformed into a point-like object that then creates the image reconstruction similar to the standard FTH method. The first approach was to employ uniformly redundant array (URA) arrangements of small identical apertures [Mar08]. The convolution of an URA arrangement with a so-called decoding pattern reduces to a single aperture. Consequentially, the image is reconstructed by first taking the Fourier transform of the hologram and then convolving with the decoding pattern. The second approach is called holography with extended reference by autocorrelation linear differential operation (HERALDO) [GS07; Zhu10]. The method

exploits the fact that the derivative of a slit-like transmission function reduces to points at each end of the slit. The last approach is built on using Fresnel zone plates as reference structure [Gei13]. As the zone plate produces a focal spot upstream of the sample, one has to numerically propagate the reconstruction from the focal point back to the sample plane in order to achieve a sharp image. The drawback of these methods is the additional mathematical step that has to be taken in order to obtain the final reconstruction. This step complicates the reconstruction process and may also introduce artifacts. Hence, a precise understanding of these operation is necessary and has to be developed in the future. However, the goal of realizing a spatial resolution of 10 nm or better will most likely only be achieved by applying one of these methods to FTH imaging.

3 Switching field distribution of bit-patterned media

3.1 Introduction

In a recent study [Hil11] information scientists have tried to quantify what is popularly but also scientifically [Cas00] referred to as: *the age of information*. The study makes an estimate about the world's total technological capacity of stored information with the inconceivable result of 2.9×10^{20} (optimally compressed) bytes (290 millions of terabytes!) in the year 2007. The annual growth rate over the last twenty years was 23 % corresponding to an information doubling every three and a half year. By monitoring the use of different storage technologies, the study also reveals another revolution: the crossover from analog to digital storage. Whereas in 1987 the usage of digital technologies was negligible, in 2007 94 % of all information was stored digitally.

Magnetic recording technologies which had in both the analog and the digital world a dominant position also reflect the digital revolution. Twenty years ago the lion share of information was stored on video and audio tapes, today hard disks and digital tapes dominate data storage. Although other digital storage technologies are emerging, still more than 50 % of the world's total information is stored on hard disk drives resulting in a strong demand for increasing device capacities in order to keep in step with an exponential information quantity growth.

The capacity of hard disk drives is also exponentially increasing. As an example, Figure 3.1 shows the evolution of the largest commercially available capacity of a 3.5 in hard disk drive. In the last 25 years, the capacity has grown over five orders of magnitude with an annual rate of 65 % until the year 2001 and 35 % in the last ten years. This growth involves a dramatic increase in the storage density, that is commonly measured in bits per square inch (bits/in^2). Today, commercial hard disks have densities of up to 446 Gbits/in^2 [HGS12a] while even higher densities have already been reported for demonstration systems [Alb09]. In such high-density media, a single bit takes an area of below 40 nm $\times$ 40 nm.

In conventional perpendicular continuous granular media (CGM), a bit, i.e. an information quantum, is stored in the magnetization of a number of (nearly uncoupled) magnetic grains in a certain area of a magnetic thin-film [Ric07]. The term perpendicular refers to the perpendicular magnetic anisotropy of the film leading to a magnetization pointing either up or down in the out-of-plane direction. The number of grains defining a single bit is determined by the signal-to-noise ratio (SNR) sufficient for an accurate read process. Technologically, the size of a single bit is, thus, reduced by down-scaling the grain size. The limit for the thermal long-term stability (at a temperature T) of a small grain (with

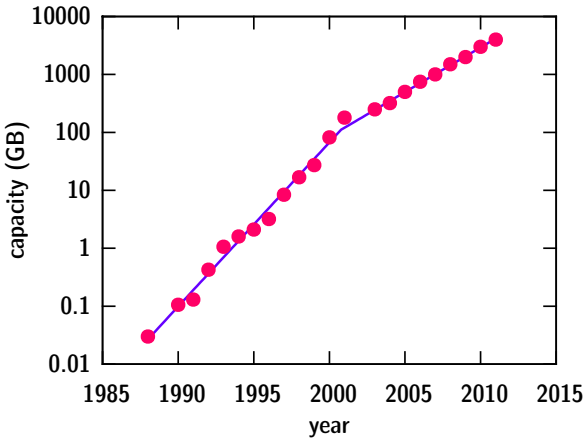

Figure 3.1: Evolution of the maximum capacity of commercially available hard disk drives with the popular form factor 3.5 in [Wik12].

a volume V) is defined by the superparamagnetism phenomenon [Bea59]. The lifetime (τ_N) of the magnetic state, i.e. the time between two magnetization flips, is given by the Néel-Arrhenius equation [Sha94]:

$$\tau = \tau_0 \exp\left(\frac{KV}{k_\mathrm{B}T}\right) , \tag{3.1}$$

with an attempt time $\tau_0 \approx 10^{-9}\,\mathrm{s}$, K being the magnetic anisotropy and k_B the Boltzmann factor. The demand for a data stability of at least 10 years leads an established criterion of $KV/k_\mathrm{B}T > 60$ [Wel99]. In order to maintain the thermal long-term stability of the grains, the magnetic anisotropy has to be increased for a decreasing grain size.

At the end of this evolution, the minimum bit size—corresponding to the maximum recording density—will be limited by the maximum achievable magnetic field of the write head that is necessary to magnetically reverse grains with the required anisotropy maintaining thermal stability. In addition, a shrinking write head accounting for the smaller bit size may even lead to smaller achievable write fields. The result of all these conflicting requirements is also referred to as the *trilemma of magnetic recording* [Ric07]: High recording density requires small grains, thermal stability requires large grain volumes and high anisotropy, and writability requires low anisotropy.

There are two proposed approaches in order to overcome this limitation [Shi09] and ultimately it is very likely that both approaches have to be combined [Eva12]. The first technology relies on reducing the energy barrier for switching a magnetic grain by local heating or by adding a radio frequency magnetic field. The methods are called heat-assisted magnetic recording (HAMR) and microwave-assisted magnetic recording (MAMR), respectively. Using the HAMR method, a recording density of more than $1\,\mathrm{Tbits/in^2}$ was demonstrated recently [HGS12b]. It was discussed, that the HAMR technology extends the trilemma to a quadrilemma of magnetic recording as now the bit error rate during thermal writing of the bits has to be considered [Eva12]. A low error rate requires high

saturation magnetization values and high switching fields from the write head.

While HAMR basically implies a drastic modification of the write head, the second proposed technology, on the other hand, will use similar heads as today, but with completely different recording media. These so-called bit-patterned media (BPM) use lithographically patterned media in a way that each information bit is stored in an isolated magnetic switching volume, which is consequentially referred to as a magnetic island. Each island consists of one grain or a few strongly coupled grains with the result that the magnetic energy KV is determined by the whole island volume. Since this volume is larger than the grain volume in CGM, the magnetic anisotropy can be reduced and the bits can be still accessed by the conventional write heads.

In order to realize bit-patterned recording with recording densities of 1 Tbits/in^2 and beyond, several technological challenges have to be met. The most striking ones are [Alb09]: a very tight switching-field distribution (SFD) of the islands, very low spatial patterning tolerances, and a very accurate write synchronization. The BPM study which was performed in the framework of this thesis focuses on the first issue, the islands' SFD. The SFD describes the bit-to-bit variation of the coercive fields. In order to reliably perform a writing process without influencing neighboring islands, the SFD of the media has to be sufficiently narrow. In general, the SFD is determined by two different contributions [Hel07a]. First, the magnetic islands are influenced by the stray fields of neighboring islands. In case of perpendicular anisotropy systems, the stray fields from neighbors tend to broaden the SFD. Second, the switching field of every single island is influenced by its individual properties. Due to island-to-island variations of these properties, the switching fields show a so-called intrinsic distribution. Variations in the island reversal fields are assumed to be induced by variations of the magnitude or direction of the local anisotropy, such as originating from island size, shape, composition, and (crystalline) structure, as well as localized strain, corrupted island edges, or misaligned grains [Dit05; Hu05b; Lau08; Sha10; Tho06].

In this study, a BPM model system is investigated concerning both the inter-island interaction and the intrinsic island properties leading to a broadening of the SFD. The study involved the monitoring of the magnetic switching of individual islands in a certain field of view of a patterned area using the x-ray Fourier-transform holography (FTH) imaging method and a subsequent structure analysis of the islands via transmission electron microscopy (TEM) and electron diffraction.

In particular in the case of BPM samples, direct imaging methods as FTH [Gü10; Pfa11], but also magnetic force microscopy (MFM), e.g. Refs. [Lau08; Sha10; Tho06], may in principle provide valuable information beyond ensemble average methods, e.g. Refs. [Dit05; Hel07a; Hu05b], as the properties of individual islands can be investigated and analyzed. In the present study, the imaging approach was at least helpful if not necessary for (i) disentangling contributions from the magnetic islands and the surrounding material, (ii) investigating the switching probability of individual islands, and (iii) to identify islands with particular low or high switching field.

Compared to MFM imaging, FTH experiments have some advantages that, where appro-

priate, justify the much higher effort of the method. In this work, these advantages include (i) the possibility to image the sample under an externally applied magnetic field, (ii) the possibility to image and investigate several different samples simultaneously, and (iii) the exclusion of any influence of the measurement on the magnetic state of the island, as it may be induced by the magnetized MFM tip. With respect to future applications, x-ray FTH imaging is able (iv) to provide element contrast and (v) to image buried layers which for example may become important for surveys of exchange coupled composite (ECC) BPM structures [Hau09]. Additionally, x-ray imaging methods (vi) have the potential to provide a spatial resolution on the order of 10 nm [Zhu10], and (vii) bring the opportunity for dynamic, i.e. time-resolved, measurements with picosecond time resolution [Bü13a].

As the study presented in this chapter is one of the first of this kind of FTH measurements at BPM samples, it must be clearly considered as a pilot study. The experimental procedures will be explained in detail in Secs. 3.2 and 3.3. In Secs. 3.4 to 3.6, different ways are proposed of how the vast amount of information in the image datasets can be analyzed. In the analysis information is gained on the intrinsic properties of the island ensemble, the magnetostatic interactions present in the sample and on the stochastic switching processes taking place. The structural origin of the intrinsic variation of the switching field is investigated in Sec. 3.7 with the help of a TEM analysis.

3.2 Experimental details

The study was performed in cooperation with scientists from Hitachi Global Storage Technologies (HGST) and different stages of the study have been performed in different groups at different places. The sample was prepared and pre-characterized in the Hitachi laboratories and then further processed at the SLAC National Accelerator Laboratory in California, USA. The FTH imaging with magnetic contrast was performed at the BESSY II synchrotron source in Berlin. Afterwards, the TEM analysis was again conducted by the electron microscopy group of the Hitachi research center. Of course, in the following, the results of all experimental steps will be summarized, but with the focus on the FTH imaging and the analysis of the data.

3.2.1 General sample layout for Fourier-transform holography using soft x-rays

As already described in the previous chapter (2.1), the FTH method in its soft x-ray compatible variant takes huge advantage from the integrated sample design first realized by Eisebitt et al. [Eis04]. By preparing the optics mask and the sample on opposite sides of the same x-ray transparent substrate, any drift or vibration between optics and sample is avoided. Due to the placement of the reference wave origin in the sample plane with a slight transversal offset from the sample, the twin image problem is effectively circumvented.

Commonly, the integrated sample is prepared on a silicon nitride (Si_3N_4) membrane with a thickness of 50 nm to 200 nm. The membrane is supported by a silicon frame and has a

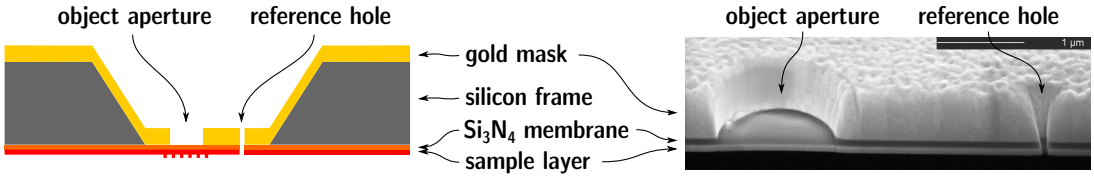

Figure 3.2: Sketch **(left)** and SEM slice image **(right)** of the integrated sample design commonly used in soft x-ray FTH (reproduced from [Sch07b]).

lateral window size of usually 0.1 mm to 1 mm. The commercially available membranes are fabricated by first growing a Si_3N_4 film on a (1 0 0) oriented Si waver using chemical vapor deposition and subsequent anisotropic etching of the lithographically defined window into the silicon substrate. In most cases, the resulting flat Si_3N_4 surface on one side of the membrane is used for the sample preparation while on the opposite site of the membrane surrounded by the remaining (1 1 1) silicon facets, the optics mask is produced.

The optics mask is processed into a gold film by focused ion beam (FIB) lithography. The gold layer has a thickness of around 1 µm making the layer nearly opaque to soft x-rays with photon energies below 900 eV (transmission below 10^{-6}). The Au film can be deposited via evaporation, sputtering or electroplating of gold. In the simplest FTH geometry, an object aperture defining the field of view (FOV) with a diameter of 1 µm to 2 µm and a reference pinhole with a diameter below 100 nm are fabricated into the gold film (Fig. 3.2). While the reference hole is milled completely through the whole structure in order to maximize the x-ray transmission, the substrate membrane in the object aperture stays intact giving the opportunity to prepare the sample on the opposite side of the membrane. The minimum distance between the two holes is given by 1.5 times the object aperture diameter, but a larger distance is used to promote a clear separation of the images in the reconstruction. A maximum limit of the distance is set by the transversal coherence length of the illumination.

3.2.2 Layout of bit-patterned media prototype sample

For the BPM holography sample in the present study, a 150 nm thick Si_3N_4 substrate containing four different patterned areas was used (Fig. 3.3). Each patterned area has a size of 6 µm × 6 µm and consists of cuboidal pillars arranged in a square lattice with different lattice constants (pitch). The pillars have a lateral size of 80 nm × 80 nm, a height of 40 nm and have been produced by electron-beam lithography using polymethyl methacrylate resist and a 20 nm thick CrMo alloy etch mask. On top of the patterned substrate, the magnetic multilayer system is sputter deposited. The multilayer consists of (Fig. 3.4): first, a 15 Å thick Ta adhesion layer followed by a 30 Å thick Pd seed layer. Then, 24 repetitions of a Co/Pd bilayer with 5.5 Å Co thickness and 8 Å Pd thickness are deposited which are finally capped by 12 Å Pd in order to prevent oxidation of the cobalt. The total thickness of the multilayer stack is 38 nm. The leading perpendicular anisotropy

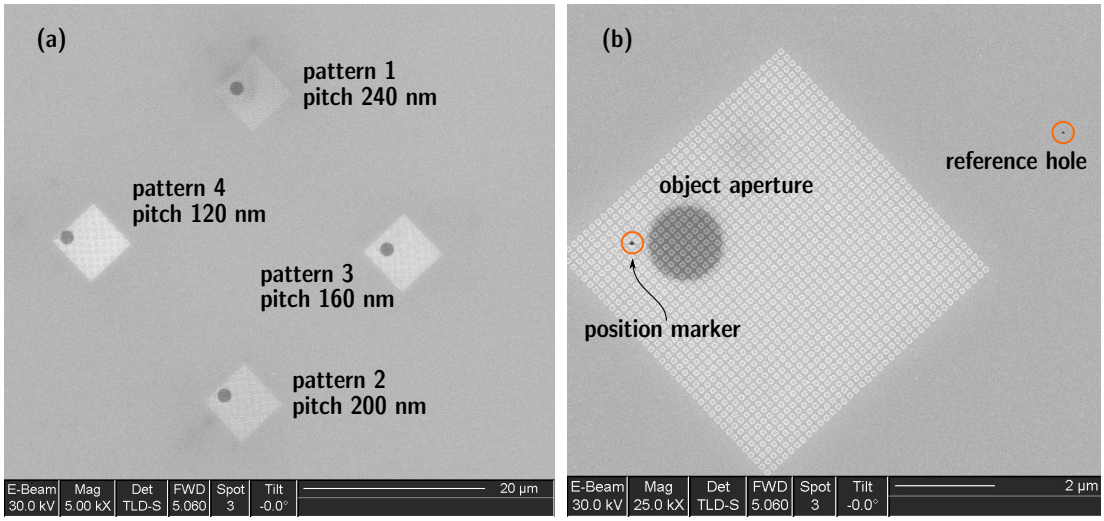

Figure 3.3: **(a)** SEM overview image of the whole BPM sample containing four different patterned areas that are independently imaged. **(b)** FTH arrangement for patterned area 3. The image is taken from the magnetic layer side, but one can clearly see the object aperture shining through the substrate. The position marker and the reference hole are milled completely through all layers.

term in Co/Pd multilayers originates from the Co/Pd interfaces [Sto06]. Furthermore the Ta/Pd seed layers provide an out-of-plane FCC [1 1 1] preferred grain crystal orientation in the Pd-rich multilayer with an x-ray rocking curve full width at half maximum (FWHM) of 7°–8°. The [1 1 1] orientation creates an additional second source of perpendicular anisotropy [Eng91] resulting in a higher anisotropy observed for [1 1 1] oriented grains compared to misaligned grains.

In the patterned areas of the substrate, the material is deposited onto the pillar structures as well as in the trenches between the pillars (Fig. 3.4). On top of the pillars, magnetic islands are created which are exchange decoupled from neighboring islands and from the trench material. The trench material forms a continuous magnetic network around the islands and merges with the continuous film outside the patterned areas. Transmission electron micrographs showing slices through similar patterned structures can be found in Refs. [Hel08; Hel09]. The small amount of material that is deposited at the walls of the pillars does not promote any exchange interaction between the islands and the trenches as it grows very irregularly.

For each of the four patterned areas, an object hole and a reference hole is fabricated into the gold film deposited on the opposite side of the membrane (Fig. 3.3). The FOV is 1.5 µm in diameter and the references have a diameter of 60 nm to 80 nm. Each object–reference pair forms an independent FTH arrangement and all four samples can be imaged simultaneously (Sec. 2.3). Therefore the distance between the object and the reference hole was chosen equally (8 µm) for all objects, but the position of the reference hole with

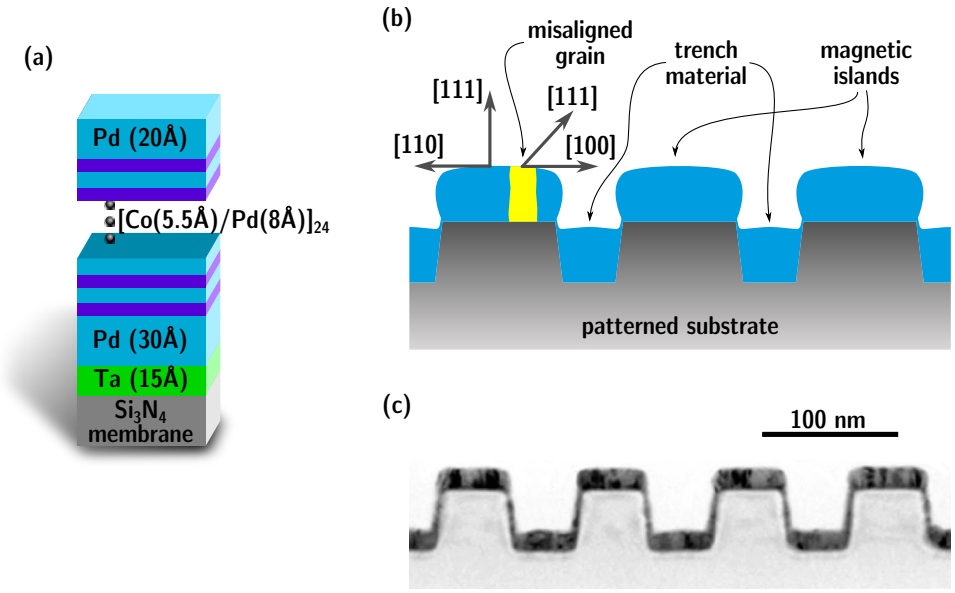

Figure 3.4: **(a)** Illustration of the magnetic multilayer system where the thickness of the layers is shown to scale, except for the Si_3N_4 substrate which is about four times thicker than the whole multilayer. **(b)** Sketched slice through the patterned area. On the pre-patterned substrate (grey), the magnetic material (blue) is deposited forming islands on top of the pillars. The material in the trenches remains magnetically active. The seed layers provide an out-of-plane FCC [1 1 1] preferred grain crystal orientation resulting in in-plane [1 1 0] oriented grains. The [1 1 1] direction for grains with in-plane [1 0 0] vectors—later called misaligned grains—is geometrically tilted away from the out-of-plane direction. **(c)** TEM image of a slice through a different BPM sample. The sample layout is very similar to the sample used in this study except for the total thickness of the multilayer which was much smaller in this case. The image was taken from [Hel08].

respect to the object aperture was varied in steps of 36° in order to avoid any overlap of the images in the reconstruction. The maximum distance between two object holes does not exceed 35 µm.

While the shape and the size of the islands were kept constant for all four patterned areas, the pitch p was varied in a range from 120 nm to 240 nm (Fig. 3.5). The shape of the islands is assumed as a rectangular prism of size $2a \times 2b \times 2c$ using the design dimensions of $2a = 2b = 80$ nm and $2c = 32.4$ nm. The storage density ($1\,\text{bit}/p^2$) and the fill factor ($f = 4ab/p^2$)—giving the fraction of sample area used for storing information to unused area—both inversely quadratically depend on the pitch length. The maximum density (fill factor) reached for the 120 nm pitch area is 44.8 Gbits/in^2 (44.4 %).

The described sample design must clearly be considered as a magnetic model system with respect to magnetic data storage. The design was optimized to the FTH imaging technique rather than to application aspects. In particular, the magnetic film contains

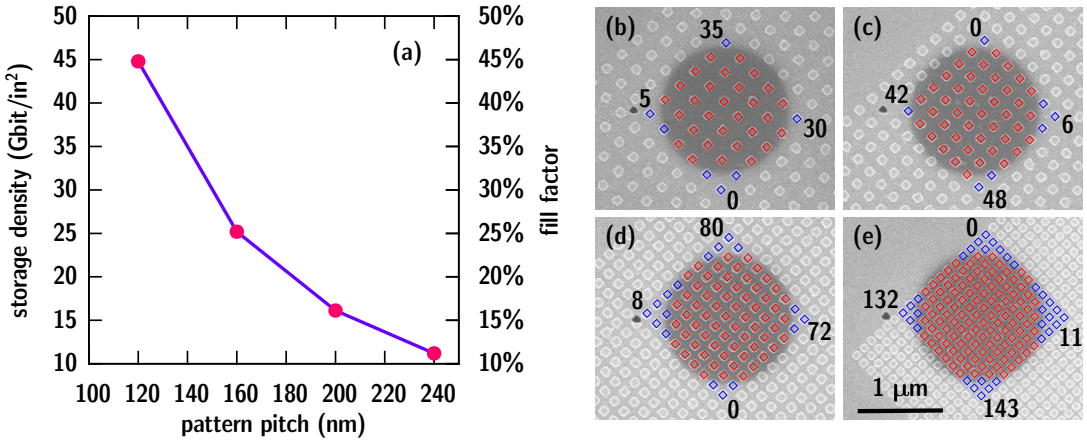

Figure 3.5: **(a)** Storage densities and fill factors of the four patterned areas on the sample. **(b)**–**(e)** SEM images of the patterned areas with **(b)** 240 nm, **(c)** 200 nm, **(d)** 160 nm, and **(e)** 120 nm pitch. The dark shadow marks the object aperture which is fabricated into the gold film on the opposite side of the membrane. Next to the FOV a position marker hole was milled. The SEM images are overlaid with a grid defining the numbering scheme of the islands.

a high fraction of cobalt since the measurements are performed resonantly at the cobalt L_3 absorption edge. In addition, the layer composition has been chosen such that it is possible to saturate the sample with the electromagnet available in the experimental vacuum chamber (see Sec. 3.2.4). Finally, the dimensions of the pre-patterned substrate have to be resolved in the FTH image reconstructions, i.e. the islands must be large enough to exhibit sufficient magnetic contrast and the trenches must be wider than the spatial resolution limit. These conditions result in a bit density which is a least one order of magnitude smaller than in production prototype pattern.

3.2.3 Magnetic properties

A continuous multilayer film prepared on a sister sample was magnetically characterized using a vibrating-sample magnetometer (VSM) in the HGST laboratories. The in-plane and out-of-plane hysteresis loops are shown in Fig. 3.6. The difference in the saturation fields clearly demonstrates the perpendicular magnetic anisotropy of the film. The measurement yielded a saturation magnetization (M_s) of (690 ± 10) emu cm^{-3} normalized to the full $[Co/Pd]_{24}$ multilayer stack with a height of 32.4 nm. The maximum effective anisotropy field, that is the in-plane saturation field, ($H_{k,eff}^{max}$) is (15.0 ± 0.2) kOe, the average effective anisotropy field ($H_{k,eff}^{avg}$) defined as the applied field where $0.9M_s$ is reached is (11.0 ± 0.2) kOe. In order to calculate the uniaxial anisotropy (K_u) of the film, one also has to account for the demagnetizing field acting against the anisotropy field inside the sample. The demagnetizing field (H_{demag}) is given by $4\pi M_s$ for a uniformly magnetized

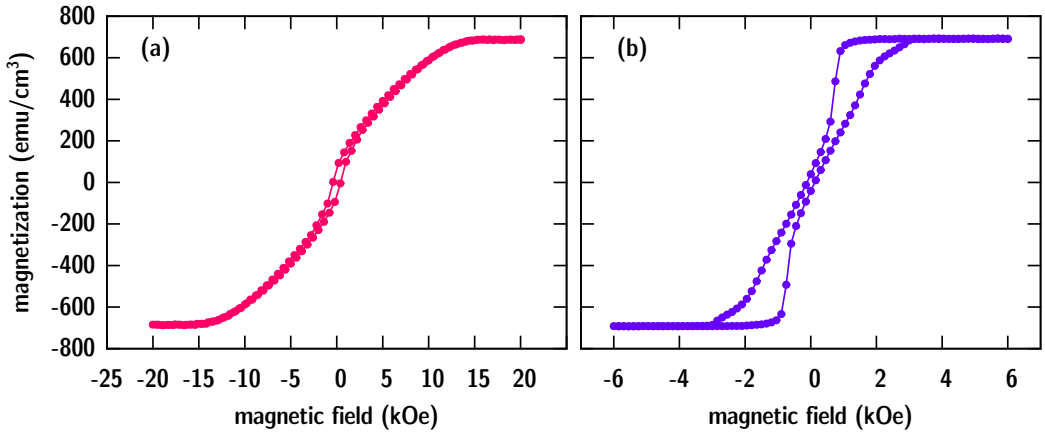

Figure 3.6: Characterization of the magnetic film using VSM. **(a)** In-plane hysteresis loop and **(b)** out-of-plane hysteresis. The magnetization was normalized to the full width of the magnetic multilayer (32.4 nm).

film. Since the magnetic film decays into domains in the remanent state, the associated magnetic energy cannot be easily calculated. In Ref. [Bü13a] the following method to determine K_u using the in-plane and out-of-plane hysteresis loops is proposed.

The calculation uses the saturation energy which is obtained by integrating the equilibrium magnetization curve that describes the path along the minimum free-energy:

$$E_\mathrm{s} = \int_0^{M_\mathrm{s}} H \mathrm{d}M \,. \tag{3.2}$$

As an approximation for the equilibrium magnetization curve, the average of both hysteresis branches can be used with the difference of both branches giving an estimate for the confidence interval of the result. The saturation energy constitutes the difference of the free-energy density in the saturated (F_s) and in the remanent (F_0) state of the system. That is, separately for the in-plane (ip) and for the out-of-plane (oop) loop:

$$E_\mathrm{s,ip} = F_\mathrm{s,ip} - F_0 \tag{3.3}$$

$$E_\mathrm{s,oop} = F_\mathrm{s,oop} - F_0 \,. \tag{3.4}$$

It is assumed that the value of F_0 is unique, i.e. independent on the actual domain configuration and equal for the in-plane and the out-of-plane loop. Additionally, the free-energy density is normalized such that $F_\mathrm{s,ip} = 0$. The free-energy density in the out-of-plane saturated state is then calculated from the competing energy of demagnetizing

field and the uniaxial anisotropy: $F_{\mathrm{s,oop}} = 2\pi M_{\mathrm{s}}^2 - K_{\mathrm{u}}$. Thus, K_{u} is calculated as:

$$K_{\mathrm{u}} = E_{\mathrm{s,ip}} + 2\pi M_{\mathrm{s}}^2 - E_{\mathrm{s,oop}}\,. \tag{3.5}$$

Note, that, when approximating the integral for $E_{\mathrm{s,ip}}$ (Eq. 3.2) with a triangular area as $H_{\mathrm{k,eff}}^{\mathrm{avg}} M_{\mathrm{s}}/2$, one ends up with the classical way of calculating K_{u} for a film showing full remanence, but now corrected by $-E_{\mathrm{s,oop}}$:

$$K_{\mathrm{u}} = \frac{H_{\mathrm{k,eff}}^{\mathrm{avg}} M_{\mathrm{s}}}{2} + 2\pi M_{\mathrm{s}}^2 - E_{\mathrm{s,oop}} = \frac{1}{2}(H_{\mathrm{k,eff}}^{\mathrm{avg}} + 4\pi M_{\mathrm{s}}) M_{\mathrm{s}} - E_{\mathrm{s,oop}}\,. \tag{3.6}$$

However, with the measured hysteresis loops on hand (Fig. 3.6), the energies can be determined much more precisely by a numerical integration of the loops which gives $E_{\mathrm{s,ip}} = (3.3 \pm 0.1) \times 10^6\,\mathrm{erg\ cm^{-3}}$ and $E_{\mathrm{s,oop}} = (5.9 \pm 1.0) \times 10^5\,\mathrm{erg\ cm^{-3}}$. With the energy density of the demagnetizing field of $2\pi M_{\mathrm{s}}^2 = (3.0 \pm 0.1) \times 10^6\,\mathrm{erg\ cm^{-3}}$, an uniaxial anisotropy of $K_{\mathrm{u}} = (5.7 \pm 0.3) \times 10^6\,\mathrm{erg\ cm^{-3}}$ is obtained. The coercive field of the continuous film is (118 ± 2) Oe.

3.2.4 Experimental setup

All synchrotron experiments presented in this thesis have been carried out at the UE52-SGM undulator beamline of the BESSY II synchrotron source. The APPLE II type undulator source [Bah01] of the beamline delivers soft x-ray radiation in the range between 90 eV and 1.5 keV with variable polarization, e.g. linearly polarized, and left or right circularly polarized light. When using a photon energy of 781.1 eV (wavelength $\lambda = 1.59$ nm) at the Co L_3-edge, the undulator is operated using radiation from its third harmonic. In this mode, the degree of circular polarization is 90 %.

The spherical grating monochromator of the beamline together with the exit slit (setting at 120 µm) generate an energy resolution ($E/\Delta E$) of 1625 as calculated by the beamline software. The beam is horizontally and vertically focused with a divergence of 6 mrad × 1 mrad (hor. × vert.) down to a spot size of horizontally 17.4 µm (FWHM) and the size of the exit slit in the vertical direction.

The actual scattering experiment is performed in the ALICE scattering chamber [Gra05; Gra03] built by the group of Prof. Zabel from the University of Bochum. Figure 3.7 depicts a sketch of the chamber design. The chamber was constructed as an in-vacuum diffractometer for magnetic samples. It is therefore not only possible to translate the sample in x, y, and z-direction, but also to rotate the sample along a vertical axis defining the horizontal scattering plane and the scattering angle 2θ. The scattered radiation is usually detected by a Si-diode detector which can be rotated in the scattering plane independently from the sample, e.g. for small-angle x-ray scattering (SAXS) experiments, but also in a θ-2θ-mode for reflectivity measurements. For the FTH studies, the chamber is additionally equipped with a charge-coupled device (CCD) camera in transmission geometry at a distance of 35 cm to 45 cm behind the sample depending on the required resolution

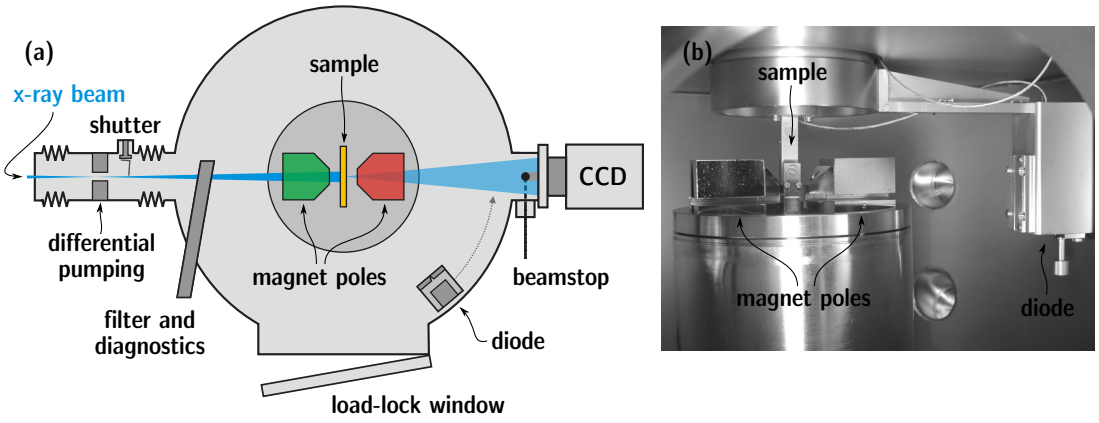

Figure 3.7: (a) Top-view sketch (not to scale) of the ALICE scattering chamber (reproduced from [Gü12]). **(b)** Photograph taken from the side of the chamber interior (taken from [Gra05]).

in Fourier space. The detector (PI-MTE, Princeton Instruments [Ins12]) uses a thinned, back-illuminated CCD chip being sensitive to soft x-rays with a quantum efficiency of 80 % at 780 eV photon energy and with a pixel fill factor of 100 %. The area of the CCD chip of 27.65 mm × 27.65 mm is given by the number of pixels of 2048 × 2048 and by the pixel size of 13.5 µm × 13.5 µm. The signal is usually read out with a pixel rate of 1 MHz resulting in a read-out time (full chip) of 4.2 s at a bit depth of 16 bits where the first 3.4 bits (FWHM) are influenced by noise and often the highest bit is not usable due to saturation of the pixels. During read-out, the x-ray beam is blanked by a shutter at the entrance of the ALICE chamber. In operation, the CCD chip is cooled down to −40 °C to −50 °C resulting in a strongly reduced thermal (dark) noise and, hence, making the read-out noise to the main source of noise in the signal. At 780 eV photon energy, the CCD is able to detect single photon events and a single pixel can store up to approximately 500 photons. The intense directly transmitted radiation from the sample is usually blocked by a beamstop. For the FTH measurements, the beamstop is made up of an epoxy-resin sphere with 0.5 mm to 1 mm diameter attached on 10 µm diameter tungsten wire which is supported by an aluminum frame [Sch07b]. The beamstop can be laterally aligned with respect to the CCD plane.

As the ALICE chamber was designed for magnetism research, an electromagnet is installed inside the chamber that can be rotated along the θ-direction. For all experiments in this thesis, the magnet poles are positioned in a way that the field is pointing in the direction of the incident beam, i.e. parallel to the sample normal. The poles are sliced along the path of the beam. Using a 5 mm gap between the poles, a maximum field of 0.72 T can be reached by the magnet with a remanence below 20 mT.

Due to the absorption of soft x-rays in air and due to the operation of the cooled CCD, the experiments have to be performed in vacuum. During the experiments the

ALICE chamber is pumped down to a pressure in the range of 10^{-6} mbar to 10^{-7} mbar. In order to meet the ultra-high vacuum (UHV) requirements of the beamline (10^{-8} mbar to 10^{-9} mbar), the experimental chamber is decoupled from the beamline by a differential pumping aperture with a diameter of 1.5 mm. The aperture is located approximately at the position of the beamline focus resulting in a distance of approximately 35 cm from the focal point to the sample position.

3.2.5 Local hysteresis loop

Magnetic FTH imaging is dependent on a precise tuning of the photon energy yielding the maximum x-ray magnetic circular dichroism (XMCD) absorption contrast (Sec. 2.5). This tuning is realized in an XMCD scan as presented in Fig. 3.9. Here, the transmitted circularly polarized x-rays are detected using the photodiode in an energy scan while alternately magnetically saturating the sample parallel or anti-parallel to the beam with the chamber magnet (Fig. 3.8). The diode signal is additionally normalized to the incoming beam intensity monitor provided by the total electron yield signal of the last beamline focusing mirror. The normalized difference of the resulting two transmission curves is then used as the XMCD (transmission) contrast P:

$$P = \frac{I_+ - I_-}{I_+ + I_-}\,, \tag{3.7}$$

where I_+ and I_- denote the normalized intensity signals for parallel or anti-parallel setting of the magnetization to the helicity vector of the incoming beam, respectively. In our experiment, the maximum XMCD contrast of almost 10 % in transmission is reached at $E = 779.8$ eV corresponding to a wavelength of $\lambda = 1.59$ nm. The XMCD setup was also used to measure a magnetic hysteresis loop of the sample complementary to the VSM measurements. The measurement is performed by monitoring the transmitted intensity of

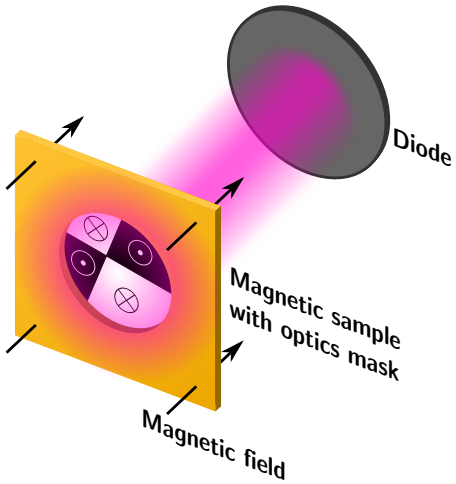

Figure 3.8: Setup for recording local hysteresis loops [Gü08]. Although the whole sample structure is illuminated on a large area, the x-rays are only transmitted where the object hole for the holography experiment was produced. An external magnetic field is applied parallel to the sample surface normal. The integrated intensity signal detected by the photodiode is determined by the difference in the areas taken by domains with magnetization pointing parallel or anti-parallel to the incoming beam direction.

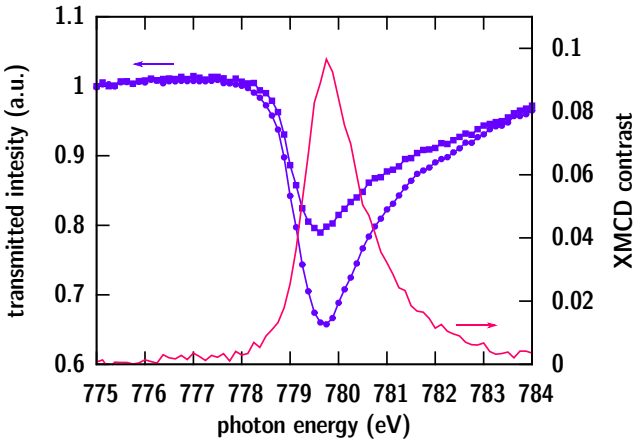

Figure 3.9: Energy scan at the Co L_3-edge using circularly polarized light while the sample is kept in saturation by an applied field. Due to the XMCD effect the intensity of transmitted x-rays through the sample depends on the magnetization direction (■ magnetization parallel to helicity vector, • magnetization anti-parallel to helicity). From these curves the energy-dependent XMCD contrast (Eq. 3.7) is calculated.

the circularly polarized x-rays through the sample while sweeping through the externally applied field. Due to the XMCD effect, the x-ray intensity transmission rate is dependent on the local magnetization direction and is given by the squared real part of the transmission function in Eq. 2.9 [Att00; Pfa11]:

$$\begin{aligned} t_\pm &= \exp\left\{-\frac{4\pi}{\lambda}(\beta \pm \Delta\beta)d\right\} \\ &\simeq 1 - \frac{4\pi}{\lambda}(\beta \pm \Delta\beta)d\,, \end{aligned} \tag{3.8}$$

when considering a thickness d of magnetized material, normal incidence conditions and out-of-plane magnetization. Neglecting the width of the domain walls, the net normalized magnetization is solely given by the difference of the fraction of sample area taken by the up domains (A_+/A) and the fraction taken by the down domains (A_-/A):

$$M = \frac{A_+ - A_-}{A_+ + A_-}\,, \tag{3.9}$$

with the total illuminated area $A = A_+ + A_-$. The total intensity transmitted through both types of domains is calculated as $I_0 A_\pm t_\pm$, where I_0 denotes the incoming photon fluence, i.e. given in units of photons/area. The total transmitted intensity is then obtained from the sum of both intensities:

$$\begin{aligned} I &= I_0(A_+ t_+ + A_- t_-) \\ &= I_0 \left\{ (A_+ + A_-) \underbrace{\left(1 - \frac{4\pi}{\lambda}\beta d\right)}_{t} + (A_+ - A_-) \underbrace{\frac{4\pi}{\lambda}\Delta\beta d}_{\Delta t} \right\} \\ &= I_0 A(t + M\Delta t)\,. \end{aligned} \tag{3.10}$$

Apart from an offset due to the transmission of the x-rays by the material, the net normalized magnetization is directly proportional to the intensity signal detected by the diode. For the sample under investigation in this study, the illuminated sample area is defined by the four small object holes. The proximity mask, thus, provides a technique for recording *local* hysteresis loops [Gü08]. The recorded integral signal is generated by the magnetization of the islands, but predominantly by the trenches in between according to the island fill factors as shown in Fig. 3.5. In addition, the impact from the islands is further reduced because of the thicker substrate due to the pillar structure. Within the 40 nm Si_3N_4 pillar material, 6 % of the x-rays are absorbed. In total, 23 % of the signal stem from the islands and 77 % from the trenches (Fig. 3.10). In particular for small applied fields below 1 kOe where the islands do not reverse their magnetization (Sec. 3.4), the determined hysteresis loop in Fig. 3.10(a) is governed by the behavior of the trenches. In comparison with the hysteresis loop of the continuous film (Fig. 3.6), the magnetic reversal of the trench material starts at similar fields around −1 kOe, but the following magnetization increase is not as rapid as for the continuous film. This observation indicates that the domain wall motion after formation of a reversed nucleus in the trench material cannot proceed on large areas. Instead, the propagation is hampered by an enhanced domain pinning in the trenches. This pinning is probably caused by the patterning of the substrate and by an irregular layer growth due to shading effects during sputter deposition.

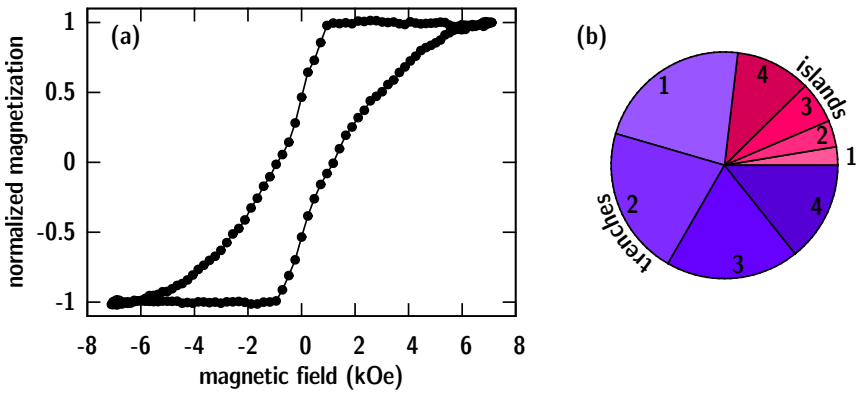

Figure 3.10: **(a)** Magnetic hysteresis loop of the BPM sample recorded with a photodiode detecting the directly transmitted radiation through the sample. Due to the XMCD effect, the x-ray absorption is dependent on the sample magnetization. The intensity is normalized to the intensity monitor of the beamline focusing mirror. Additionally, the constant intensity offset was subtracted and the resulting magnetization curve is normalized to saturate at ±1. **(b)** Composition of the integral signal measured in (a) calculated from the geometrical design of the sample and taking into account a slightly higher absorption at the island sites. One quarter of the signal is given by the magnetization of the islands, the remaining three quarters are assigned to the trenches. The numbering of the different bit patterns can be found in Fig. 3.3.

3.3 Holographic imaging of the bit-patterned media sample

During the beamtime of six 12-hour-shifts, in total, 73 holograms have been recorded. As each hologram is encoding four images, these numbers correspond to four images per hour including the time overhead for beamline, chamber and sample alignment and photon energy calibration.

For each dataset, two holograms, with left and right circularly polarized incident x-rays, were recorded with a total accumulation time between 350 s and 500 s depending on the available photon flux. A typical hologram of the BPM sample is presented in Fig. 3.11. In the center the light is blocked by a beamstop sphere attached to a thin, horizontally stretched wire. The central part of the hologram is particularly characterized by the diffraction of the radiation at the sample apertures resulting in the typical Airy pattern. The Airy pattern is additionally modulated by the interference between light passing through different apertures and by the interfering light from the reference holes. Another striking feature in the hologram is the appearance of interference peaks due the two-dimensional lattice of the bit pattern.

In the hologram taken with one helicity only, the magnetic scattering is superimposed by the much stronger charge scattering contributions from the apertures and the pre-patterned substrate. By taking the difference of holograms recorded with left and right circularly polarized x-rays the charge scattering is nearly completely subtracted from the hologram (Sec. 2.5). These difference holograms (Fig. 3.11) containing predominantly magnetic information are now further processed in the following way: First, the digital hologram is embedded and centered in a larger matrix (4096×4096 pixels) containing zeros elsewhere. This procedure is called zero-padding and helps to better represent non-periodic signals and to numerically improve the sampling in the reconstruction. Since the signal in the recorded difference holograms already approaches zero towards the edges of the CCD, applying an additional window function is not necessary. The zero-padding procedure results in a pixel resolution of 11.4 nm in the reconstruction. The center of the hologram, i.e. the pixel with zero momentum transfer ($q = 0$) is known from holograms taken without beamstop. In a next step, the shadow of the beamstop is filled with a smoothed radial heavy-side function of shape:

$$\mathrm{HS}(q) = \left[\exp\left\{(q - q_{\mathrm{HS}})/\sigma_{\mathrm{HS}}\right\} + 1\right]^{-1} , \tag{3.11}$$

where q_{HS} denotes the cut-off radius and σ_{HS} the width of the smoothed region. Finally, faulty pixels, e.g. due to cosmic rays, shadows from the beamstop wire and dust or defects in the CCD chip, are replaced by a local mean.

The reconstruction of the difference hologram is obtained by a Fourier transform of the hologram as exemplarily presented in Fig. 2.3(a) showing the real part only. The images of the four samples are formed with strong contrast on a very flat background. In the center of the reconstruction the auto-correlations and in the edges the cross-correlations of the four FOV emerge.

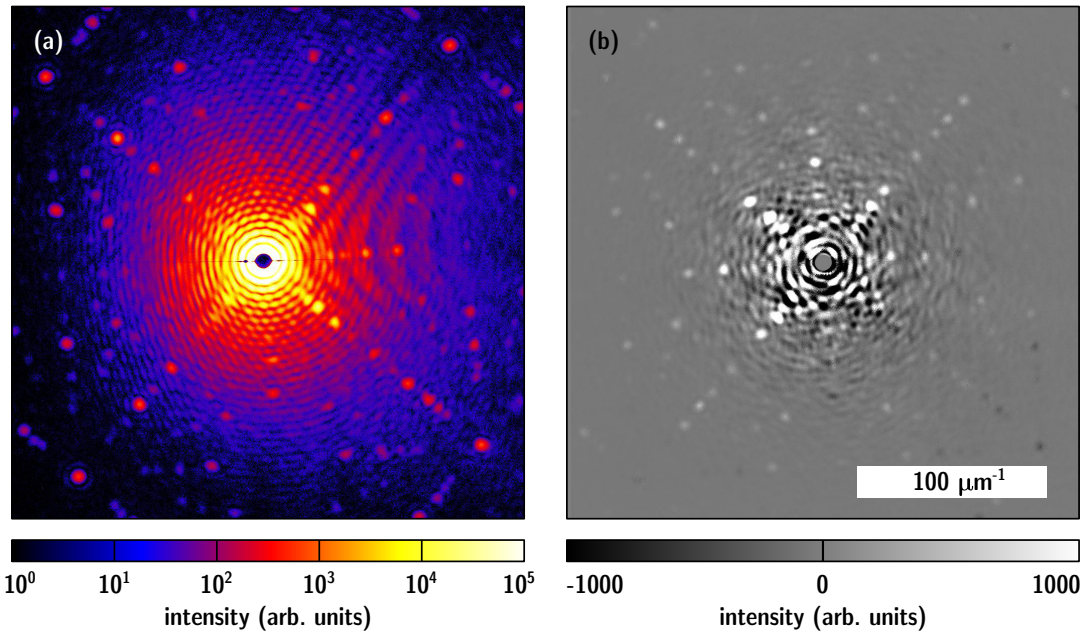

Figure 3.11: **(a)** Typical hologram of the BPM sample in logarithmic pseudo-color intensity scale and **(b)** difference hologram from holograms taken with left and right circularly polarized light in linear gray scale.

In order to gain the maximum magnetic contrast in the images, the signed magnitude of the signal was calculated as described in Sec. 2.5. In particular the phase of the reconstructed exit wave is manipulated referring to Eq. 2.57, i.e. the reconstructed complex value in all pixels is rotated in the complex plane by a constant angle α in a way that the magnetic contrast is maximized in the real part and vanishes in the imaginary part. The angle α was individually determined for every image by visual inspection. In theory one would expect, that for a photon energy calibration to maximum XMCD contrast, the initially reconstructed phases would already equal zero and magnetic contrast is found only in the real part. The deviation of the phases from zero is mainly explained by an improper centering of the hologram. If the hologram is miscentered by an offset $\Delta\boldsymbol{q} = (\Delta q_x, \Delta q_y)$, the reconstruction is superimposed by a phase gradient $\exp(\mathrm{i}\Delta\boldsymbol{q}\boldsymbol{r})$ [SN09]. In the present case, already a subpixel offset of half a pixel would induce a phase shift of 10° at the position of the images in the reconstruction matrix and the center position is known with a precision of at best one pixel. Unfortunately, finding the right offset $\Delta\boldsymbol{q}$ is a complicated task and cannot easily be automated. For this reason the phase shift over the small area of the reconstructed images is considered to be constant and is corrected as described above.

Examples of optimized reconstructions can be found in Fig. 3.12(b)–(e). The magnetic contrast is shown in gray scale with the magnetization in white and black areas pointing in opposite out-of-plane directions. An absolute magnetization value cannot be determined

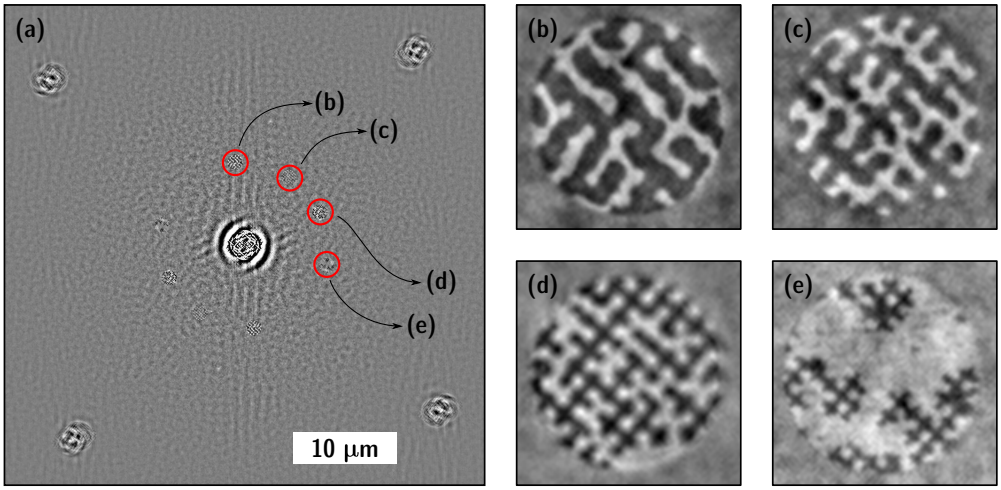

Figure 3.12: **(a)** Complete reconstruction matrix of a typical hologram (Fig. 3.11). In the center the auto-correlation of every individual object is located. The residual fringing is the result of the missing data in the center of the hologram due to the beamstop. Around the center the images of the four object holes and their twin images become visible. In the corners, weak object–object cross-correlations emerge. **(b–e)** Magnification of the image reconstructions. The magnetization is encoded as gray scale with white and black regions pointing into opposite directions. The images show the pattern ensembles with pitches: **(b)** 240 nm, **(c)** 200 nm, **(d)** 160 nm, and **(e)** 120 nm. The FOV has a diameter of 1.5 µm.

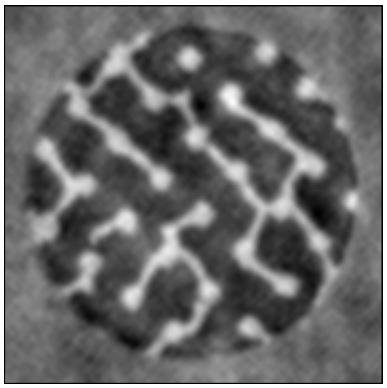

Figure 3.13: Magnetic trench material pinned at the patterned substrate. The FOV has a diameter of 1.5 µm, the pitch size is 240 nm.

as the intensity information at low momentum transfer is lost. All magnetic state images shown in this thesis are scaled to the minimum intensity value represented as black and the maximum intensity as white, i.e. the images are scaled to $\pm M_s$.

Since the aim of the experiment was the analysis of the switching behavior of the magnetic islands, the sample was investigated under different externally applied magnetic fields. The usual procedure was to first magnetically saturate the sample at a field of $H_{max} = \pm 7\,\mathrm{kOe}$ and then image the sample after certain field steps. Images taken during such a field sweep are presented in Figs. 3.14 and 3.15. As already pointed out, all four patterned areas are imaged simultaneously at the same external field values. After saturation at $-7\,\mathrm{kOe}$ the first image is taken before remanence at $-1.2\,\mathrm{kOe}$ still showing completely saturated areas. When approaching remanence the magnetic film in the trenches partially reverses its magnetization in the case of the 240 nm and 200 nm pitch samples while the samples with smaller pitch length stay saturated. The domain pattern is similar to the worm domain patterns known from continuous film Co/Pd or Co/Pt multilayer samples [Hel06; Hel07b]. In the 160 nm and 120 nm pitch samples, the coercive field of the magnetic film in the trenches is increased since the missing material at the island positions acts as defects and pinning centers [Alb09]. This pinning becomes also visible for the patterns with higher pitch when applying a field of 1.2 kOe and 2.3 kOe. At these fields values, the islands that have not switched appear on the background of the nearly completely reversed film in the trenches. But in addition, between the islands, bridges of non-reversed, pinned magnetic material in the trenches remains visible (Fig. 3.13). Between 2.3 kOe and 3.4 kOe the first islands start to reverse their magnetization. At 4.5 kOe slightly more than half of the islands has switched. The last islands switch between 4.5 kOe and 5.4 kOe and at 6.7 kOe the sample is completely saturated in the reverse direction compared to the situation at the beginning.

The difference of the coercive field of the magnetic island versus the continuous magnetic film is explained by the different reversal mechanism. Whereas a continuous film reverses via nucleation and rapid domain wall motion, the switching of an island is commonly described as a quasi-coherent rotation of the magnetization in the island volume. This mechanism is also known as Stoner–Wohlfarth behavior [Alb09; Hu05a; Sto06].

The majority of the holograms in this study was taken in applied field. However, for the field sweep presented in Figs. 3.14 and 3.15 also images in remanence have been recorded. In the figures, the remanent images after a certain field step are presented on the right side next to the in-field images. These images prove that although the film in the trenches partially switches back, the islands always retain their magnetization. This result does not play a role for the FTH study, but is important for MFM studies that can be performed in remanence only and for data storage applications where the information is stored and read out under remanent conditions.

In order to perform a statistical analysis of the switching behavior of the magnetic islands, the islands were labeled in a square matrix as shown in Fig. 3.5 using the positions known from the SEM image. A few labeled islands are not visible in the FOV and were ignored in the analysis. The magnetic state of every individual island was recorded for

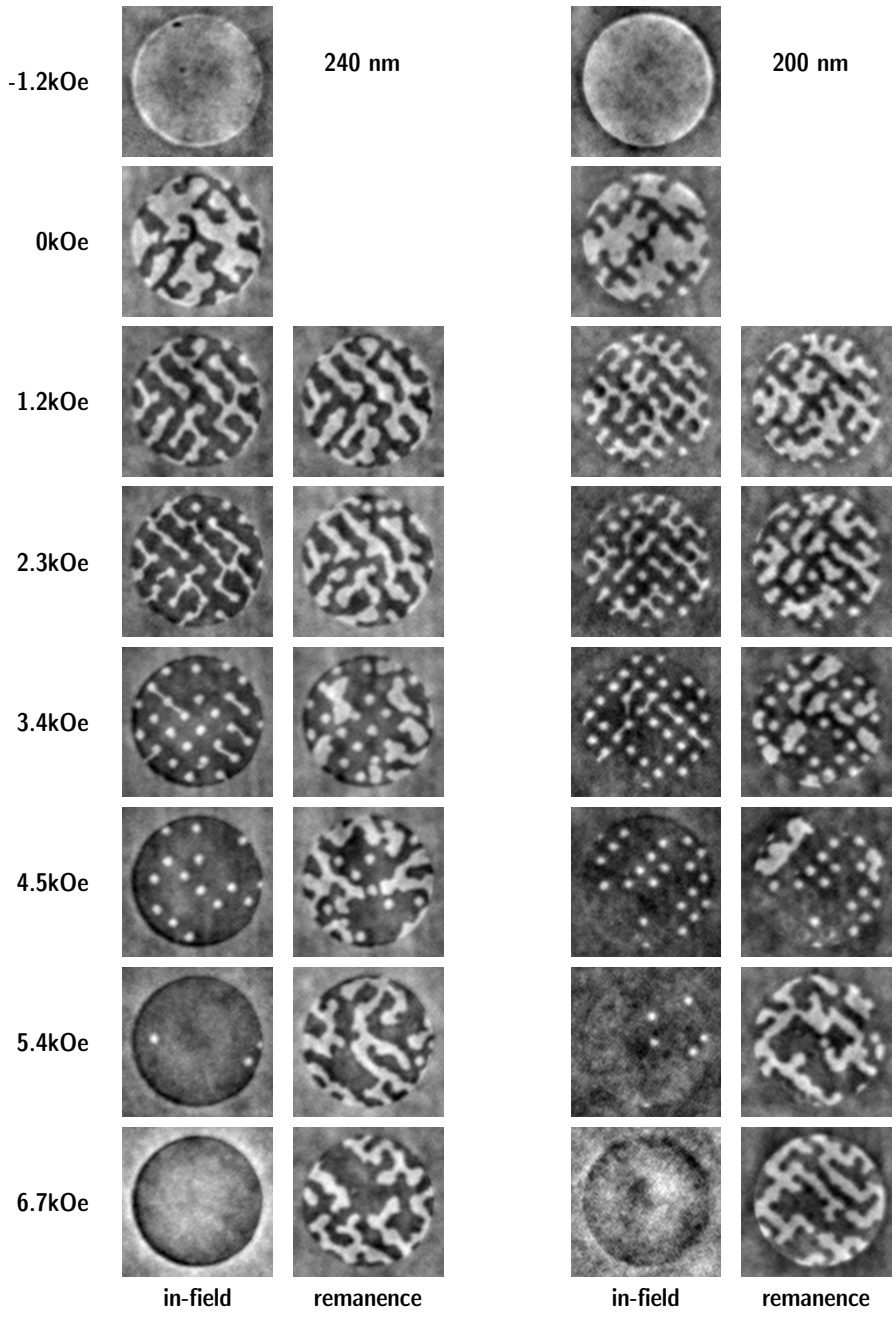

Figure 3.14: FTH reconstructions of the BPM sample in a magnetic reversal. Each double-column belongs to one BPM ensemble and each row is assigned to a certain field step. At the beginning of the image series the sample was saturated at $-7\,\mathrm{kOe}$. Then the field was swept in the indicated field steps. At each field step (except for the first two ones for obvious reasons) images in applied field (left side of each double-column) and in remanence (right side) were recorded. The FOV has a diameter of $1.5\,\mu\mathrm{m}$.

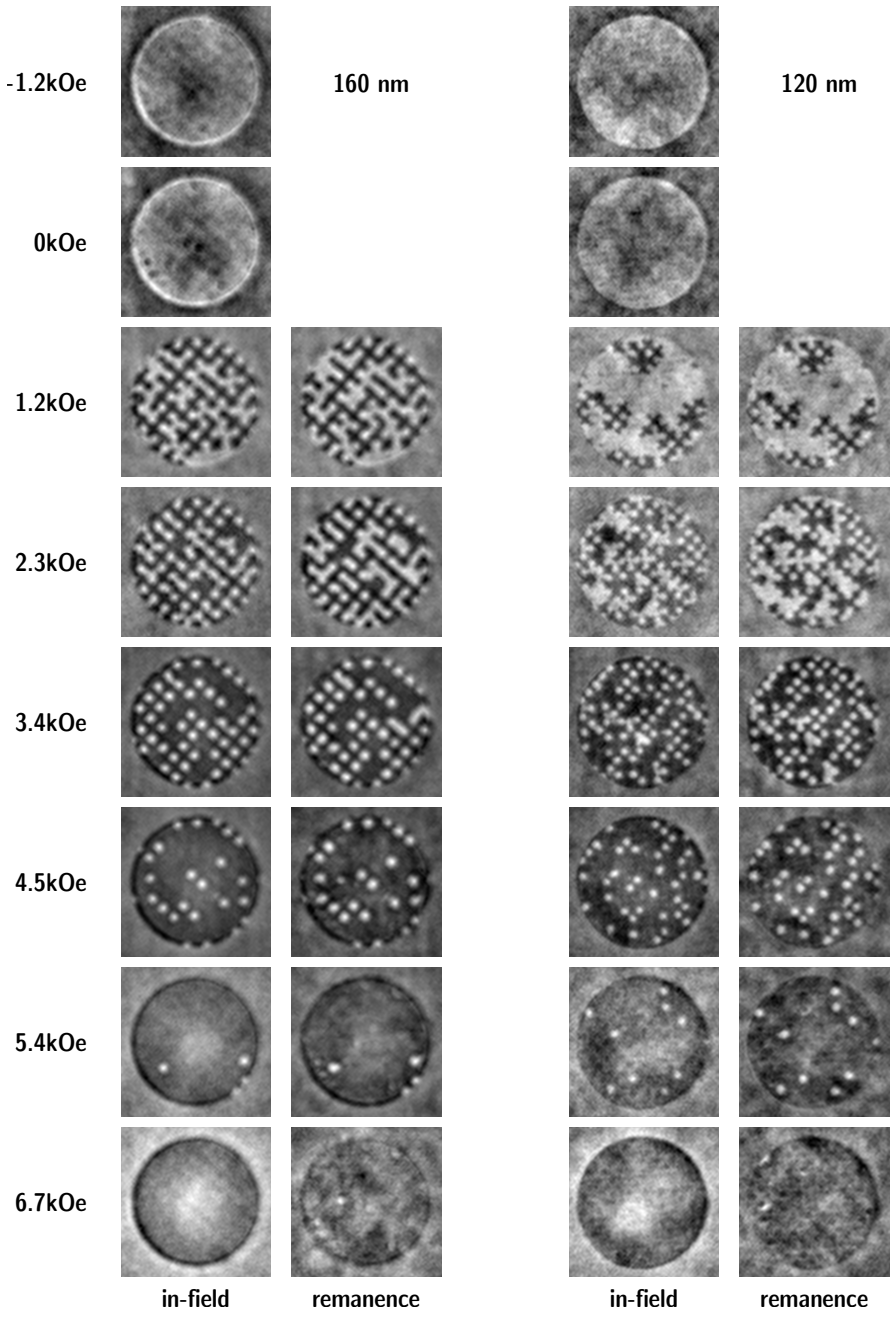

Figure 3.15: Continuation of Fig. 3.14.

every image. In total, $N(p = 240\,\mathrm{nm}) = 29$, $N(p = 200\,\mathrm{nm}) = 42$, $N(p = 160\,\mathrm{nm}) = 64$, and $N(p = 120\,\mathrm{nm}) = 112$ islands are visible in the four FOVs and have been investigated.

3.4 Influence of the magnetic interaction on the switching-field distribution

3.4.1 Bit-ensemble hysteresis loops

A major aspect for the sample design used in this study was the systematic investigation of the magnetic interaction in BPM. As the islands are decoupled with respect to exchange interaction, the magnetic interaction is mediated via stray fields from the islands, but also from the magnetically active trench material. As the strength of the stray fields is strongly dependent on the distance between the islands, i.e. the pattern pitch, this parameter was varied in the study while all other parameters during preparation and experiments were kept constant. In particular, the size and the square lattice arrangement of the islands, and the composition of the magnetic layer system is identical for all samples. Furthermore, by employing the multi-object capabilities of FTH imaging, it was possible to fabricate the samples on the same substrate. The pre-patterned substrate and the magnetic layer are therefore prepared exactly under the same conditions and the samples are imaged in exactly the same environment including external magnetic field and temperature.

In a first analysis step, a switching hysteresis loop of each imaged island ensemble was compiled from 60 images recorded in applied field H with 22 different field values. The hysteresis loops were generated by counting the number of reversed islands $n(H)$ only. Contributions from the trench material or due to slightly different island volumes are eliminated in this way. The normalized magnetization of the ensembles in the FOV is calculated as:

$$M(H) = \frac{2n(H)}{N} - 1\,. \tag{3.12}$$

The total number of imaged islands is very limited which introduces a certain uncertainty to this procedure. Imaging N switched or non-switched islands from a population of many more islands[1] is described by a hypergeometric distribution with the mean $n(H)$ and the variance of this distribution given by:

$$\sigma_n^2 = n\left(1 - \frac{n}{N}\right)\,. \tag{3.13}$$

1 In probability theory, one would speak of N draws without replacement.

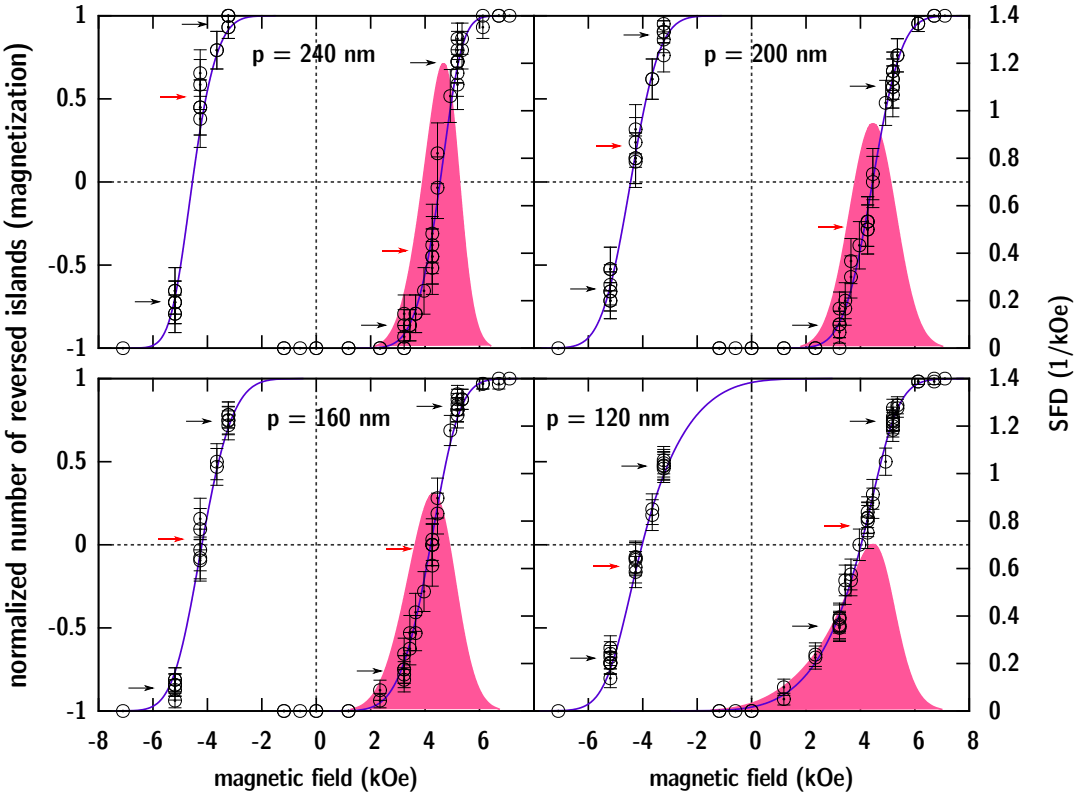

Figure 3.16: Hysteresis loops for the island ensembles visible in each FOV with different pattern pitch (p). The data points for the magnetization (left axis) are obtained by counting the number of reversed islands. The lines represent a fit to the data using an asymmetric error function. The filled areas show the corresponding SFD (right axis). The arrows mark the measurement points to obtain the switching probability and identifying hard and easy switchers.

With the error of the magnetization calculated as $\Delta M = 2\sigma_n/N$ one yields:

$$\Delta M = \frac{2}{N}\sqrt{n\left(1-\frac{n}{N}\right)}\,. \tag{3.14}$$

The resulting hysteresis curves for all samples are presented in Fig. 3.16. Following the work of O. Hellwig et al. [Hel07a], the data points are fitted with an asymmetric error function corresponding to an asymmetric Gaussian distribution for the SFD. This function is analytically defined only as an inverse function:

$$H(M) = H_\mathrm{c} + \sqrt{2}\sigma_\mathrm{SFD}\frac{\mathrm{erf}^{-1}(M)}{1+\alpha_\mathrm{SFD}M}\,, \tag{3.15}$$

with H_c denoting the coercive field, σ_{SFD} the width of the SFD and α_{SFD} the asymmetry parameter.

As can be seen in Fig. 3.16, the given fit function models the island switching remarkably well. In this work, the SFD of the island ensemble is defined as the derivative of the magnetization curves:

$$\mathrm{SFD}(H) = \frac{\mathrm{d}M(H)}{\mathrm{d}H}\,, \tag{3.16}$$

that is presented for the ascending branch only. The resulting fit parameters are listed in Tab. 3.1 and displayed in Fig. 3.17 in dependence on the pattern fill factor. Due to the slicing of the poles of the ALICE chamber magnet (see Sec. 3.2.4), the magnetic field is inhomogeneous on millimeter length scales. As it cannot be guaranteed that the magnet calibration was performed at exactly the same position where the sample was located during the measurements, a systematic error of maximum 10 % in the field values cannot be excluded. This systematic error has to be taken into account for the values given for H_c and σ_{SFD}, but must not be considered for the asymmetry α_{SFD} and the relative SFD $2\sigma_{SFD}/H_c$ additionally given in Tab. 3.1 The fits which are additionally presented in Fig. 3.17 will be explained in Sec. 3.4.2. At this point, only a qualitative discussion of the hysteresis loops is given.

The hysteresis loops (Fig. 3.16) and the fit results (Fig. 3.17) reveal that the switching behavior of the island ensembles is strongly influenced by the inter-island interaction as the magnetostatic interaction is strongly dependent on the distances between the islands. In the investigated range of pattern pitches, the island coercivity decreases with the fill factor while the SFD width increases. Accordingly, the full width of the relative

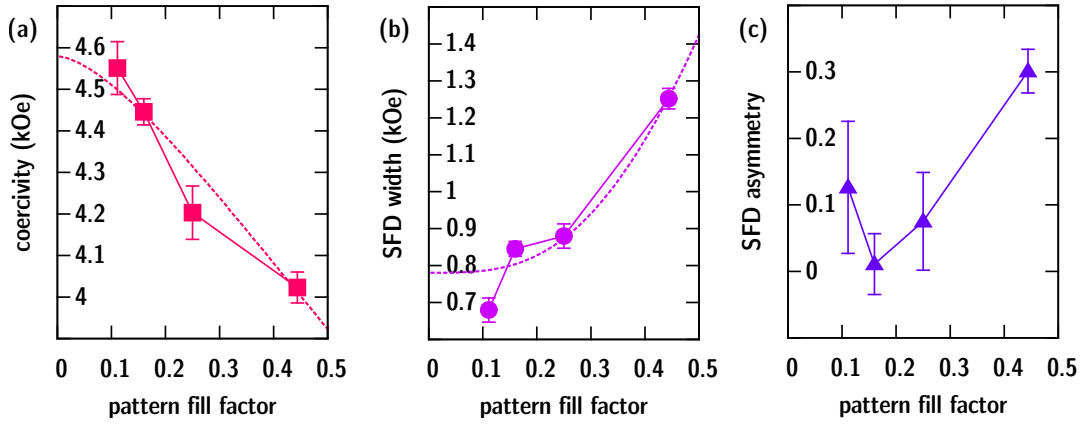

Figure 3.17: Fit results for the hysteresis loops presented in Fig. 3.16 in dependence on the fill factor $f = 4ab/p^2$. **(a)** Coercivity H_c, **(b)** SFD width σ_{SFD}, and **(c)** asymmetry parameter α_{SFD}. The dashed lines in **(a)** and **(b)** are fits to the data using a magnetostatic model that is described in detail in Sec. 3.4.2.

sample	pitch (nm)	fill factor	H_c (kOe)	σ_{SFD} (kOe)	α_{SFD}	$2\sigma_{SFD}/H_c$
1	240	0.111	4.55 ± 0.06	0.67 ± 0.03	0.12 ± 0.10	0.30 ± 0.02
2	200	0.160	4.45 ± 0.03	0.85 ± 0.02	0.01 ± 0.05	0.38 ± 0.02
3	160	0.250	4.20 ± 0.06	0.88 ± 0.03	0.08 ± 0.07	0.42 ± 0.02
4	120	0.444	4.02 ± 0.04	1.25 ± 0.03	0.30 ± 0.03	0.62 ± 0.02

Table 3.1: Fit results for the hysteresis loops presented in Fig. 3.16. The fits (dashed lines) in **(a)** and **(b)** are explained in Sec. 3.4.2.

SFD $2\sigma_{SFD}/H_c$ drastically changes from $(30 \pm 2)\,\%$ (240 nm pitch) to $(62 \pm 2)\,\%$ (120 nm pitch). In general, a dependence of the coercive field on the island-island interaction is not expected as on average the stray fields from the neighboring islands vanish in this situation. The observed change is, thus, attributed to the influence of the magnetic trenches. In the following, a brief and only qualitative explanation for the observations is given. In Sec. 3.4.2, these considerations lead to a magneto-static model of the BPM system that finally is able to quantitatively interpret the results.

For small fill factors, i.e. in the limit of very sparse islands, the interaction between the islands vanishes, but the islands will be influenced by the magnetic film surrounding the islands. As the film magnetization will reverse and saturate at smaller fields than the islands' switching fields, the magnetic state of the unswitched island is additionally stabilized. The stray fields induced by the film will reduce the effectively acting field on the island and the observed coercive field of the SFD increases from the intrinsic value. On the other hand, the width of the SFD will not be changed from the intrinsic value in the case of a large pattern pitch as every island experiences the same field offset from the surrounding magnetic film.

When looking at samples with high fill factors, i.e. very dense pattern, the influence of the trench material will diminish and the coercivity will approach its intrinsic value. However, the width of the SFD will be much more broadened due to the increasing island-island interaction via stray fields. In the beginning of the reversal process, at low fields, when all islands still retain their magnetization, the effective field acting at each island will be increased by the stray field from the neighboring islands leading to a reversal of the islands with low intrinsic switching field at even lower fields than expected from the intrinsic value. The opposite scenario is established at high external fields when the reversal of the ensemble is nearly accomplished. In this case, the magnetization state of the last remaining non-reversed islands will be stabilized due to the stray fields from the neighboring (already reversed) islands and the switching fields shift to higher values. Both effects result in a significant broadening of the SFD. The applied field where the reversal is initiated and the field where the island ensemble magnetization saturates are depicted in Fig. 3.18. The values have been obtained by applying a threshold of 2 % and 98 % reversed islands to the fitted SFD, respectively. Of course, these numbers are arbitrarily chosen and different limits would result in a shift of the field values. The actual choice is motivated by the fact that the gained field values closely match the experimentally observed first or

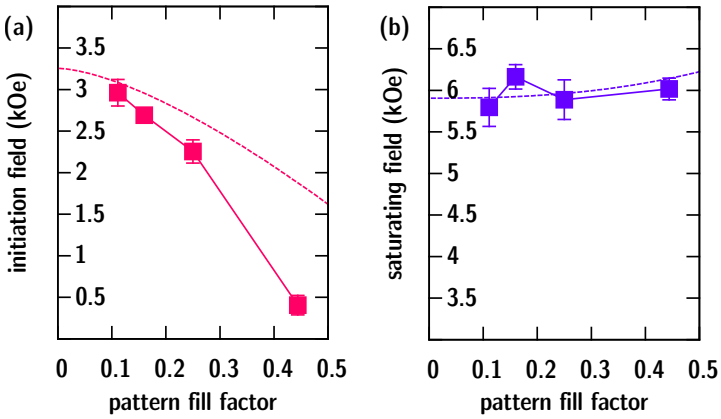

Figure 3.18: Field values from the fits in Fig. 3.16 **(a)** where the island reversal is initiated and **(b)** where it saturates. The thresholds were set to 2 % and 98 % switched islands, respectively. The dashed lines correspond to fits using the magnetostatic model developed in Sec. 3.4.2. As the model is not able to reproduce the observed initialization fields, the "fit" in (a) was realized by using the same (negative) field offset from the coercive field (Fig. 3.17) as fitted in (b).

last switching events. A first and maybe surprising observation in this plots is the fact, that the initializing field strongly depends on the fill factor while the saturation field stays nearly constant.

The just described two extreme points of the onset of the islands switching and its termination in the hysteresis loop are important for the present study of these systems, but also from the application point of view. In this study, these points will be further investigated as they are easy to model and because here the most singular islands, later called easy and hard switchers, can be identified. In the application of BPM as storage media, these points gain their relevance from the fact that data integrity has to be ensured during the writing of a bit. The saturation field defines the minimum write field of the write head as every islands must be writable by the head. And the initialization field defines the maximum allowed stray field from the head in order to avoid any influence on neighboring bits during a write process.

Up to now, the observed asymmetry in the hysteresis loops has not been considered in the qualitative discussion of the observations. The results of the study so far clearly suggest that the asymmetry is caused by the magnetostatic interaction as it increases with the pattern fill factor. The asymmetry parameter seems to be below 0.1 for low fill factors, when the SFD should be similar to the intrinsic distribution. This finding is in contrast to results presented in Ref. [Hel07a] where the main contribution to the asymmetry is found in the intrinsic SFD. Other studies [Gar95; Gun94] suggest, that the asymmetry is caused by the experimental method of ramping the field itself. This effect will be discussed in more detail in Sec. 3.5.

3.4.2 Magnetostatic model

Demagnetizing field of an island

In an ensemble of magnetic islands that are decoupled in terms of exchange interaction, the interplay between the island is mediated via magnetic stray fields. These fields are generated by the magnetization of the island material. The existence of the fields is a consequence that the $\boldsymbol{B}$-field has no divergence: [Coe10; Sto06]. In general, the $\boldsymbol{B}$-field is given by:

$$\boldsymbol{B} = \boldsymbol{H} + 4\pi\boldsymbol{M}\,. \tag{3.17}$$

In free space, i.e. without any magnetized material ($\boldsymbol{M} = 0$), $\boldsymbol{B}$ and $\boldsymbol{H}$ are indistinguishable. On the other hand, a magnetized body will always contain sources and sinks of magnetization at its surface (Fig. 3.19(a)). In order to provide the divergenceless of the $\boldsymbol{B}$-field, an additional magnetic field has to exist which accounts for the magnetization. The $\boldsymbol{H}$-field may be split into two contributions, the externally applied field ($\boldsymbol{H}_\mathrm{c}$) usually produced by charge currents and the field created by magnetization contributions ($\boldsymbol{H}_\mathrm{d}$). $\boldsymbol{H}_\mathrm{d}$ is called the demagnetizing field or the stray field. The reason for the two different names lies in the nature of the field as illustrated in Fig. 3.19(b). Inside the magnetized volume the field points in the opposite direction as the magnetization and outside the magnetized material the field does not vanish. The stray field can be approximated by a dipolar field for small magnetic particles and large distances from the particle. The terms demagnetizing, stray or dipolar field are often used as synonyms.

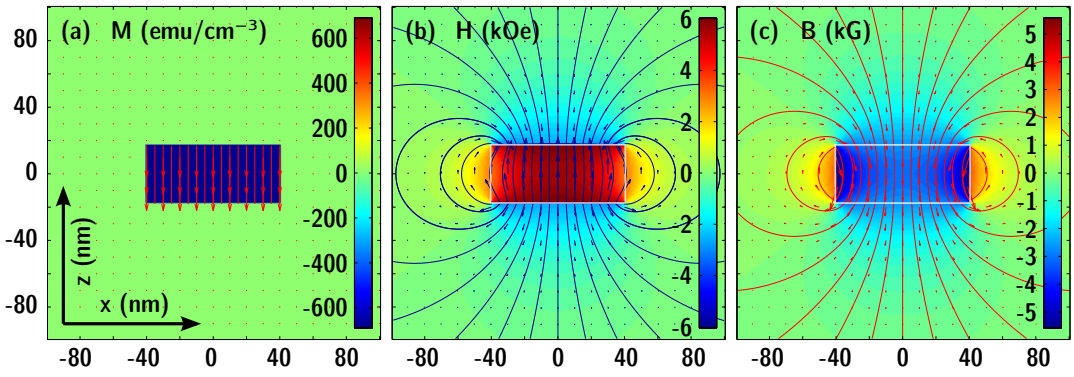

Figure 3.19: **(a)** Magnetization $\boldsymbol{M}$, **(b)** demagnetizing field $\boldsymbol{H}$ and **(c)** $\boldsymbol{B}$-field for an uniformly magnetized rectangular prism in the absence of any externally applied field. The fields were analytically calculated using Eqs. 3.18 to 3.22. The dimension of the body were chosen to match the size of a BPM island. For the presentation, the x–z-plane was selected where the y-component of all fields vanishes. In the background, the z-component of each field is shown encoded in a pseudocolor scale. On top, selected field lines and field vectors are drawn.

In general, the demagnetizing field of a particular volume having a certain shape is calculated with the help of the demagnetizing tensor N_{ij} related to this shape:

$$H_i = -4\pi \sum_j N_{ij} M_j \qquad i,\, j = x,\, y,\, z\,. \tag{3.18}$$

An analytic expression of N_{ij} only exists for a few basic, i.e. highly symmetric shapes, such as ellipsoids, cylinders and prisms. The magnetic islands in this study are approximated of having the shape of rectangular prisms ($2a \times 2b \times 2c$) (Fig. 3.20). The analytic solutions for the demagnetizing tensor of a prism were derived by Joseph and Schlömann [Jos65]:

$$\begin{aligned} N_{zz} = (1/4\pi)\{&\cot^{-1} f(x,y,z) + \cot^{-1} f(-x,y,z) \\ &+ \cot^{-1} f(x,-y,z) + \cot^{-1} f(x,y,-z) \\ &+ \cot^{-1} f(-x,-y,z) + \cot^{-1} f(-x,y,-z) \\ &+ \cot^{-1} f(x,-y,-z) + \cot^{-1} f(-x,-y,-z)\} \end{aligned} \tag{3.19}$$

$$N_{xz} = \frac{1}{4\pi} \ln \left\{ \frac{g(x,y,z;a,b,c)g(x,y,z;-a,-b,c)g(x,y,z;-a,b,-c)g(x,y,z;a,-b,-c)}{g(x,y,z;-a,b,c)g(x,y,z;a,-b,c)g(x,y,z;a,b,-c)g(x,y,z;-a,-b,-c)} \right\} \tag{3.20}$$

with:

$$f(x,y,z) = \frac{\sqrt{(a-x)^2 + (b-y)^2 + (c-z)^2}(c-z)}{(a-x)(b-y)} \tag{3.21}$$

$$g(x,y,z;a,b,c) = (b-y) + \sqrt{(a-x)^2 + (b-y)^2 + (c-z)^2}\,. \tag{3.22}$$

Due to the symmetry, all other components of N_{ij} are obtained by interchanging x, y, z and similarly a, b, c.

The results of the analytical calculation for demagnetizing field of a model island (Fig. 3.20) are presented in Figs. 3.19 and 3.21. The design parameters of the BPM structure were used for the dimensions of the prism, that is $2a = 2b = 80\,\text{nm}$ and $2c = 32.4\,\text{nm}$. The space origin is set to the center of the island. The out-of-plane magnetization (M_s) is pointing along the c-axis being parallel to the z-direction. Figure 3.19 shows an x–z-slice through the island's center. The demagnetizing field inside the island has a strength

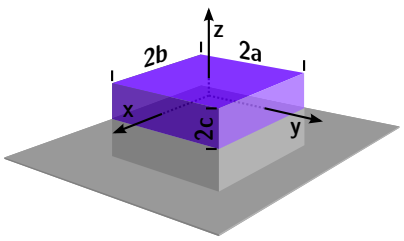

Figure 3.20: Coordinate system and geometry of the model for calculating the demagnetizing field of an island (violet) on the patterned substrate (gray).

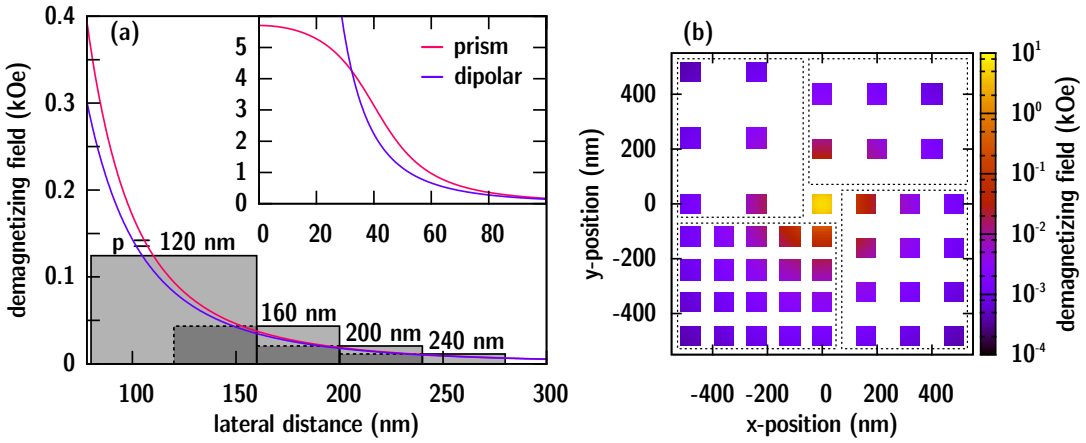

Figure 3.21: Stray field (z-component) of a single magnetic island with a prismatic shape. **(a)** Field strength along the x- (or y-) direction at $z = 0$ calculated using either the solution for a magnetized prism or assuming a dipolar field. The main plot shows the region of the inter-island distances, where the field is nearly dipolar. The gray boxes visualize the position, lateral size (box width) and the mean experienced stray field (box height) of the nearest neighbor island for each pattern pitch. The inset displays the field inside the island and the field in close proximity to it. In this region the dipolar approximation diverges and the prism solution has to be employed. **(b)** 2D map (x–y-plane) of the stray field (z-component) only at the positions of the islands in the 2D lattice. In each quadrant one of the four pattern is visualized.

of up to 6 kOe and laterally extends beyond the borders of the island. This external, demagnetizing field is responsible for the inter-island interaction which is investigated in more detail in Fig. 3.21. In the direct vicinity of an island, the stray fields are on the order of 0.1 kOe but with increasing distance they quickly diminish. The stray field is nearly dipolar (deviation below 10 %) at distances above 140 nm and may be calculated as:

$$\boldsymbol{H}(\boldsymbol{r}) = \frac{2a\,2b\,2c}{4\pi}\left(\frac{3\boldsymbol{r}(\boldsymbol{M}\cdot\boldsymbol{r})}{r^5} - \frac{\boldsymbol{M}}{r^3}\right), \tag{3.23}$$

which in the x–y-plane for out-of-plane magnetization simplifies for the z-component to:

$$H_z(r) = \frac{2a\,2b\,2c\,M_\mathrm{s}}{4\pi\,r^3}. \tag{3.24}$$

In order to obtain the total stray field acting on one specific island in an array of islands, one has to numerically sum up the stray field values over all islands. The maximum interaction impact is reached in the extreme case that all island are equally magnetized. Then, the total field can be estimated as $9H_\mathrm{i}$ with H_i being the nearest neighbor interaction field and under the assumption that the field is nearly dipolar [Ros01]. Consequently, the

interaction field in the used BPM sample reaches values up to 1 kOe. In the above described case, the field is demagnetizing, i.e. it promotes reversal. In the opposite case with a single remaining non-switched island surrounded only by reversed islands, the field hampers a reversal of the remaining bit. For the smallest fill factor, the maximum interaction field stays below 0.1 kOe indicating a very low stray field interaction in this system.

Demagnetizing field of the trench material

As previously pointed out, there is also a considerable magnetostatic influence of the trench material on the magnetic islands. It is possible to analytically model the stray fields from the trenches by the following consideration: When the magnetic layer is deposited, the pillars of the pre-patterned substrate create voids in the otherwise continuous magnetic layer. Such a single void has the same, but inverted, stray field as the corresponding missing prism of magnetized material would have [Sto06]. Consequentially, the resulting demagnetizing field of a single void is calculated from the difference of the demagnetizing field of a continuous magnetic film and a magnetized island which can be perceived as an anti-void. An (infinitely) extended thin film that is magnetically saturated in the out-of-plane direction does not have any stray field outside the material [Sto06]. The magnetization is completely compensated by the internal demagnetizing field of $4\pi M_s$. With the help of the analytic expressions for a magnetized prism given above (Eq. 3.19), the stray field at the actual position of the islands (40 nm above the film) is readily obtained as shown in Figs. 3.22 and 3.23. The geometrical parameters of the void are identical

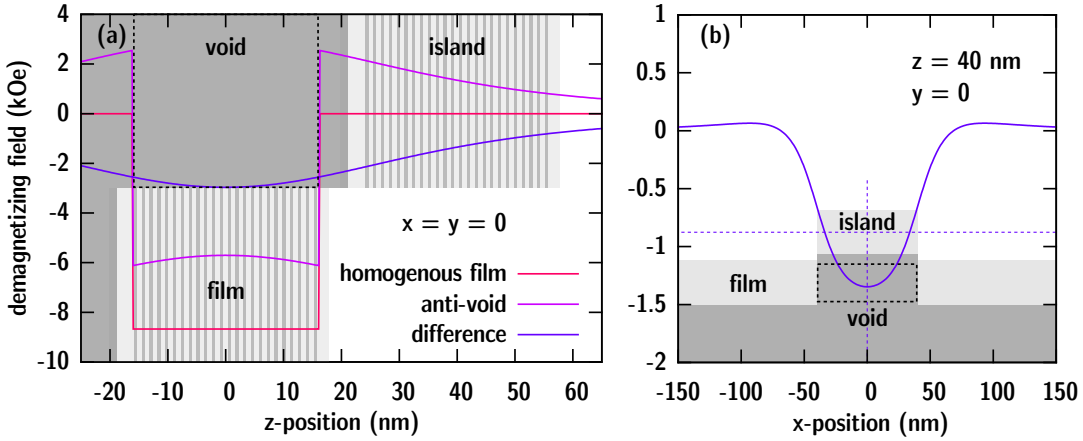

Figure 3.22: Demagnetizing field (z-component) of a homogeneous magnetic film containing a square void. **(a)** A plot along the z-axis through the center of the island. The field is retrieved from the difference of the fields created by a continuous film and by an anti-void. **(b)** Slice along the x-axis. In order to promote a better orientation, the sample geometry is sketched in the background of each plot. The dashed lines in (b) mark the position, where the field slices have been calculated.

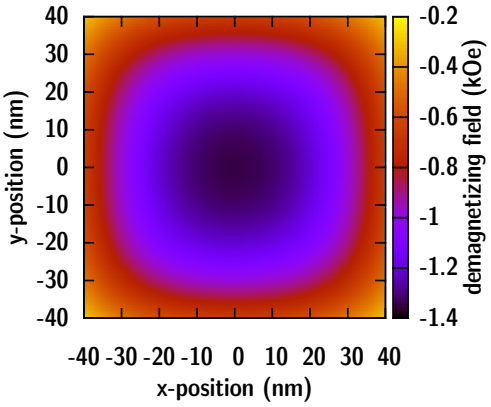

Figure 3.23: Demagnetizing field in the x–y-plane of a homogeneous magnetic film containing a square void calculated at the position of the magnetic island. The presented area corresponds to the size of the island.

to the island parameter. Inside the island, the stray field reaches maximum magnitudes of 1 kOe to 2 kOe. In the case that the film and the island have opposite magnetization, these fields stabilize the state of the island, i.e. they increase the external field needed to switch the island. In order to account for the whole array of voids, the field values at a certain position have to be summed up over all voids. This procedure leads to a reduction of the stray field since the fields of the neighboring voids point into the opposite direction (Fig. 3.22(b)).

Summary of demagnetizing fields

In summary, there are three different field contributions modifying the external field and, thus, influencing the switching field of an island: First, the internal demagnetizing field of the island itself (H_{internal}) which is of course independent from the pattern pitch. Second, the interaction field from the neighboring islands (H_{island}), and third, the stray fields from the trenches (H_{trench}). In Fig. 3.24 the magnitude of the z-component of these fields inside an island for the different pattern arrangements is presented. For the stray fields from the islands and the trenches, the fields from all sites in the pattern array have been numerically integrated up to a distance where the magnitude of the stray field falls below 0.1 Oe. In the bottom row of the figure, three prominent situations for a not yet switched bit are investigated: First, the film in the trenches has already completely reversed while all islands stay unaltered ($H_{\mathrm{internal}} + H_{\mathrm{trench}} + H_{\mathrm{island}}$), second, the coercive state ($H_{\mathrm{internal}} + H_{\mathrm{trench}}$), and third, the situation where all islands except for the one under consideration have reversed ($H_{\mathrm{internal}} + H_{\mathrm{trench}} - H_{\mathrm{island}}$). Note that the configuration of switched and non-switched islands in the coercive state is supposed to be random. In this case, the average demagnetizing field from neighboring islands will vanish. If short-range correlations are present and the system tends to form a checkerboard-like state, a small stray field offset from the islands has to be still considered. For an ideally alternating checkerboard pattern this field would be as high as -0.03 kOe to -0.26 kOe depending on the pattern pitch. As shown in Sec. 3.6, the correlations in the present sample are very

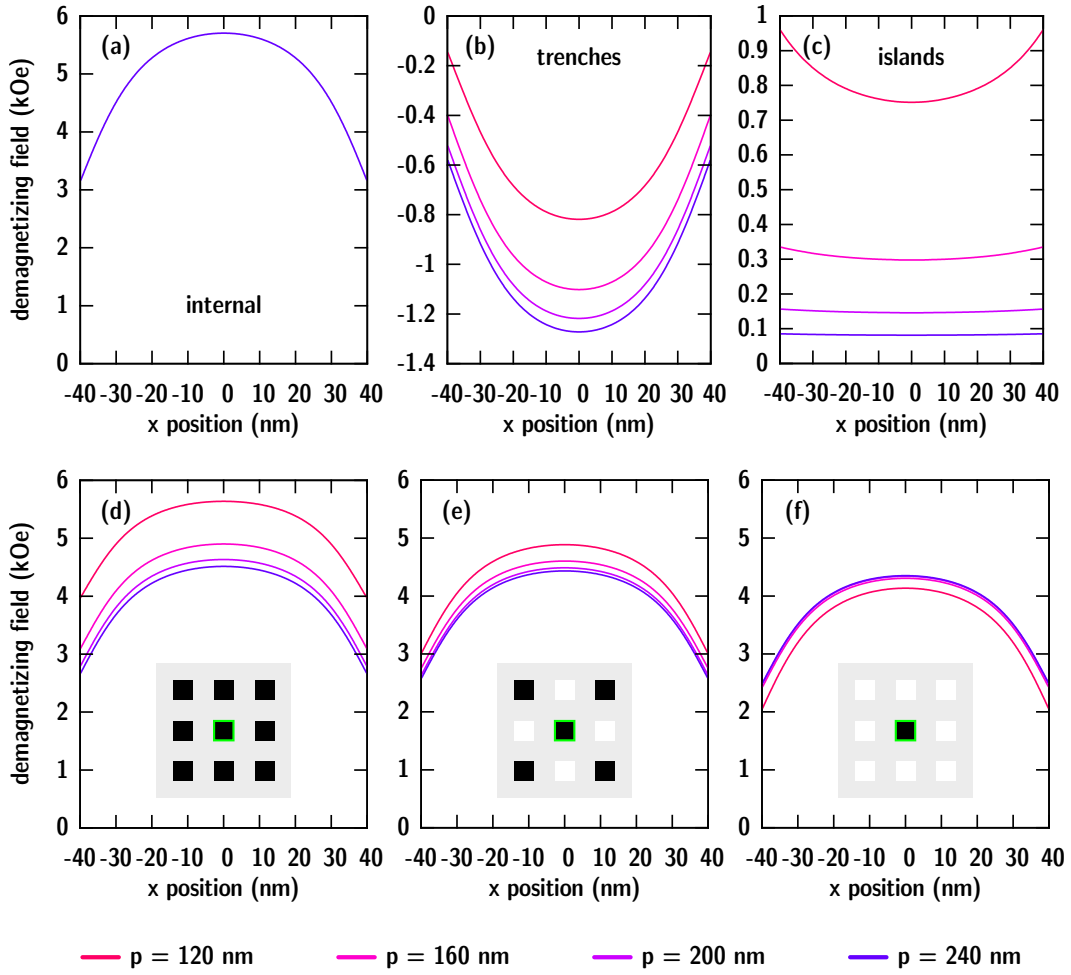

Figure 3.24: Summary of the calculation of demagnetizing fields. All plots show a slice of the demagnetizing field (z-component) along the x-axis inside an island. **(a)** Internal demagnetizing field created by the magnetization of the particle itself (H_{internal}). Of course, this field is independent of the patterning pitch. **(b)** Demagnetizing field created by the surrounding trench material (H_{trench}). It is assumed that the material is saturated (i.e. the absence of any domains) and that the magnetization is pointing in the opposite direction compared to the island's magnetization. **(c)** The stray field created by the pattern ensemble in the case that all islands have the same magnetization (in this case parallel to the magnetization of the island under consideration) (H_{island}). **(d)**–**(f)** The demagnetizing field acting inside an island for three different prominent cases: **(d)** Initiation of the island switching ($H_{\text{internal}} + H_{\text{trench}} + H_{\text{island}}$). **(e)** Coercivity ($H_{\text{internal}} + H_{\text{trench}}$). The magnetic configuration is supposed to be random, in particular it is not checkerboard-like. **(f)** Saturation of the reversal ($H_{\text{internal}} + H_{\text{trench}} - H_{\text{island}}$). Although the "situation sketches" in the plots only show the nearest neighbors, the calculation was performed for the whole ensemble.

weak and are therefore not considered here.

With the plots in Fig. 3.24, it is possible to confirm that most of the experimental observations in Sec. 3.4 can be explained by magnetostatic interactions in the sample system:

1. Due to the influence from the trench material, the coercivity is dependent on the fill factor (Fig. 3.17(a) and 3.24(e)). In Fig. 3.17(a), the experimental values were fitted with the model: $H_\mathrm{c} = H_\mathrm{c,i} + H_\mathrm{trench}(f)$, where $H_\mathrm{c,i}$ denotes the intrinsic coercivity and $H_\mathrm{trench}(f)$ is taken from the calculations in Fig. 3.24(e). Note that the trivial offset $H_\mathrm{c,i}$ is the only fit variable in this fit. From this point of view, the fit models the measurement remarkably well, confirming the validity of the assumed trench–island interaction. The intrinsic coercivity was determined with $H_\mathrm{c,i} = (3.12 \pm 0.02)\,\mathrm{kOe}$.

2. The island–island interaction clearly influences the effective H-field at the islands as it is the only changing parameter in the plots in Fig. 3.24(d)–(f). In accordance with the experimental results (Fig. 3.17(b)), the change in the demagnetizing field during a hysteresis loop is largest for the highest fill factor. Using a fit function of the form:

$$\sigma_\mathrm{SFD} = \sqrt{\sigma_\mathrm{SFD,i}^2 + (k_\mathrm{island} H_\mathrm{island}(f))^2}\,, \tag{3.25}$$

   a phenomenological model is applied to the experimental data for the SFD width as presented in Fig. 3.17(b). The function is motivated by the fact, that the intrinsic width of the SFD ($\sigma_\mathrm{SFD,i}$) is additionally broadened by the interaction field which changes by $2H_\mathrm{island}$ in a complete island reversal process. The constant k_island is a phenomenological parameter. If the broadening was only due to the interaction field, its value should be around 0.68, corresponding to the σ-width of the interaction SFD. The fit performs satisfactorily resulting in $\sigma_\mathrm{SFD,i} = (0.78 \pm 0.05)\,\mathrm{kOe}$. However, k_island is fitted with 1.22 ± 0.14 which suggests that either the interaction fields are stronger than calculated or there is another additional effect that broadens the SFD and that also depends on the fill factor. In addition, the validity of the assumption that k_island can be treated as being independent of the fill factor is questionable, in particular in the light of the observation discussed in the next point.

3. The observation, that the field where the reversal is initiated is strongly dependent on the fill factor while the saturation field stays nearly constant (Fig. 3.18), is also supported by the magnetostatic model. By comparing the model results in Fig. 3.24(d) representing the reversal initiation with Fig. 3.24(f) representing saturation, one realizes that the variation in the demagnetizing fields is much larger in the former case. The predictions from the model are used to fit the experimental results as presented in Fig. 3.18. As for the fit of the coercivity values, the fit of the initialization and saturation fields was achieved by adding a constant field offset to the calculated values. In this case, the shift correlates to the intrinsic broadening of the switching field. The procedure is motivated by the assumption that the *intrinsic* SFD is

identical for the four ensembles, e.g. the last switching islands in every ensemble would intrinsically reverse at the same field (being higher than the coercive field). In the different pattern arrangements, this field is then altered by the stray fields. While the saturation points are well fitted by this procedure, the dependence of initialization field on the fill factor in the experiment is much stronger than in the magnetostatic model. Therefore, the "fit" (dotted line) presented in Fig. 3.18(b) was realized by using the same (negative) offset from the coercive field as fitted for the saturation field. This shift yields a good estimate for the pattern with low fill factor. However, in the case of high fill factors, the measured initialization fields are much lower than predicted by the model. An estimate for the standard deviation of the intrinsic SFD of 0.68 kOe is yielded by the consideration that the interaction vanishes in the limit of a zero fill factor.[1]

In the general case, the field acting on one island is combined out of four contributions:

$$H_{\mathrm{eff}} = H + m_{\mathrm{internal}} H_{\mathrm{internal}} + m_{\mathrm{trench}} H_{\mathrm{trench}} + m_{\mathrm{island}} H_{\mathrm{island}} \,. \tag{3.26}$$

The weights m_k with $-1 \leq m_k \leq 1$ are dependent on the magnetization of the island, the trench material and island ensemble, respectively. On average, they can be assumed to linearly follow the net magnetization of the sub-system, but for a particular island they are determined by the local configuration. In the present experiments m_{trench} mostly equals -1 as the trench material is saturated before the island switching sets in. But for other types of experiments, e.g. MFM imaging in remanence or experiments where the bits are addressed and switched locally, other values are also possible. In a BPM context m_{island} can take any value, as every bit configuration on the medium must be allowed. It is common practice to summarize all contributing demagnetizing fields by an effective demagnetizing factor N_{eff}:

$$H_{\mathrm{eff}} = H - 4\pi N_{\mathrm{eff}} M_{\mathrm{s}} \quad \text{or alternatively} \tag{3.27}$$

$$K_{\mathrm{eff}} = K_{\mathrm{u}} + 2\pi N_{\mathrm{eff}} M_{\mathrm{s}}^2 \,, \tag{3.28}$$

but one has to be aware that N_{eff} is a function of the actual magnetic configuration.

3.5 The switching probability distribution

The hysteresis loops give only information on the *ensemble average* switching behavior, but do not reveal the *individual* properties of the islands, in particular on the repeatability of the switching. The repeatability is important for the question whether the observed

1 Note that the data points were obtained by a 2 % and 98 % threshold to the measured SFDs, respectively. The width (standard deviation) of the intrinsic SFD was calculated from these point assuming a Gaussian distribution.

SFD is only caused by the distribution of intrinsic switching fields within the ensemble and by the inter-islands interaction, or whether each single island treated independently from the ensemble would show a distribution of switching fields when switched several times.

For this analysis, ten independent configurations in a series of field values of $|H_{\mathrm{easy}}| = 3.2\,\mathrm{kOe}$, $|H_{\mathrm{coerc}}| = 4.3\,\mathrm{kOe}$, and $|H_{\mathrm{hard}}| = 5.2\,\mathrm{kOe}$ (indicated by the arrows in Fig. 3.16) were recorded after each time saturating the sample. At the field of H_{easy} the island reversal is initiated corresponding to 6 % to 25 % switched islands depending on the pattern pitch. At the highest field of H_{hard}, the switching is almost completed with 81 % to 90 % switched islands. The configuration at H_{coerc} approximately represents the coercive state with 34 % to 58 % reversed islands. In Fig. 3.25 detailed statistics for every island are presented showing how frequent each island reversed its magnetization at field values of H_{easy} and H_{hard}. For clarity, only the remaining non-switched islands are shown in the case of H_{hard}.

The statistics reveal three different groups of islands which are further summarized in the histograms for the switching probability at H_{easy} and H_{hard} (Fig. 3.26): (i) islands that always did not switch, (ii) islands that occasionally switched, and (iii) islands that always switched. The apparent coexistence of deterministic and non-deterministic processes is explained in a statistical broadening of the islands' individual switching field from the intrinsic value due to thermal activation and due to the local demagnetizing field from the island's environment, which varies with the actual magnetic configuration. When applying a certain external field, this field is either much lower (island group (i)), or much higher than the individual intrinsic switching field (group (iii)), or lies within the statistical broadening of the individual intrinsic switching field resulting in the random behavior of group (ii).

3.5.1 Switching probability in an external magnetic field

The statistical broadening is called either *switching probability distribution (SPD)* [Che10] or *thermally induced SFD* [Eng10] whereby the latter term does not cover fluctuations from the changing magnetic environment. The physical reason for the thermal broadening is found in the influence of an externally applied field to the energy barrier for switching the island magnetization. Under applied field, the energy of a magnetic particle is no longer given by KV as in Eq. 3.1 but changes to [Bea59]:

$$E_{\mathrm{b}}(H) = KV\left(1 - \frac{HM_{\mathrm{s}}}{2K}\right)^2 \tag{3.29}$$

$$= KV\left(1 - \frac{H}{H_{\mathrm{k}}}\right)^2, \tag{3.30}$$

with M_{s} being the saturation magnetization and with defining the anisotropy field $H_{\mathrm{k}} = 2K/M_{\mathrm{s}}$. In order to account for demagnetizing fields, one can either replace K with K_{eff} (Eq. 3.28) [Kro10b] or use the corrected H-field (Eq. 3.27). Here, the latter variant will be

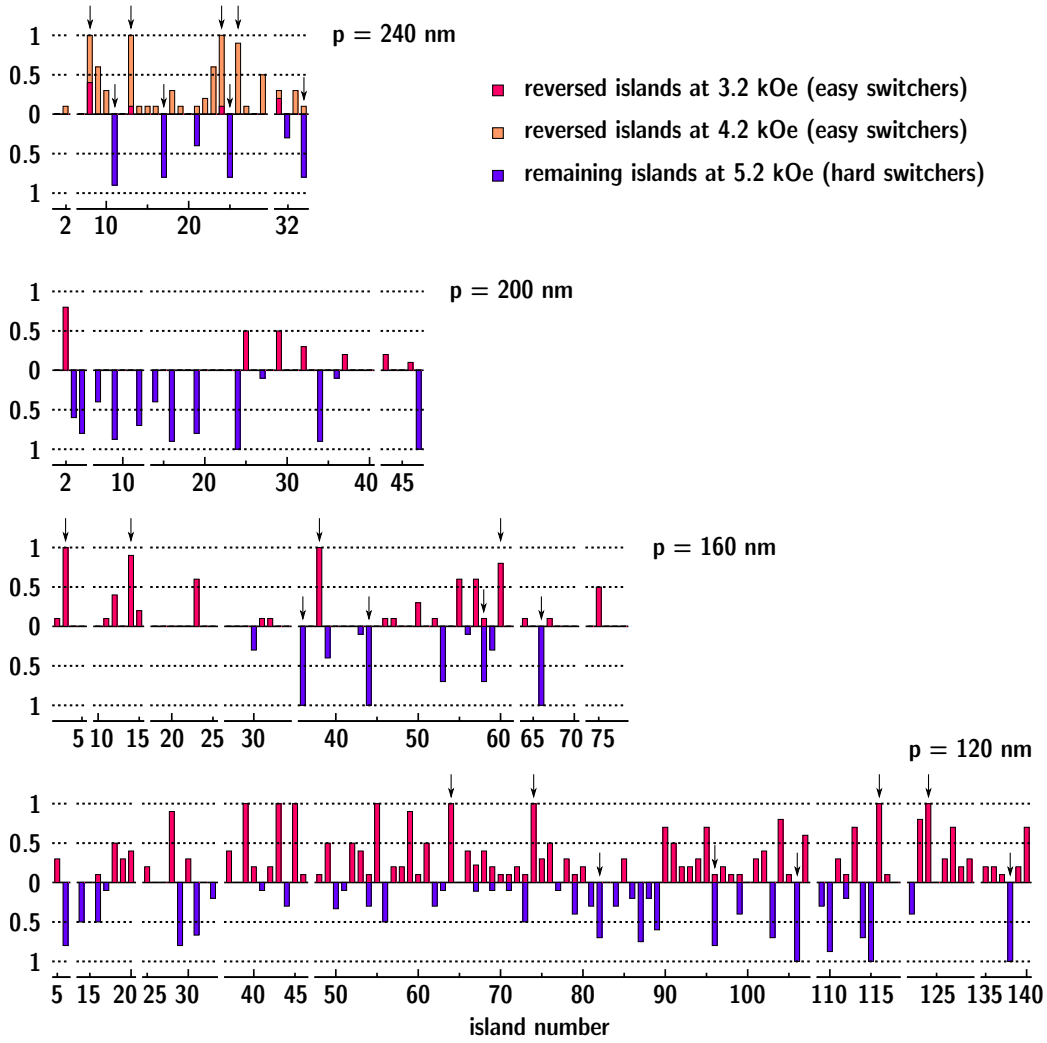

Figure 3.25: Switching probability of each island at fields of 3.2 kOe and 5.2 kOe within ten independent runs. Each plot shows a single ensemble with indicated pitch. As most islands have never switched at 3.2 kOe for the bit pattern with the largest pitch, here also the data for 4.2 kOe is included. On one hand, these plots demonstrate that for many islands the reversal (or non-reversal) at a certain field is not deterministic. On the other hand, this plot was employed to identify islands which have mostly switched at the beginning of the reversal (easy switchers) and islands which have rarely switched when approaching saturation (hard switchers). A few of these particular islands were selected for a detailed TEM analysis (island numbers marked by arrows).

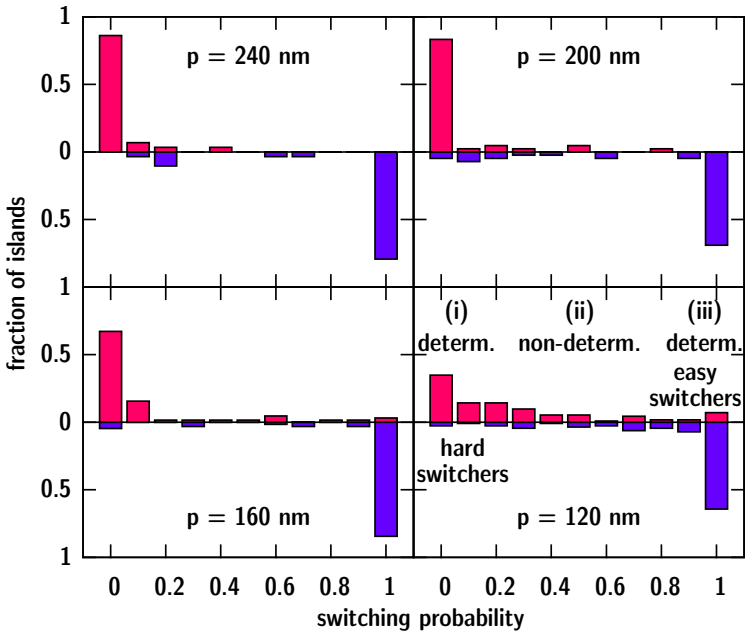

Figure 3.26: Histogram of the switching probability compiled from the data in Fig. 3.25 for each pattern ensemble. The purple bars pointing up correspond to the data taken at 3.2 kOe where most islands have not yet switched. The violet bars pointing down belong to the data at 5.2 kOe approaching saturation. On the left side of the graphs (low switching frequency), the hard switchers are found, while on the right side the easy switcher are located. Both types of islands are indicated by a highly deterministic switching behavior (at these particular fields!). In between, islands with a medium switching probability, i.e. a non-deterministic behavior, are found.

employed and K is identified by K_u.

When the field is swept from zero towards the anisotropy field, the energy barrier will drastically decrease and a switching event may occur due to thermal fluctuation before H_k is reached. In fact, in this scenario both the field with highest switching probability and the mean coercive field will always be smaller than the anisotropy field. The theoretical description of the thermal SFD observed in a repeated measurement by ramping the external field was developed in parallel by A. Garg [Gar95] as well as by L. Gunther and B. Barbara [Gun94]. Both publications are based on the work of Kurkijärvi [Kur72] studying thermal fluctuations in Josephson junctions.

Recalling that the lifetime of the magnetic state of a small particle is given by (Eq. 3.1) [Sha94]:

$$\tau(H) = \tau_0 \exp\left(\frac{E_\mathrm{b}(H)}{k_\mathrm{B}T}\right), \tag{3.31}$$

the probability that the magnetization has *not* switched at fixed field H after a time Δt will be:

$$w(H) = \exp\{-\Delta t/\tau(H)\}\,. \tag{3.32}$$

However, if the field $H(t)$ is ramped up from zero at $t = 0$ at a fixed rate $v = \mathrm{d}H/\mathrm{d}t$, the probability becomes:

$$w(H(t)) = \exp\left\{-\int_0^t \mathrm{d}t'/\tau(H(t'))\right\} \tag{3.33}$$

$$= \exp\left\{-\int_0^H \frac{1}{\mathrm{d}H'/\mathrm{d}t'}\frac{\mathrm{d}H'}{\tau(H')}\right\} \tag{3.34}$$

$$= \exp\left\{-\frac{1}{v}\int_0^H \frac{\mathrm{d}H'}{\tau(H')}\right\}\,. \tag{3.35}$$

The switching probability density that the switching occurs between H and $H + \mathrm{d}H$ is then given by:

$$p(H) = \frac{\mathrm{d}}{\mathrm{d}H}(1 - w(H)) = -\frac{\mathrm{d}}{\mathrm{d}H}w(H) \tag{3.36}$$

$$= \frac{1}{v\,\tau(H)}\exp\left\{-\frac{1}{v}\int_0^H \frac{\mathrm{d}H'}{\tau(H')}\right\} \tag{3.37}$$

$$= \frac{1}{v\tau_0}\exp\left(-\frac{E_\mathrm{b}(H)}{k_\mathrm{B}T}\right)\exp\left\{-\frac{1}{v\tau_0}\int_0^H \exp\left(-\frac{E_\mathrm{b}(H')}{k_\mathrm{B}T}\right)\mathrm{d}H'\right\}\,. \tag{3.38}$$

It shall be noted that this equation can be used for a variety of systems describing switching or escape events where the energy barrier depends on a bias field which is continuously ramped up [Gar95]. In particular, the model is also used for describing switching or depinning of magnetic films by applying a generalized equation for the energy barrier [Sha94]:

$$E_\mathrm{b} = E_0\left(1 - \frac{H}{H_\mathrm{c}^0}\right)^n\,. \tag{3.39}$$

Here, H_c^0 is identified with the coercive field at $T = 0$. The exponent n may vary between 1 and 2—even for single domain particles—depending on the magnetic system. There is an ongoing debate about the underlying models predicting different exponents [Sko06] and even completely different models have been proposed [Mor05].

In Refs. [Eng10; Wer97], Eq. 3.38 was successfully used to model the experimentally obtained thermal SFD of individual small magnetic particles. In contrast to these experiments where the field is swept at a constant rate v, the field in the present imaging experiment is changed in large steps, i.e. the field is increased up to a certain value on time scales of milliseconds and then—during the image acquisition—kept constant for approximately 10^3 s.

In order to account for the discontinuous change in the applied field in the present experiments, the model of Kurkijärvi was modified in this thesis. As already pointed out in Ref. [Wan04], Eq. 3.38 is also derived by the following consideration. If $1 - w(H)$ is the probability that the system overcomes the energy barrier at the magnetic field H, the probability that the system switches its magnetization between H and $H + \mathrm{d}H$ will be the probability for passing the barrier times the probability that the switching has not yet occurred, that is:

$$p(H) = (1 - w(H)) \left[1 - \int_0^H p(H')\,\mathrm{d}H' \right] . \tag{3.40}$$

For the case that the field is increased in a discrete (small) number of steps H_j, the integral can be written as a series:

$$p(H_{j+1}) = (1 - w(H_{j+1})) \left[1 - \sum_{k=0}^{j} p(H_k) \right] , \tag{3.41}$$

where the switching events in between the steps are neglected, since the time for changing the field is at least four orders of magnitude smaller than the following hold time and, thus, will not contribute to the integral.

3.5.2 Analysis of experimental results

In the FTH experiment, the switching probability was determined at three different field values. In addition it is known, that at $H = 0$ the islands have full remanence and at $H = 6.7\,\mathrm{kOe}$ all islands have switched. Therefore, for each island five data points of the cumulative individual switching curve $P(H_j) = \sum_{k=0}^{j} p(H_k)$ are available (Fig. 3.25):

$$P(0\,\mathrm{kOe}) = 0,\ P(3.2\,\mathrm{kOe}),\ P(4.3\,\mathrm{kOe}),\ P(5.2\,\mathrm{kOe}),\ P(6.7\,\mathrm{kOe}) = 1\,. \tag{3.42}$$

These data points were fit with a model function containing only five discrete values following Eq. 3.41. To describe the energy barrier, Eq. 3.29 was employed. In the model, five parameters K_u, M_s, V, T, and Δt are involved. As the saturation magnetization M_s is predominately determined only by the total Co thickness [Eng91], the value of $690\,\mathrm{emu\ cm^{-3}}$ as obtained for the continuous film was taken. In contrast, the uniaxial anisotropy K_u is strongly sensitive on the structure of the material. As the anisotropy

mainly originates from the Co/Pd interfaces, the interface quality largely determines the anisotropy. Due to the deposition of the material on the pre-patterned substrates, the structure and quality of the interfaces has not to be equal to the material grown on a flat substrate. In addition, the anisotropy is influenced by the crystallographic orientation of the grains [Eng91] which may be different for the continuous and the patterned media, but which might be different also for different islands. It has been proposed that the origin of the differences in the islands coercive fields is found in the variation of K_u [Lau08; Sha10; Tho06] which will be discussed in more detail in the next section (Sec. 3.7) revealing the origin of the intrinsic SFD. Consequently, K_u was individually fit for each island.

In the introduction to this chapter in Eq. 3.1, the volume V has been identified with the whole volume of the magnetic island. This attribution is only valid in the case that the island is very small (roughly below 10 nm in thickness and lateral extend) and therefore flips its magnetization by quasi-coherent rotation [Kro10b]. In larger volumes as in the present case, the magnetization reversal is initialized in an activation volume being smaller than the total island volume. Nevertheless, the reversal of this activation volume induces an incoherent reversal of the complete island. In equilibrium, the island will, thus, only appear as a mono-domain volume. Due to the magnetodynamic constraints, the activation volume must not be identified with the grain volume, but a correlation of the grain structure with a certain activation site is very likely. However, a variation of the volume among the islands was not taken into account for the fit procedure. The parameters K_u and V are highly correlated in the fit. It was therefore impossible to fit both parameters individually for each island with only five data points which in addition—although covering the switching distribution of the whole island ensemble—do not accurately resolve the distribution of a *single* island as the field step spacings were too large. The activation volume V was locked to the same value for every island resulting in an ensemble average value for the parameter.

The sample temperature T was not measured during the experiment. As the experiment was carried out under room temperature, a temperature of $(296 \pm 3)\,\mathrm{K}$ has been assumed for the fit. The time interval between two field steps varies between 800 s and 1700 s as the accumulation time of the holograms was always adapted to the current x-ray intensity in order to maintain a constant image quality. The fit procedure was performed with a value of $\Delta t = 1000\,\mathrm{s}$, but a change to $\Delta t = 2000\,\mathrm{s}$ resulted in a deviation of the fitted parameter below 3 % which is even smaller than the fit accuracy.

The fit was performed individually for each pattern ensemble, but simultaneously for all islands in the respective ensemble. The fits for the two samples with the smallest fill factors delivered nearly identical results while all fitted parameters for the third ensemble are systematically shifted by approximately 10 % compared to the former ones (Fig. 3.27). In the case of the sample with the highest fill factor, the fit did not converge.

The fits deliver a reversal volume corresponding to a mean (activation) grain size ($\sqrt{V/(2c)}$) of about 5 nm. This size is similar to what was found in numerical simulations [Kro10b] and this size also corresponds to the physical grain size of the material as observed in high-resolution TEM micrographs from the islands as will be shown in Sec. 3.7 (Fig. 3.33).

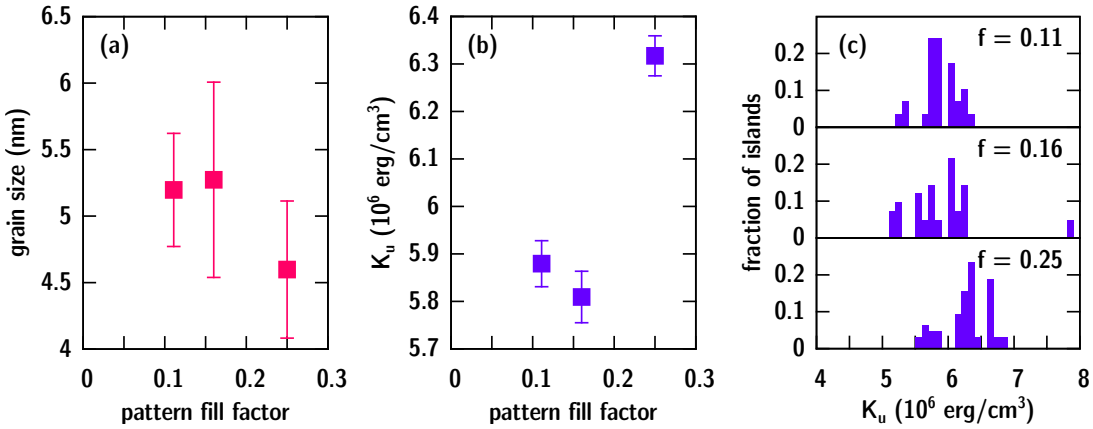

Figure 3.27: Fit results of the switching probability data to the thermal distribution model. For the ensemble with the highest fill factor, a fit was impossible. **(a)** Activation grain size obtained from $\sqrt{V/(2c)}$, **(b)** the mean uniaxial anisotropy, and **(c)** the distribution of anisotropies for each bit ensemble (fill factor indicated).

The fitted values for the mean uniaxial anisotropy reproduce the measurements from the continuous medium. The distributions of the anisotropy have standard deviations of 5 % to 9 %.

The successful fits demonstrate that in the case of only weakly interacting particles the model used is able to describe the observed switching probabilities. This notion includes (i) that the measured SPDs are caused by thermal activation and (ii) that the applied model for the energy barrier is valid. However, as already pointed out in Ref. [Eng10], where the SPD of a single magnetic island was measured much more precisely than in the present work, these kinds of SPD measurements are not able to distinguish between different exponents in Eq. 3.39.

The deviation of the results for the second densest bit pattern (160 nm pitch), but in particular the failing of the fit for the ensemble with the highest fill factor (120 nm pitch) proves the failure of the model in the case of interacting particles. This failure is not surprising as the model explicitly does not include that interaction. It must be concluded that for the densest bit pattern the SPD predominantly originates in the local magnetic environment of the islands which changes from run to run. On the other hand, the fluctuations in the magnetic configuration are initiated by the thermal switching fluctuations themselves. In this sense the inter-island interaction would act as an amplification for the thermal fluctuations.

Unfortunately, it is not easily possible to visualize the fitted distribution curves, since each magnetic island has its individual one and the fitted SPD curves only contain five data points already including the trivial 0 and 1 at the beginning and the end, respectively. Therefore, Fig. 3.28 presents the SPDs gained by employing Eq. 3.38 assuming a continuous field sweep.

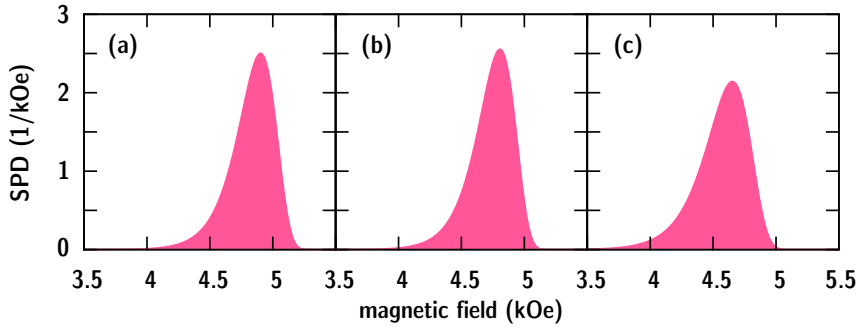

Figure 3.28: Simulated SPDs when assuming a field sweep with a slope of $v = 1\,\mathrm{Oe/s}$. All other values have been taken from the fit results as presented in Fig. 3.27. **(a)** $p = 240\,\mathrm{nm}$, **(b)** $p = 200\,\mathrm{nm}$, and **(c)** $p = 160\,\mathrm{nm}$.

In order to illustrate the fit results as smooth SPD curves, Eq. 3.38 is employed assuming a continuous field sweep. For the calculation, a sweep rate of $v = 1\,\mathrm{Oe/s}$ corresponding approximately to the *mean* field-increase velocity in the experiment was used. The uniaxial anisotropy is set to the mean value of the fitted distribution. The distributions have a σ-width of approximately 0.15 kOe to 0.17 kOe corresponding to a relative width of 3 % to 4 %. The curves additionally show a pronounced asymmetry very similar to what was experimentally observed. This asymmetry is a result of measuring the SFD in a hysteresis loop by first saturating the sample and then ramping up the external magnetic field. The probability for a switching event at low fields is increased simply by the fact that at the beginning of the experiment there are more unreversed islands left than at later stages.

3.6 Spatial correlation analysis

Another way of revealing the inter-island interaction in relation to the intrinsic switching field broadening is to calculate the spatial auto-correlation of the ensemble magnetization state. This procedure uses the spatial information gained in the imaging experiment and may in principle provide information about the presence of an interaction, its sign, strength and length scale. Despite these opportunities and despite the wide usage of MFM imaging in the research on BPMs [Alb09], a correlation analysis of this kind has not yet been published to the knowledge of the author.

The magnetization state auto-correlation is calculated from an $L \times L$ matrix with elements $m_{k,l}$ containing either -1 for a non-reversed island, 1 for a reversed island or 0 for islands outside the FOV. The matrix size L and the number of imaged islands N for every sample with different pitch can be found in Fig. 3.5. The auto-correlation matrix depending on the shift (i, j) is then calculated from the zero-padded matrices (size $2L \times 2L$)

as:

$$C_{i,j} = \frac{1}{N} \sum_{k,l=1}^{L} m_{k,l} m_{k+i,l+j} \qquad -L < i,j < L\,. \tag{3.43}$$

Typically, islands arranged in a square lattice tend to form checkerboard-like patterns with alternating magnetization in both dimensions. This arrangement allows the system to minimize its magnetostatic energy, in particular because no energy has to be invested in forming domain walls as present in continuous magnetic films [Ros01]. In practice, the magnetic state of lowest energy is tried to achieved by a demagnetization procedure where the direction applied magnetic field is alternated while the absolute strength of the field decreases with time. In the correlation matrix, the checkerboard state is characterized by a negative correlation for elements $C_{i,j}$ with odd $i+j$, in particular the nearest neighbor elements $i+j=1$, and positive correlation for elements with even $i+j$, e.g. the next-nearest neighbors with $i+j=2$.

3.6.1 Experimental results

Correlations should be detected at best in the coercive state due to the equipartition of switched and non-switched islands. However, at coercivity the state of lowest energy is usually not reached as the intrinsic properties and random fluctuations cover the magnetic interaction. In the present experiment, images were taken at an external field of $|H_{\mathrm{coerc}}| = 4.26\,\mathrm{kOe}$ as indicated with red arrows in Fig. 3.16. Unfortunately, as already presented in Fig. 3.17, the coercive field depends on the pattern pitch with the result that in the case of $p = 240\,\mathrm{nm}$ and $p = 200\,\mathrm{nm}$ the island majority has not yet switched (34 % and 42 % switched islands, respectively), for $p = 160\,\mathrm{nm}$ coercivity is obtained (52 % switched islands) and in the last case $p = 120\,\mathrm{nm}$ already 58 % of the islands have switched. For this reason, the following analysis and discussion solely focuses on the $p = 160\,\mathrm{nm}$ bit pattern. In order to improve the statistics, in total ten independent configurations were recorded each time after previously saturating the sample.

The averaged auto-correlation map obtained from the FTH experiment is presented in Fig. 3.29 together with a radial plot showing the average correlation of equivalent (i,j) sites (e.g. $(1\,0)$, $(0\,1)$, $(\overline{1}\,0)$, and $(0\,\overline{1})$) in dependence on the absolute shift distance. The zero-shift element, i.e. correlating each element with itself is located in the center and naturally always contains unity. The degree of correlation is encoded in a color scale, where red color denotes positive correlation, i.e. the magnetization is preferentially pointing in the same direction, and blue color denotes anti-correlation with preferred opposite magnetization of two islands. In the radial plots, the color code is used in a different way. Here, red and blue color encode the *expected* sign of the correlation coefficient in the case of an ideal checkerboard pattern.

The correlations—even for the nearest neighbors—are weak and never exceed a value of $|C_{i,j}| \leq 0.20$. The correlation coefficients further decrease for larger distances. The

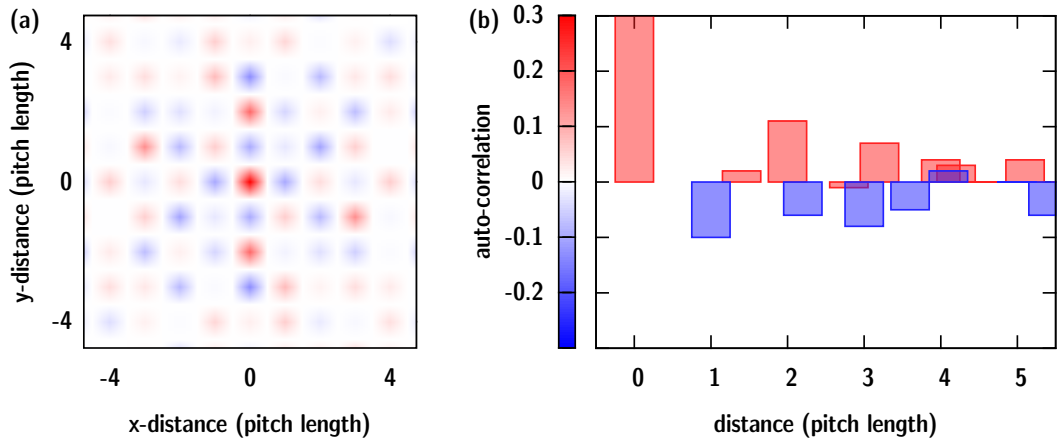

Figure 3.29: Auto-correlation functions for the magnetic bit pattern with 160 nm pitch at remanence. The experimental results were averaged over ten independent measurements. **(a)** A 2D map and **(b)** radial plot of the auto-correlation are shown. The color scale of the 2D map encodes the magnitude of the correlation coefficients $C_{i,j}$ (the scale bar is given in the (b) panel). In the radial plot, the values for equivalent lattice sites have been averaged. Depending on the *expected* sign of the correlation function in a checkerboard pattern arrangement, the bars in the radial plot have different color. Blue encodes expected anti-correlation while red encodes positive correlation.

anti-correlation tendency for the nearest neighbors is clearly present in the system, even the positive correlation is still detected for the sites with $i + j = 2$. For larger distances, systematic correlations only show up as alternating pattern along the $j = 0$ row and the $i = 0$ column. Most of the other $C_{i,j}$ elements seem to fluctuate irregularly. However, the averaged values in the radial plot do show the behavior in sign (correlation vs. anti-correlation) that is expected for a checkerboard pattern, although the actual correlation values are small (below 0.11). A long-range correlation, e.g. indicating a partial exchange coupling of the island material to the trench material, was not detected.

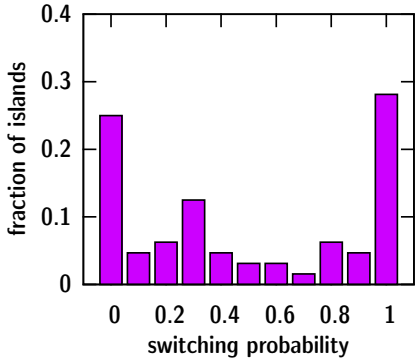

Figure 3.30: Histogram of the switching probability in remanence (at $H = 4.3\,\mathrm{kOe}$) for the bit pattern with 160 nm pitch. A probability of zero refers to islands that have never switched at this field value within ten independent runs, unity refers to island that have always switched. All other islands show a certain degree of non-deterministic behavior.

The strength of the observed checkerboard correlation is a measure for the competition between the distribution of intrinsic switching fields and the island-island interaction. If the intrinsic distribution of switching fields is very narrow compared to the demagnetizing fields from the islands, the island switching will be dominated by the latter and the checkerboard pattern will show up prominently. In the opposite case, when the intrinsic SFD is much wider than the interaction fields, the switching field of each island will be predominantly dictated by its intrinsic value suppressing the inter-island correlations. The width of the intrinsic SFD of the investigated BPM sample has been previously estimated from the experiments with 0.68 kOe (Fig. 3.18), the sample's maximum island-interaction field was determined in the magneto-static model with 0.31 kOe (Fig. 3.24). These properties clearly attribute the investigated bit ensemble to the class of intrinsically dominated island switching. This finding is further supported by the switching probability histogram presented in Fig. 3.30, that has been compiled analogously to the histograms shown in Fig. 3.26. The histogram reveals that more than half of the islands (53 %) behave absolutely deterministic, i.e. they have always or never switched at this particular field value. In other words, the intrinsic switching field of these islands is either too high or too low to be influenced by the island-island interaction. The domination of the intrinsic island properties is the main reason for the low correlation coefficients observed.

3.6.2 Ising simulation

An analytic theory describing the influence of the intrinsic SFD, the inter-island interaction and the thermal switching probability on the correlation results does not exist and is not easy to develop. The experimental results in this work were therefore modeled using a basic Monte-Carlo simulation of an Ising model. The aims of the simulations are (i) to verify whether the observed correlation coefficients fit to the previously determined properties of the sample and (ii) to investigate as how reliable this kind of correlation analysis can be perceived.

In order to match the experimental ensemble arrangement and to minimize boundary effects, the simulation was performed on a 11×11 matrix of Ising spins representing the magnetic state of the islands. The correlation analysis was then performed in an identical FOV as it was defined in the FTH measurements due to the object aperture (Fig. 3.5) with a diameter of 9 pitch lengths. The intrinsic switching field of each element was randomly determined within a Gaussian distribution with a standard deviation of 0.68 kOe as obtained from Fig. 3.18. The island-island interaction is considered only for the nearest neighbors with a demagnetization field per neighboring element of 0.044 kOe as shown in Fig. 3.21. The trench material was not simulated, i.e. it is considered to be saturated all the time providing a constant demagnetization field, that was simply added to the coercive field of the islands. The simulation starts with a completely saturated ensemble of Ising spins at an external field of $H = 0$. The field is then ramped up in steps of 10 Oe up to the ensemble's experimentally observed coercive field of 4.2 kOe (Tab. 3.1). At each field step, the field acting at each island is recalculated from the external field and the

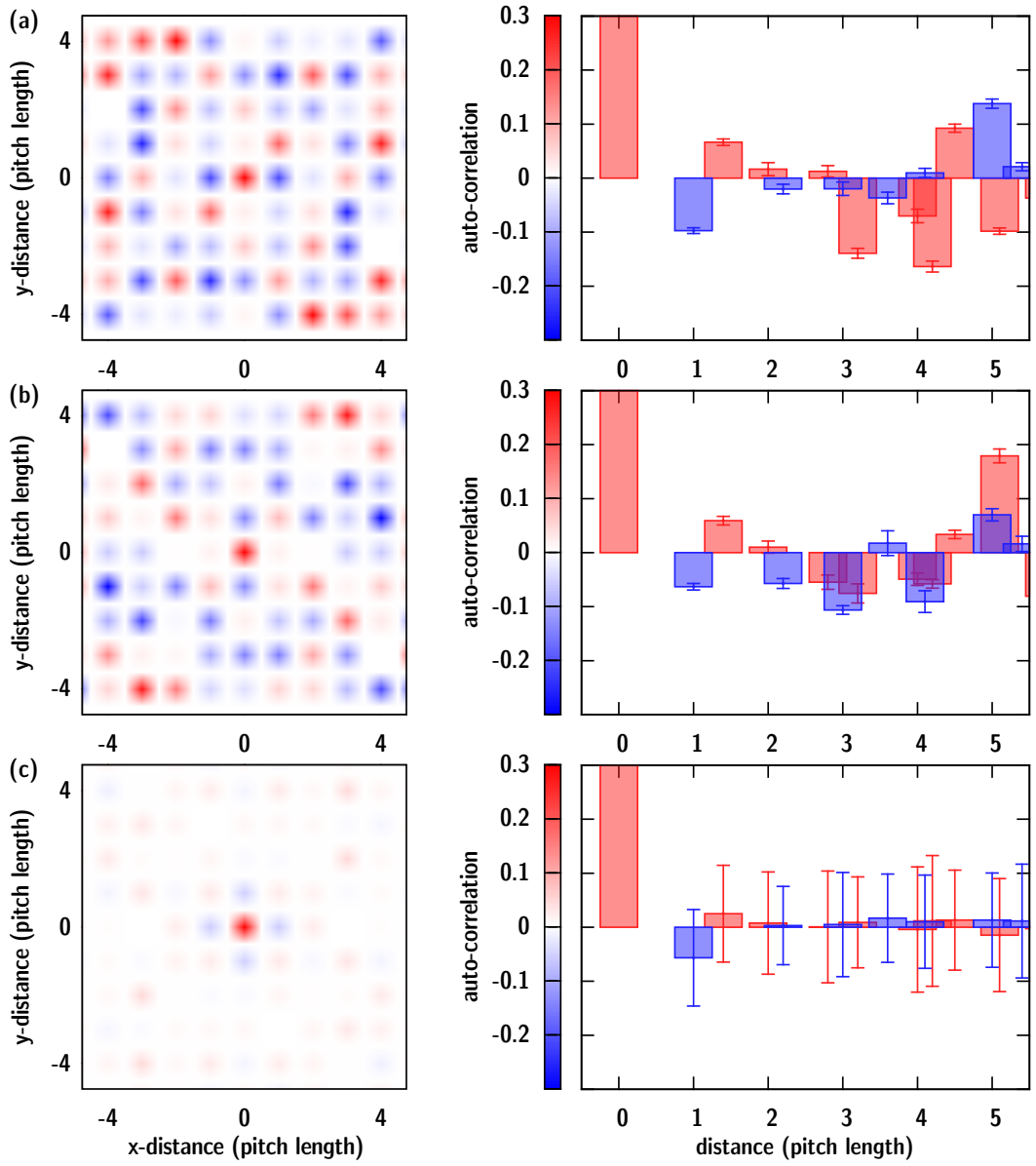

Figure 3.31: Auto-correlation functions retrieved from an Ising simulation of a BPM sample. The parameters in the simulation have been chosen to fit the properties of the ensemble with 160 nm pitch. The results of the auto-correlation analysis are presented analogously to the experimental data in Fig. 3.29. **(a)** Results from Ising simulation using a *single* set of islands with randomly predefined switching fields obeying a Gaussian distribution. The values were averaged over ten runs always keeping the same set. The errorbars indicate the deviations in 200 simulation repeats with again always using the same set of islands. **(b)** The same procedure as (a), but with a different random ensemble. **(c)** Results from an Ising simulation similar as in (a) and (b), but now with a new island ensemble for each of the 200 repeats of the simulation.

demagnetization field of the next neighbors. In addition, the switching field is randomly varied using a Gaussian distribution with a σ-width of 0.17 kOe (Fig. 3.28) in order to simulate the SPD of each individual island. In case the magnetic field at an island exceeds the switching field, the island (spin) switches its sign. After reaching the final external field, the net magnetization, and the auto-correlation for the ensemble were calculated. The mean value of the Gaussian distribution of the intrinsic switching fields was adapted in a way that the net magnetization vanishes at the termination of the simulation at the coercive point. The iteratively obtained value of 4.59 kOe of the mean switching field is in good agreement with the experimental fit result of 4.58 kOe (Fig. 3.17(a)).

By analogy with the experiment, the auto-correlation function was averaged over ten runs. The results were then again averaged over 200 repeats of these ten runs. The error is calculated as the standard deviation among these 200 repeats. Two different simulation schemes were performed: First, the intrinsic switching fields were once determined at the beginning of the simulation and than kept fixed for every repeat. In the second scheme, the random set of intrinsic switching fields was renewed after each repeat of ten runs.

The first scheme can be seen as an example of what can be experimentally expected when using a given ensemble of islands in a fixed FOV. Note that the results as presented in Fig. 3.31(a,b) stem from ensembles that were generated using the experimentally obtained intrinsic SFD, but that are not a reflection of the exact island arrangement of the sample. Hence, a match of the individual $C_{i,j}$ coefficients cannot be expected. Consequentially, the results of the two distinct simulation runs in panel (a) and (b) also differ from each other. Nevertheless, the coefficients show a very similar behavior as experimentally observed. There are coefficients that systematically follow the checkerboard rules, while other coefficients deviate from that rules. The individual magnitudes of the simulated coefficients are higher than experimentally determined. However, in the radial plots of the averaged coefficients this effect already disappears resulting in correlation coefficients of equal magnitude in the experiment and the simulation. The small errorbars in the radial plot indicate that a number of ten runs is sufficient to record the spatial correlation function of the sample with satisfactory precision and that the occurring strong spatial fluctuations are sample intrinsic.

In the second simulation scheme the above results are now averaged over many different island ensembles or, equivalently, different FOVs. This kind of simulation answers the question of how much the results are influenced by the particular selection of a certain FOV, i.e. of how reliable the correlation analysis as performed in the present experiment can be perceived. As the auto-correlation map in Fig. 3.31(c) reveals, nearly all correlation coefficients vanish in the averaging process except for the nearest neighbor coefficients. This finding and the large errorbars indicate that the experimentally observed correlation are only given by the selection of islands in a certain FOV. If one aims to study correlations beyond the nearest neighbor interaction in island arrays dominated by the intrinsic switching field distribution, one has to significantly increase the number of investigated islands, that is one has to increase the FOV.

In conclusion, the simulations confirm that correlation coefficients much higher than

0.1 cannot be expected for the given experimental situation. The simulation further reveals that the observed correlations are dominated by intrinsic switching fields and therefore depend on the particular ensemble selected by the FOV. On average, systematic correlations only show up on the nearest neighbor distance.

3.7 Origin of the intrinsic switching-field distribution [1]

The considerations in the previous sections have revealed that although the inter-island interaction and thermal fluctuations induce an SFD broadening, a substantial contribution to the SFD is caused by an intrinsic variation of the islands' individual coercive fields themselves. The structural origin of this variation is a subject of intense research. Once such an origin would have been identified, one could start to optimize the fabrication process of the media in a way that the distribution of switching field narrows. Conversely, each BPM manufacturing technology brings its own variation of properties among the islands. It is, thus, doubtful whether a single and general origin of the intrinsic SFD exists. Rather, a palette of structural variations always depending on the complete production process of the media will influence the intrinsic switching fields.

It is not aim of this thesis to give a detailed insight into the broad variety of BPM production methods as the manufacturing of the bit pattern was not part of the thesis. There are several review articles available discussing this topic [Alb09; Ros01]. In general, current technologies can be divided into two classes: first, methods using deposition of thin magnetic films on pre-patterned substrates and second, methods working with post-patterning of films deposited on a flat substrate. Of course, each class has its own advantages and disadvantages. When the magnetic film is deposited on a pre-patterned substrate, the properties and the deposition method of the film can be chosen and optimized independently from the patterning process with the drawback that one has to deal with residual material between the islands and that the structural properties of the film material might be adversely influenced by the patterning of the substrate. Conversely, thin-films which are fabricated for post-patterning on flat substrates usually have a much higher quality, but the film and the substrate have to be suitable for the patterning process.

In 2006, the understanding of the switching behavior of patterned media was substantially brought forward by a work of Thomson et al. [Tho06] where the authors made two important findings. First, the reversal mechanism of the islands is always governed by a Stoner-Wohlfarth (SW) behavior. While this is not surprising for very small particles, as this model was developed for such magnetic structures, it turns out that also larger islands that reverse their magnetization by an incoherent rotation, and even islands that show a multi-domain remanence state behave like small SW particles [Dit05; Hu05a]. It is, thus, suggested that the reversal is initiated by a nucleation or activation volume being much

1 The results presented in this section were already published as Ref. [Pfa11]. Parts of the text and some figures in this section were taken from that publication.

smaller than the island. This volume can, but does not have to be a crystallographic grain. The island reversal is then governed by the behavior of the nucleation site. The second finding was, that the distribution of switching fields can be traced back to a distribution of anisotropy [Kro09; Kro10a]. Naturally, this realization again raises the question of the origin of the anisotropy variation. It has been proposed that this variation may be induced by the patterning process itself, in particular by edge roughness [Lau07] and edge damage [Lee11; Sha08]. Other studies have focused on micro-structural effects such as grain structure and orientation [Sha07], the influence of the seed layer [Sha09] and anisotropy defects [Sha10]. The assumption of a distribution of uniaxial anisotropy in the bit ensemble was already used in the previous Sec. 3.5 for explaining the variation of the individual switching behavior. The anisotropy distribution as fitted for the magnetic islands of the present sample can be found in Fig. 3.27.

In a recent study, Lau et al. [Lau08] found that the switching field of an island is determined by the presence or the absence of a so called "trigger" grain inside the island. The trigger grains were identified as crystallographically misaligned grains and the authors suggest that these grains feature an anisotropy lower than the average and therefore act as a nucleation site for the reversal. In the experiment in Ref. [Lau08], the bit pattern was produced by post-patterning of a continuous [Co/Pd] multilayer film via electron-beam lithography. Assuming that misaligned grains are statistically distributed in the thin-film, these grains will also randomly appear among the magnetic islands. Additionally, the position of the defects in the islands will be random as well, e.g., any preference for an edge or central location is not expected.

This situation changes if the BPM is fabricated by deposition on a pre-patterned substrate. Here, the appearance of misaligned grains might be promoted due to the deteriorated growth conditions. Especially at the edges of the substrate pillars, where the substrate orientation becomes undefined, a growth of grains with different orientations is very likely. In order to compare the structural properties of the BPM manufactured on a pre-patterned substrate in the present study with the post-patterned media, the islands were investigated in a very similar manner as in the experiment of Lau and coworkers.

In a first step, islands with a switching field that heavily deviates from the ensemble mean value were identified as the structure–switching field correlations should be strongest in those islands. Islands with a very low switching field are called *easy switchers* while islands with a very high coercivity are called *hard switchers*. In order to identify these islands, it was monitored which islands reverse most of the time first and which islands mostly switch late in ten independent hysteresis runs. The magnetization images were recorded at field values $H_{\mathrm{easy}} = \pm 3.2\,\mathrm{kOe}$ and $H_{\mathrm{hard}} = \pm 5.2\,\mathrm{kOe}$. The data from these runs has already been used in Sec. 3.5. In the statistics of Fig. 3.25, it can be seen how often an island was among that kind of outliers. The most frequent easy and hard switchers (marked by arrows in the figure) were then selected for a further structure investigation with TEM and electron diffraction.

In order to be able to observe misaligned grains, the islands were imaged in a plan-view geometry and the sample had to be thinned to electron transparency. The preparation

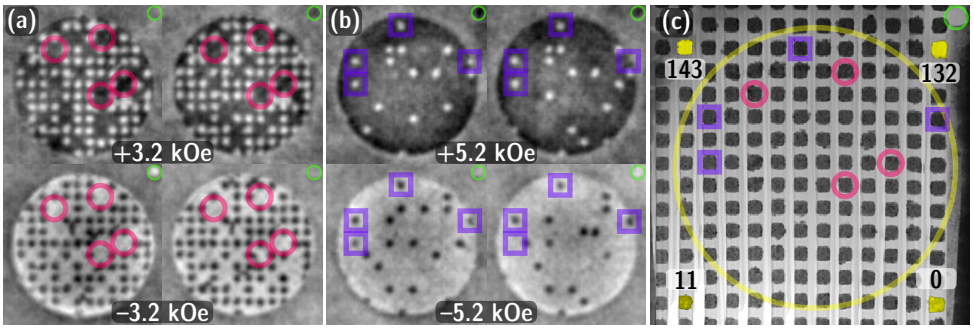

Figure 3.32: Correlating the position of easy and hard switchers in the FTH images and in the TEM study. As an example the BPM sample with 120 nm pitch length is shown. **(a)** Images (four out of ten) taken at the beginning of the reversal to identify easy switchers. **(b)** Images taken just before saturation to find the remaining hard switchers. **(c)** TEM overview image. Using the marker hole (green ring), the positions of the easy and hard switchers were transferred to that overview. The yellow ring marks the position of the FTH object aperture.

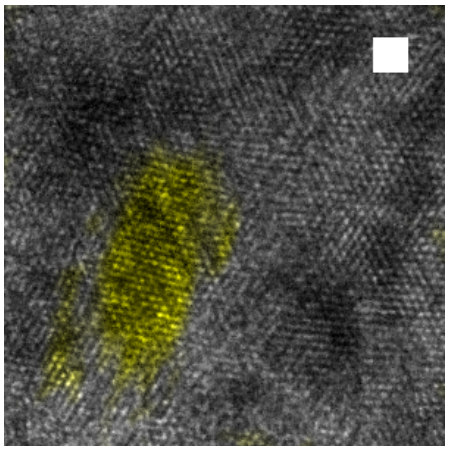

Figure 3.33: Detail of a high-resolution TEM image. The white square corresponds to an area of 1 nm × 1 nm. The image clearly demonstrates the atomic resolution. The semi-transparent yellow overlay marks areas with (2 0 0) lattice spacing.

started with filling the space between the islands with electron-beam deposited Si-oxide. Following removal of a sample section generated via FIB, the sample was thinned down by milling from the substrate side of the islands, leaving only islands and filler material in the final thin section. With the help of the marker hole next to the FOV aperture it was then possible to locate the islands, which were previously selected from the FTH measurements, in the TEM overview image (Fig. 3.32(c)). The inspection of the selected islands was then performed in a high-resolution TEM mode being able to resolve the atomic structure of the magnetic material as demonstrated in Fig. 3.33 showing a 12.3 nm × 12.3 nm detail of the whole island (edge length 80 nm). The size of the images showing the whole island was 2048 × 2048 pixels.

Due to the outstanding TEM image quality, it is possible to not only identify the

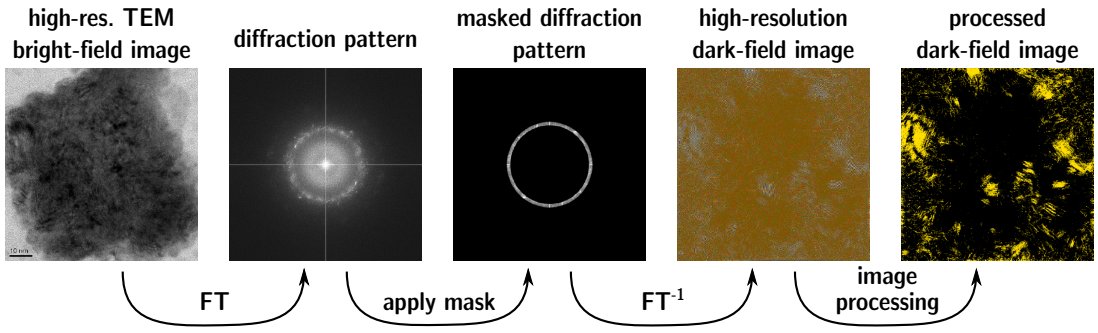

Figure 3.34: TEM image processing workflow.

crystallographic grains, but to even use the images as input data for the diffraction analysis. In detail, the images have been processed in the following way (Fig. 3.34): First, the high-resolution TEM images were Fourier-transformed gaining the diffraction pattern of a single island. Then, the diffraction pattern was masked removing all information outside of the range between 0.185 nm and 0.200 nm corresponding real space distances. This range relates to the (2 0 0) lattice spacing as the average (2 0 0) lattice spacing in the TEM analysis was determined as 0.191 nm. Subsequently generated inverse Fourier transforms only show the island regions containing in-plane (2 0 0) lattice spacings. The regions or grains with in-plane [1 0 0] orientation are significantly misaligned from the preferred face-centered cubic (FCC) [1 1 1] out-of-plane crystal orientation as illustrated in Fig. 3.4. Since the crystal orientation is the second source of perpendicular anisotropy [Eng91] which is highest for the [1 1 1] orientation, the selected regions will feature a reduced anisotropy. In a last step, the images were processed in such a way that the misaligned regions become clearly visible. In particular, the image was smoothed with a Gaussian kernel and the contrast and color scale were optimized equally for each image. The resulting image is called the *dark-field image* of the island.

Images of all islands that were investigated in the TEM analysis are presented in Figs. 3.35 and 3.36. Four easy and four hard switchers were selected from each ensemble. Unfortunately, the FIB chip of pattern 2 broke during the preparation. In total, 12 easy and 12 hard switching island were analyzed.

In agreement with Ref. [Lau08], regions with (2 0 0) reflections were found in every easy switcher. However, more than 50 % of the hard switcher also contain such grains. But in contrast to the easy switchers, those grains are always located *at the edges* of the islands. Obviously, the peripheral misaligned grains do not always act as trigger grains. A statistics of these observation is presented in Fig. 3.37. There is only one island classified as hard switcher that contains a misaligned grain in its central part—namely island 34 from pattern 1. However, on one hand, that misaligned grain is small compared to grains in easy switchers, and on the other hand, within the ten repeated hysteresis loops for identifying these outliers, the island 34 was once among the first switching islands which

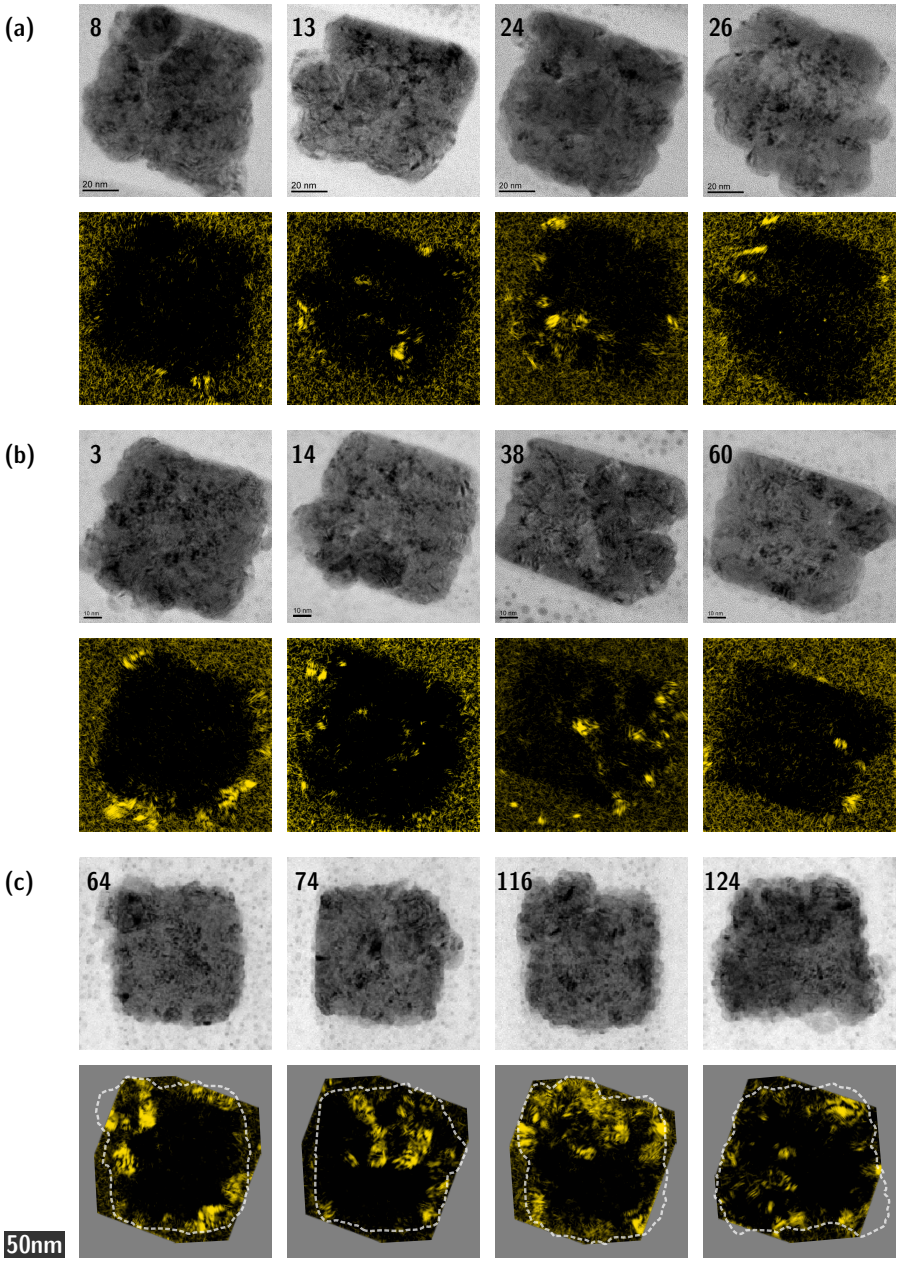

Figure 3.35: Bright-field (top rows) and dark-field (bottom rows) images of easy switchers investigated in the TEM analysis. **(a)** Islands from pattern 1 with 240 nm pitch, **(b)** islands from pattern 3 with 160 nm pitch, and **(c)** islands from pattern 4 with 120 nm pitch. The yellow regions in the dark-field images of the islands indicate reflections from (2 0 0) lattice spacings. The dark-field images of pattern 4 were produced from images that have a better resolution, but smaller FOV compared to presented bright-field images. For this reason, the contour of the island is additionally drawn as dashed line.

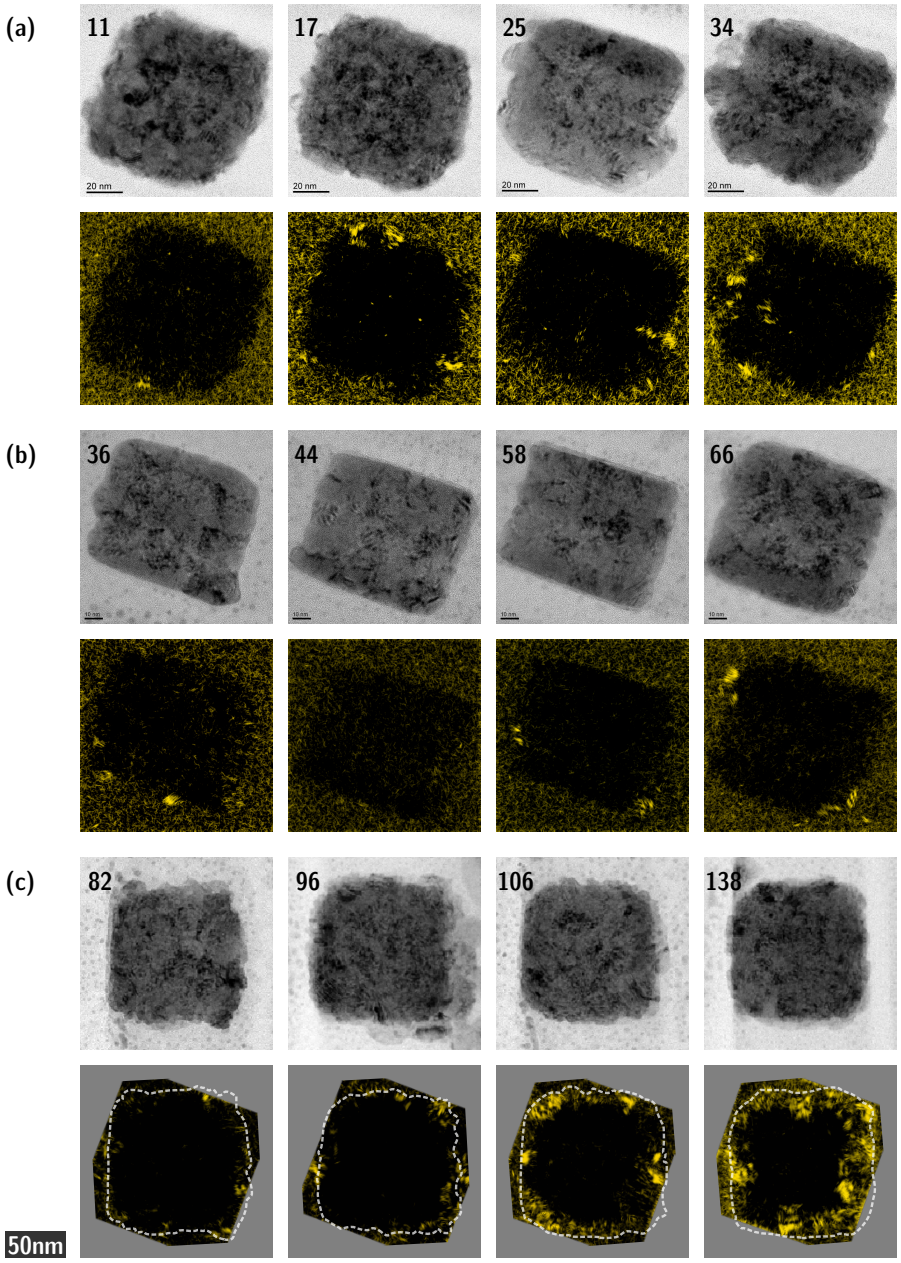

Figure 3.36: Continuation of Fig. 3.35. Bright-field (top rows) and dark-field (bottom rows) images of all hard switchers investigated in the TEM analysis. **(a)** Islands from pattern 1 with 240 nm pitch, **(b)** islands from pattern 3 with 160 nm pitch, and **(c)** islands from pattern 4 with 120 nm pitch.

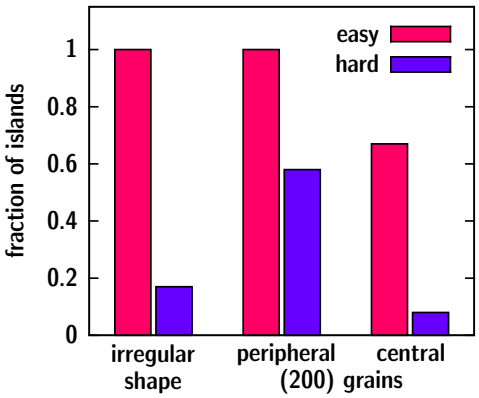

Figure 3.37: Statistical analysis of the TEM observation showing how frequent the islands exhibit (i) a shape deviating from a square as promoted by the substrate, (ii) misaligned grains in the island's center, and (iii) misaligned grains at the periphery of the island. Misaligned grains are identified by showing a (2 0 0) reflection in the electron diffraction spectra. The statistics are compiled separately for easy and hard switching islands.

may be an indication of the grain acting. In addition to the occurrence of misaligned grains, it was also discovered that the shape of the easy switcher islands is always irregular, i.e. deviating from quadratic shape as supported by the patterned substrates, whereas the hard switchers predominantly follow the shape of the substrate pillars. Consequentially, there is an indication that the irregular island shape is correlated with the presence of misaligned grains. This finding is not surprising as a disordered growth will favor various grain alignments and vice versa.

The observed insensitivity of the island reversal to misaligned grains located at the periphery of the island can be understood using the results from the magnetostatic calculations in Sec. 3.4.2. Looking again at Fig. 3.24 showing the demagnetizing field inside an island, one realizes that the field is much weaker at the edges of the island. As a result, the effective anisotropy $K_{\mathrm{eff}} = K_{\mathrm{u}} - \frac{1}{2} H_{\mathrm{demag}} M_{\mathrm{s}}$ at the edges is much larger than in the island's center. The difference between both positions is as large as approximately $1.3 \times 10^6\,\mathrm{erg\ cm^{-3}}$. Even if the anisotropy of an edge grain is reduced due to a crystallographic misalignment the *effective* anisotropy might be still higher than in the center of the island with the result that the grain will not act as a nucleation site for the reversal.

The experimental findings are in agreement with micro-magnetic simulations where the switching field of an island depending on the position of a "magnetic defect" in the island was determined [Sha10]. The defect was simulated by a reduced or tilted anisotropy. It was found that in some cases—depending on the tilt of the anisotropy—the switching field even increases if the defect is located at the edge of the island.

3.8 Summary

Bit-patterned media (BPM) are a leading candidate for the next-generation magnetic data storage in order to keep up with the increasing demand for higher storage capacities. The technology relies on storing the information in the magnetization of isolated (exchange decoupled) areas of a thin-film material arranged in a 2D lattice. A major challenge of this technology lies in the variation of the magnetic islands' switching field—called the switching field distribution (SFD). In order to be able to reliably write a bit without influencing neighboring islands the SFD has to be sufficiently narrow. In the presented study, a specially designed prototype BPM sample was used to investigate (i) the influence of the stray-field interaction in an array of islands on the SFD, (ii) the SFD due to thermal fluctuations, and (iii) the structural origin for the bit-to-bit intrinsic variation of the switching field. The switching behavior of the islands was investigated by imaging the magnetic state of the islands in an ensemble using soft x-ray Fourier transform holography (FTH). The method allows for a few particular opportunities which distinguish this study from previous surveys:

1. The holography imaging method allows to investigate several samples at the same time and with a spatial separation of less than 35 µm in our case (object multiplexing). The sample in this study contained four areas with different BPM ensembles. As the stray-field interaction is strongly dependent on the island-to-island distance (pitch), this parameter was systematically varied among the four ensembles in a way that the four patterns represent the crossover from an intrinsically dominated SFD to an interaction dominated SFD. All other experimental parameters as the substrate, the patterning method, the size of the islands, the magnetic multilayer coating, the magnetic history and the experimental environment (e.g. magnetic field, temperature) during the measurements were exactly identical for all BPM ensembles.

2. As x-ray FTH imaging relies on the photon-in–photon-out principle the measurements can be performed in applied field and an influence of the probe on the magnetization of the islands is entirely excluded.

3. Due to the direct imaging of the islands, the individual switching behavior, in particular the individual switching probability, can be analyzed. This is in contrast to ensemble measurements, e.g. via the total magnetization.

4. Furthermore, the imaging approach makes it possible to identify and locate islands with particularly low or high switching fields. In this study such outliers could thus be selected for a further structural analysis using high-resolution transmission electron microscopy.

In order to study the island interaction, island switching hysteresis loops were compiled from the magnetization state images of the sample in applied field. From a fit of the loops, the coercivity (mean switching field) of the ensemble, the width of the SFD and

its asymmetry were obtained. The experimental observations were compared with a magnetostatic model that was developed for the investigated system. The model considers the demagnetizing fields from the magnetized volume, the island ensemble and the trench material in between the islands. In addition, spatial correlations in the magnetic state imaged at remanence were analyzed and compared with an Ising simulation of the system. The following results have been obtained:

1. The coercive fields of the ensembles lie between 4.0 kOe to 4.6 kOe and increase with higher pattern pitch. This change could be explained with the influence from the magnetically saturated trench material. Note, that the saturation of the material is a result of the applied field during the measurement. In a remanent measurement (e.g. when using MFM), the trench material would decay into domains and the coercive field would stay unaffected. One could speculate that in this case, the different local magnetic environments of the islands lead to an additional broadening of the SFD.

2. As expected, the width of the SFD heavily depends on the bit-to-bit spacing. The σ-width for the ensemble with the smallest distances (120 nm) of 1.25 kOe is twice as high as for the largest pitch (240 nm). The change is larger than calculated from the magnetostatic model. A phenomenological fit to the data delivered an intrinsic SFD width of 0.78 kOe.

3. The SFDs show a certain asymmetry. The asymmetry increases for smaller pitch sizes. As for the ensembles with the largest pitch sizes, i.e. the ensembles with only weakly interacting islands, the asymmetry nearly vanishes, it is very unlikely that the asymmetry is mainly caused by the intrinsic properties of the islands. On the other hand, an asymmetry is also not predicted from the magnetostatic interactions.

4. To further analyze the observed asymmetry, the field values where the island reversal sets in and the field where all islands have switched were determined. In agreement with the model, it turned out that the saturation field only marginally changes with the pattern pitch. However, although already the model predicts a strong dependence of the initialization field on the pitch, the dependence in the experiment even exceeded the prediction. From this analysis, another estimate for the intrinsic SFD width of 0.68 kOe was obtained. Most probably, the difference between the experimental observation and the model is explained by the fact, that the trench material has not completely reversed its magnetization due pinning effects at the substrate pillars acting as defects in the magnetic film (Fig. 3.13). This pinning increases with higher fill factors. As a result, the stray field from the trench material stabilizing the magnetization of the unswitched islands is reduced and the islands tend to reverse at lower fields.

5. The correlation analysis showed only weak correlation coefficients of the switching behavior. The checkerboard correlation, indicating the lowest energy state, vanishes

at longer distances than the nearest and next-nearest neighbors. It is obvious that the intrinsic properties of the islands still mask the inter-island correlations.

The next step of the study was to examine the individual switching behavior of each island, in particular the repeatability of the reversal. For this task, the islands were imaged in ten independent, but identical hysteresis runs. It was shown:

1. Each individual island exhibits a certain broadening of its switching field, i.e. from run to run it switches at different field values.

2. The behavior was explained with thermal fluctuations at the vicinity of the switching field. An adapted model describing switching (or escape) events with an energy barrier depending on a ramped bias field was developed and used to analyze the experimental data.

3. In the case of the BPM ensembles with large pitch, the model was able to describe the experimental results supporting the assumption of thermal fluctuations. The resulting switching probability distributions have a σ-width of approximately 0.16 kOe. For the ensemble with the highest bit density, the model was failing. It is suggested that the changing local magnetic environment of an island is an additional source for the fluctuations.

4. A distribution of anisotropies among the islands was extracted from the fit of the model with the experimental data. The mean anisotropy exactly reproduced the value obtained for the continuous film of 5.7 erg/cm^3; the σ-width of the distribution was on the order of 0.4 erg/cm^3.

5. The obtained switching probability distributions show a pronounced asymmetry that is very similar to what was observed for the complete reversal loop of the ensemble. It was thus proposed that the SFD asymmetry may have its origin in the method of measuring the SFD in a ramped hysteresis loop and that the stray-field interaction may act as an amplification of the thermal fluctuations.

The aim of the last part of the study was the search for a structural origin of the intrinsic SFD. The structural analysis was performed using high-resolution TEM of single islands in plane-view geometry. The study focused on the detection of grains that are misaligned from the preferred FCC [1 1 1] out-of-plane direction as these grains presumably act as trigger grains for the reversal process. The islands that were selected for the analysis were previously identified as islands with a particularly low switching field (easy switchers) or islands with a particularly high switching field (hard switchers). The following observations and conclusions have been made:

1. Every easy switching island contains a misaligned grain, but there is also a substantial number of hard switchers that have such a grain. The structural difference was found in the fact that inside an easy switcher the misaligned grain is often located in

the central part of island while in the case of a hard switcher the misaligned grains are always found at the periphery.

2. The frequent appearance of misaligned grains at the island's periphery can be explained with the undefined growths conditions at the edges of the substrate pillars with the result that the preferred FCC [1 1 1] out-of-plane orientation is no longer promoted.

3. An explanation for the reduced impact of misaligned grains at the edges is again found in the demagnetizing fields acting inside the island. It was shown that these fields are much lower in the outer regions of the islands, leading to the conclusion that it is more likely that the reversal will be initiated in the center of the the island. A low anisotropy area—such as misaligned grains—in the center of the island will have more impact than at the periphery.

The experimental data (i.e. the images) recorded, the subsequent data analysis and the proposed models were able to reveal the switching of individual islands and to widely explain the observed behavior. Nevertheless, there is room for improvements and further investigation on both the experimental and the theoretical side of the study. Experimentally, it is suggested:

1. The limits in the imaging capabilities of FTH were not reached in the design of the sample. The full reconstruction matrix is widely unused and the images show a very strong contrast, i.e. the sensitivity limit was by far unreached. A second generation of BPM produced for FTH imaging may possibly feature (i) a larger FOV with more islands imaged and, thus, providing better statistics, (ii) one or two more independent island ensembles, (iii) smaller and therefore more application-oriented islands, as well as (iv) a smaller number of repeats in the magnetic multilayer.

2. A change of the multilayer composition towards more realistic BPM samples will certainly result in higher switching fields of the islands. The experimental setup has to account for these fields by using a more sophisticated electromagnet or even super-conducting magnet coils.

3. In the present study, the resolution of the imaging system was sufficient to clearly distinguish islands with a trench spacing of 40 nm. While an improvement by another 10 nm seems to be feasible with the present FTH imaging approach, reaching the 10 nm spatial resolution barrier will only be possible by using more elaborate reference structures [Gei13; Mar08; Zhu10] and by using even more intense x-ray sources.

On the model side of study, the following questions may be addressed:

1. The experimentally observed SFDs are broader than expected from the obtained intrinsic SFD together with the calculated interaction broadening. In particular, the first islands switch at much lower fields than predicted by the magnetostatic model.

As already pointed out, the reason could lie in influence from the incompletely reversed trench material.

2. The above mentioned observation also results in a pronounced asymmetry of the SFD. The origin of the asymmetry could not be entirely identified in the present study.

3. In Sec. 3.5, it was not possible to explain the observed SPD of the most dense packed BPM sample with the proposed thermal model. This unsuitability was traced back to the influence of the magnetostatic interaction between the islands via a locally changing magnetic environment. Up to now, the magnetostatic interaction was always treated in relation with the ensemble-average SFD. It could be fruitful to also find a description from the viewpoint of a single island and the broadening of its individual switching field and to merge this effect with the thermal broadening.

An even further outlook to application of FTH imaging in the research of BPM and other fields of magnetic research will be given in the next chapter.

4 Perspectives of Fourier-transform holography for magnetic imaging

In this thesis it has been shown that Fourier-transform holography (FTH) is a very powerful tool for imaging magnetic structures on a nanometer scale. However, other imaging methods exist which also provide magnetic contrast. Comprehensive overviews about this topic can be found in the books [Hub98] and [Bea06]. As all x-ray magnetic imaging methods, FTH imaging relies on the x-ray magnetic circular dichroism (XMCD) effect requiring photon sources with variable wavelength, polarization control and high photon flux. Up to now, these requirements can only be fulfilled at third generation synchrotrons and x-ray free-electron lasers. Compared to laboratory imaging instruments, such as magnetic force microscopy (MFM)s, transmission electron microscopy (TEM)s or scanning electron microscopy (SEM)s, the access to these sources is very restricted and their operation is very expensive. Consequentially, a magnetic imaging study will always be performed using laboratory methods if possible. Nevertheless, there is a substantial number of features provided by the x-ray methods or even solely by FTH that will provide unique insights to the question studied and justify the additional effort.

In this last chapter of the thesis, the perspectives of FTH in the field of magnetic imaging shall be addressed in the form of presenting experimental surveys which the author of this thesis was involved in and which witness the capabilities of FTH.

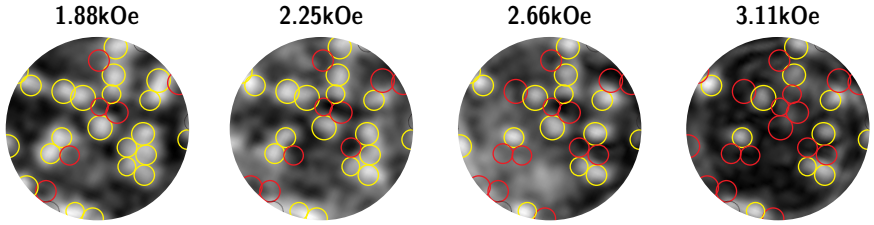

Figure 4.1: Images of magnetically capped nanospheres obtained via FTH at external magnetic fields as indicated. The gray-scale encodes purely magnetic contrast. The position of the nanospheres is marked by circles (red indicates caps that have switched while yellow marks unswitched caps) that were obtained from SEM images of the sample. The circular FOV is 590 nm in diameter. Images were reproduced from Ref. [Gü10].

Microscopic reversal behavior of magnetically capped nanospheres

In this study [Gü10], the magnetic switching behavior of nanospheres capped by a Co/Pd multilayer was investigated. Similarly to the patterned sample presented in Chap. 3 of this thesis, the nanocaps form magnetic islands. The magnetic state of the islands was imaged by FTH under applied field in order to record the individual switching field of each nanocap (Fig. 4.1). In particular, the study focused on the dependence of the switching field on the size of the nanosphere, the local arrangement of the spheres and on the tilt angle of the externally applied magnetic field.

Methodically, the study demonstrated the high sensitivity of the x-ray magnetic imaging method on one hand as the multilayer contained a total height of only 2.4 nm of cobalt. On the other hand, the experiment is another example of the environmental flexibility of FTH allowing to even tilt the applied magnetic field by the rotation of an electromagnet around the sample. In terms of maximum field strength, the only limitation is set by the capabilities of the electromagnet, but not by the method itself due to the photon-in–photon-out principle of the underlaying interaction. In the opinion of the author, FTH is the most promising method for magnetic imaging under very high magnetic fields in the Tesla-regime.

Direct observation of field and temperature induced domain replication in dipolar-coupled perpendicular anisotropy films

The study of Hauet and coworkers [Gü12; Hau08] combines a multitude of experimental advantages of the FTH method. In order to directly image the duplication of a domain pattern from one magnetic layer into another, only dipolar coupled layer, a sample consisting of a hard-magnetic Co/Pd multilayer and soft-magnetic CoNi/Pd multilayer separated by a thick (10 nm) Pd layer was produced. Employing the high penetration depth of x-rays and the element selectivity of the XMCD effect, the magnetization of each layer was imaged separately by recording holograms at the Co and Ni L_3-edges. The

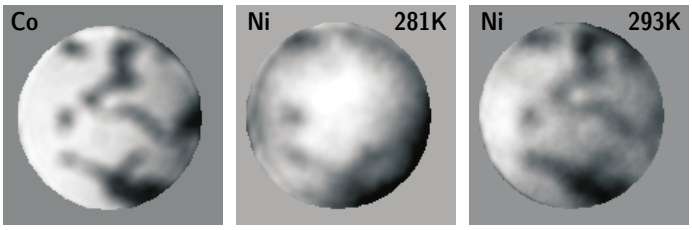

Figure 4.2: Temperature induced domain replication from a hard magnetic layer (imaged at the Co-edge) into a soft layer (imaged at the Ni-edge). While at a temperature of 281 K the domain pattern is already partially duplicated into the soft layer, the soft layer fully resembles the configuration at 293 K. The circular FOV has a diameter 1.2 µm. Images were taken from Ref. [Gü12].

replication of the domain pattern from the hard into the soft layer was then induced either by heating the sample towards the Curie temperature of the CoNi/Pd layer or by driving minor magnetic hysteresis loops of the soft layer only while maintaining the state of the hard layer. The external field was again applied using an electromagnet. In Fig. 4.2 the stepwise duplication of the domain pattern from the hard magnetic layer (imaged at the Co-edge) into the initially saturated, soft magnetic layer (imaged at the Ni-edge) is shown in the process of approaching the Curie temperature close to 350 K. Note that the Ni thickness in the multilayer added up to only 4.2 nm compared to a total thickness of the whole sample system of 87 nm.

The temperature of the sample was varied during the experiment within a range of 100 K. Although cryostatic sample stages are available also for other imaging instruments, they are particularly easily implemented in an FTH setup. In addition, the FTH experiment is insensitive against drift on a nanometer or even micrometer scale that is very difficult to avoid during temperature changes of such a magnitude. The integrated sample design guarantees that always the same sample region is imaged.

Femtosecond single-shot imaging of nanoscale ferromagnetic order in Co/Pd multilayers using resonant x-ray holography

X-ray free-electron laser (FEL) sources deliver ultra-bright x-ray pulses with durations of 100 fs. As ultra-fast magnetic processes such as ultra-fast demagnetization proceed on a femtosecond timescale [Pfa12], these sources fuel the hope of being able to image such processes in real space. Due to the high coherence of the emitted x-ray radiation, coherent and lensless imaging methods such as FTH are particularly suited for being employed at FELs. Unfortunately, most existing and most projected sources deliver or will deliver only linearly polarized light. It was proposed by the author of this thesis to employ simple absorption filters based on the XMCD effect to produce partially circularly polarized light at FELs in order to promote imaging with XMCD contrast at these sources [Pfa10b]. Based on this concept, it was possible to record the first femtosecond single-shot images of magnetic domains with 100 nm width as presented in Fig. 4.3 [Wan12]. The experiment was carried out at the Linac Coherent Light Source (LCLS) in Stanford, USA. Although these images show a static sample, the experiment marks an important milestone on the path to image

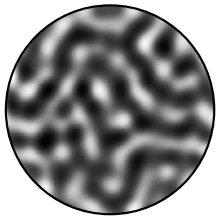

Figure 4.3: Image of a Co/Pd multilayer sample exhibiting a magnetic labyrinth domain pattern recorded with a single x-ray pulse with 80 fs duration. The image was retrieved from the sum of 15 individual images obtained by reference multiplexing. The FOV is 1.45 µm in diameter. Taken from Ref. [Wan12].

magnetization dynamics on the femtosecond timescale.

Sequential femtosecond x-ray imaging

In the previous experiment the possibility of recording a magnetic *still* image by a single femtosecond x-ray pulse was demonstrated. However, a femtosecond time-lapse *movie* showing the dynamics of a sample requires a sequence of images taken with controllable time delay. Due to the fundamental readout time limitations of two-dimensional area detectors, it is impossible to separately record two images with a time delay in the femtosecond regime. However, the holographic imaging approach as presented in Ref. [Gü11] is capable of recording two fully independent images by superimposing two subsequent x-ray holograms of a sample within one detector exposure. First, a single x-ray pulse is split into two pulses that travel along different paths guided by x-ray mirrors. By changing the path length for one of the pulses a certain time delay is introduced between the two pulses. The two pulses are then recombined on the sample in a way that the two spots partially overlap. In the overlap region the sample is positioned which is surrounded by multiple reference apertures. As some references are only illuminated by one of the two pulses, the reconstruction contains independent images that can be unambiguously addressed to one of the two pulses and therefore represent the sample at two different points in time [Gü12; Gü11].

In this pilot experiment carried out at the Free-electron Laser in Hamburg (FLASH), a pure absorption sample without any magnetic contrast was used. The reconstruction of that sample at two different times with a delay of 50 fs is presented in Fig. 4.3. The sequential imaging approach is not methodically limited for being applied to magnetic

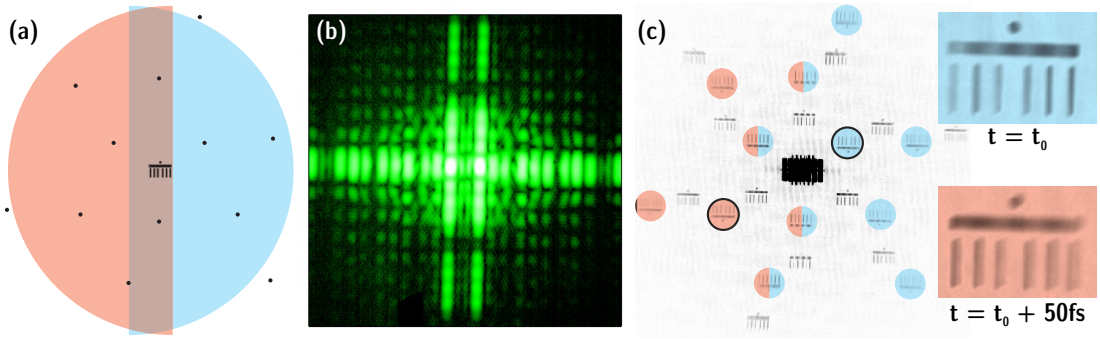

Figure 4.4: Sequential femtosecond x-ray imaging. **(a)** Schematics of the sample and its illumination. The test sample is represented by the Brandenburg Gate in the center surrounded by multiple reference apertures. The red and the blue areas show the illumination spots of the two split and delayed beams on the sample. **(b)** Superimposed holograms on the CCD detector. **(c)** Reconstruction of the hologram shown in (b). The color overlay denotes the assignment of the image to one of the two beams. The insets show two enlarged images. Taken from Ref. [Gü11].

samples as well.

Apart from the presented approach, there are other proposals for employing the properties of holographic imaging for realizing time-resolved experiments in the femtosecond regime. In Refs. [Pfa10a; Sch07c] it is proposed to exploit the capabilities of FTH of imaging multiple objects simultaneously. If these objects are properly arranged in space a time delay between the moments when the objects are hit by the x-ray pulse can be realized. Another approach is presented in Ref. [Cha07] using a modified in-line holography setup.

Finally, FTH imaging is fully compatible with measurements using a pump-probe scheme either in a single-shot or integrating mode. In Ref. [Pfa12] pump-probe measurements at FLASH have been carried out in the femtosecond regime using the small-angle x-ray scattering (SAXS) signal of a magnetic multilayer sample exhibiting a labyrinth domain pattern. The setup used in this experiment could be easily transfered to a holography setup by simply replacing the sample by an integrated FTH sample arrangement as presented in Sec. 3.2.1. Another very recent experiment was carried out at the synchrotron source BESSY II and operates in the picosecond regime [Bü13a; Bü13b]. In this FTH experiment, the motion of a magnetic bubble domain was monitored with 3 nm spatial resolution after excitement by a magnetic field pulse.

Summary

Based on the presented experiments, three cases of application in the field of magnetic imaging can be identified where FTH offers unique features: first, measurements with special environmental requirements, in particular high magnetic fields and/or low or elevated temperatures; second, imaging of buried layers with element contrast; third, time-resolved measurements in the picosecond to femtosecond regime.

In the research and development of magnetic data storage technologies which Chap. 3 of this thesis was part of, all three application cases for FTH can play an important role. The possibility of studying samples in high magnetic fields and under elevated temperatures will help to understand the switching of magnetic bits in bit-patterned media (BPM) and heat-assisted magnetic recording (HAMR) applications. Imaging the magnetization in buried layers is essential in the survey of exchange coupled composite (ECC) structures where the bit reversal is assisted by an additional layer [Hau09]. Finally, time-resolved methods will provide a more fundamental understanding of the magnetic switching mechanisms and will possibly help to improve the write processes.

Under a more fundamental point of view, the unique feasibility given by FTH magnetic imaging of studying magnetization phenomena simultaneously with nanometer spatial resolution and with picosecond to femtosecond temporal resolution will have a huge impact in the future research of magnetic phenomena. On one hand, magnetic phenomena are intrinsically acting on these length and time scales. On the other hand, the instruments and methods for this kind of research have just been made available in the recent years and will have to be further developed. With the upcoming new x-ray sources and the increasing possibilities in nanofabrication, exciting and momentous discoveries in the field

of magnetic research are expected.

Bibliography

[Ack07] W. Ackermann, G. Asova, V. Ayvazyan, et al., 'Operation of a free-electron laser from the extreme ultraviolet to the water window', *Nat. Photon.* **1**, 336–342 (2007), DOI: 10.1038/nphoton.2007.76 (cit. on pp. 40, 45, 46).

[Ade09] R. Adelmann, J. Frercks, M. Heßler, and J. Hennig, 'Datenbilder, Zur digitalen Bildpraxis in den Naturwissenschaften', transcript Verlag, Bielefeld, 2009 (cit. on p. 2).

[Alb09] T. R. Albrecht, O. Hellwig, R. Ruiz, M. E. Schabes, B. D. Terris, and X. Z. Wu, 'Nanoscale Magnetic Materials and Apllications', ed. by J. Ping Liu, Erik Fullerton, Oliver Gutfleisch, and David J. Sellmyer, Springer Science+Business Media, 2009, chap. Bit-Patterned Magnetic Recording: Nanoscale Magnetic islands for Data Storage, 237–274, DOI: 10.1007/978-0-387-85600-1_9 (cit. on pp. 51, 53, 68, 91, 97).

[Ama12] J. Amann, W. Berg, V. Blank, et al., 'Demonstration of self-seeding in a hard-X-ray free-electron laser', *Nat. Photon.* **6**, 693–698 (2012), DOI: 10.1038/nphoton.2012.180 (cit. on p. 48).

[Ash76] N. W. Ashcroft and N. D. Mermin, 'Solid State Physics', Cengage Learning Emea, 1976 (cit. on p. 7).

[Att00] D. Attwood, 'Soft X-Rays and Extreme Ultraviolet Radiation', Cambridge University Press, 2000 (cit. on pp. 6, 10, 63).

[Bah01] J. Bahrdt, W. Frentrup, A. Gaupp, M. Scheer, W. Gudat, G. Ingold, and S. Sasaki, 'Elliptically polarizing insertion devices at BESSY II', *Nucl. Instrum. Methods Phys. Res., Sect. A* **467–468, Part 1**, 21–29 (2001), DOI: 10.1016/S0168-9002(01)00554-X (cit. on p. 60).

[Bar10] R. Barth, F. Staier, T. Simpson, S. Mittler, S. Eisebitt, M. Grunze, and A. Rosenhahn, 'Soft X-ray holographic microscopy of chromosomes with high aspect ratio pinholes', *Journal of Biotechnology* **149**, 238 –242 (2010), DOI: 10.1016/j.jbiotec.2010.03.017 (cit. on p. 8).

[Bea59] C. P. Bean and J. D. Livingston, 'Superparamagnetism', *J. Appl. Phys.* **30**, S120–S129 (1959), DOI: 10.1063/1.2185850 (cit. on pp. 52, 84).

[Bea06] E. Beaurepaire, H. Bulou, F. Scheurer, and J. P. Kappler, eds., 'Magnetism: A Synchrotron Radiation Approach', Springer-Verlag Berlin Heidelberg, 2006 (cit. on p. 109).

[Bin83] G. Binnig, H. Rohrer, C. Gerber, and E. Weibel, '7 × 7 Reconstruction on Si(111) Resolved in Real Space', *Phys. Rev. Lett.* **50**, 120–123 (1983), DOI: 10.1103/PhysRevLett.50.120 (cit. on p. 1).

[Bor99] M. Born and E. Wolf, 'Principles of Optics', Seventh edition, Cambridge University Press, 1999 (cit. on p. 32).

[But06] T. Butz, 'Fourier Transformation for Pedestrians', Springer-Verlag Berlin Heidelberg, 2006 (cit. on pp. 30, 31).

[Bü13a] F. Büttner, C. Moutafis, A. Bisig, et al., 'Magnetic states in low-pinning high-anisotropy material nanostructures suitable for dynamic imaging', *Phys. Rev. B* **87**, 134422 (2013), DOI: 10.1103/PhysRevB.87.134422 (cit. on pp. 54, 59, 113).

[Bü13b] F. Büttner, C. Moutafis, M. Schneider, et al., 'Topological mass of skyrmionic spin structures', *submitted* (2013) (cit. on p. 113).

[Cam11] J. Camarero, E. Jimenez, J. Vogel, et al., 'Exploring the limits of soft x-ray magnetic holography: Imaging magnetization reversal of buried interfaces (invited)', *Journal of Applied Physics* **109**, 07D357 (2011), DOI: 10.1063/1.3567035 (cit. on p. 17).

[Cas00] M. Castells, 'End of Millennium, The information Age: Economy, Society and Culture, Vol. 3', Blackwell Publishers, 2000 (cit. on p. 51).

[Cha07] H. N. Chapman, S. P. Hau-Riege, M. J. Bogan, et al., 'Femtosecond time-delay X-ray holography', *Nature* **448**, 676–679 (2007), DOI: 10.1038/nature06049 (cit. on p. 113).

[Che10] Y. Chen, J. Ding, J. Deng, et al., 'Switching Probability Distribution of Bit Islands in Bit Patterned Media', *Magnetics, IEEE Transactions on* **46**, 1990–1993 (2010), DOI: 10.1109/TMAG.2010.2043064 (cit. on p. 84).

[Coe10] J. M. D. Coey, 'Magnetism and Magnetic Materials', Cambridge University Press, 2010 (cit. on p. 76).

[Dit05] R. Dittrich, G. Hu, T. Schrefl, T. Thomson, D. Suess, B. D. Terris, and J. Fidler, 'Angular dependence of the switching field in patterned magnetic elements', *J. Appl. Phys.* **97**, 10J705 (2005), DOI: 10.1063/1.1851931 (cit. on pp. 53, 97).

[Eis04] S. Eisebitt, J. Lüning, W. F. Schlotter, M. Lörgen, O. Hellwig, W. Eberhardt, and J. Stöhr, 'Lensless imaging of magnetic nanostructures by X-ray spectroholography', *Nature* **432**, 885–888 (2004), DOI: 10.1038/nature03139 (cit. on pp. 8, 9, 43, 54).

[Eng91] B. N. Engel, C. D. England, R. A. Van Leeuwen, M. H. Wiedmann, and C. M. Falco, 'Interface magnetic anisotropy in epitaxial superlattices', *Phys. Rev. Lett.* **67**, 1910–1913 (1991), DOI: 10.1103/PhysRevLett.67.1910 (cit. on pp. 56, 88, 89, 100).

[Eng10] J. B. C. Engelen, M Delalande, A. J. le Fèbre, T Bolhuis, T Shimatsu, N Kikuchi, L Abelmann, and J. C. Lodder, 'Thermally induced switching field distribution of a single CoPt dot in a large array', *Nanotechnology* **21**, 035703 (2010) (cit. on pp. 84, 88, 90).

[Eva12] R. F. L. Evans, R. W. Chantrell, U. Nowak, A. Lyberatos, and H.-J. Richter, 'Thermally induced error: Density limit for magnetic data storage', *Appl. Phys. Lett.* **100**, 102402 (2012), DOI: 10.1063/1.3691196 (cit. on p. 52).

[Fle11] S. Flewett and S. Eisebitt, 'Experimental geometry for simultaneous beam characterization and sample imaging allowing for pink beam Fourier transform holography or coherent diffractive imaging', *Appl. Opt.* **50**, 852–858 (2011), DOI: 10.1364/AO.50.000852 (cit. on p. 40).

[Gar95] A. Garg, 'Escape-field distribution for escape from a metastable potential well subject to a steadily increasing bias field', *Phys. Rev. B* **51**, 15592–15595 (1995), DOI: 10.1103/PhysRevB.51.15592 (cit. on pp. 75, 86, 87).

[Gei13] J. Geilhufe, B. Pfau, M. Schneider, et al., 'Focused reference beam x-ray holography', *submitted* (2013) (cit. on pp. 49, 107).

[Gla82] O. Glatter and O. Kratky, eds., 'Small Angle X-ray Scattering', Academic Press, 1982 (cit. on p. 41).

[Goo85] J. W. Goodman, 'Statistical Optics', John Wiley & Sons, 1985 (cit. on pp. 32, 33, 38).

[Goo05] J. W. Goodman, 'Fourier Optics', Third edition, Roberts Company, Englewood, Colorado, 2005 (cit. on pp. 6, 15, 18, 19).

[Gra05] J. Grabis, 'Soft X-ray resonant scattering from magnetic heterostructures', *phdthesis*, Ruhr-Universität Bochum, Fakultät für Physik und Astronomie, 2005 (cit. on pp. 60, 61).

[Gra03] J. Grabis, A. Nefedov, and H. Zabel, 'Diffractometer for soft x-ray resonant magnetic scattering', *Rev. Sci. Instr.* **74**, 4048–4051 (2003), DOI: 10.1063/1.1602932 (cit. on p. 60).

[Gue09] E. Guehrs, C. M. Günther, R. Könnecke, B. Pfau, and S. Eisebitt, 'Holographic soft X-ray omni-microscopy of biological specimens', *Opt. Express* **17**, 6710–6720 (2009) (cit. on p. 5).

[GS07] M. Guizar-Sicairos and J. R. Fienup, 'Holography with extended reference by autocorrelation linear differentialoperation', *Opt. Express* **15**, 17592–17612 (2007) (cit. on p. 48).

[Gun94] L. Gunther and B. Barbara, 'Quantum tunneling across a domain-wall junction', *Phys. Rev. B* **49**, 3926–3933 (1994), DOI: 10.1103/PhysRevB.49.3926 (cit. on pp. 75, 86).

[Guo03] C.-S. Guo, L. Zhang, Z.-Y. Rong, and H.-T. Wang, 'Effect of the fill factor of CCD pixels on digital holograms: comment on the papers "Frequency analysis of digital holography" and "Frequency analysis of digital holography with reconstruction by convolution"', *Opt. Eng.* **42**, 2768–2771 (2003) (cit. on pp. 25, 27).

[Gá48] D. Gábors, 'A new microscopic principle.', *Nature* **161**, 777 (1948) (cit. on p. 5).

[Gá49] D. Gábors, 'Microscopy by reconstructed wave-fronts', *Proc. Royal Soc. A* **197**, 454–487 (1949), DOI: 10.1098/rspa.1949.0075 (cit. on p. 5).

[Gá51] D. Gábors, 'Microscopy by Reconstructed Wave Fronts: II', *Proc. Phys. Soc., Sec. B* **64**, 449–469 (1951), DOI: 10.1088/0370-1301/64/6/301 (cit. on p. 5).

[Gü12] C. M. Günther, 'Application and Development of Fourier Transform Holography', *phdthesis*, Technische Universität Berlin, Fakultät II - Mathematik und Naturwissenschaften, 2012 (cit. on pp. 16, 17, 61, 110, 112).

[Gü08] C. M. Günther, F. Radu, A. Menzel, S. Eisebitt, W. F. Schlotter, R. Rick, J. Lüning, and O. Hellwig, 'Steplike versus continuous domain propagation in Co/Pd multilayer films', *Appl. Phys. Lett.* **93**, 072505 (2008), DOI: 10.1063/1.2968305 (cit. on pp. 6, 17, 62, 64).

[Gü10] C. M. Günther, O. Hellwig, A. Menzel, et al., 'Microscopic reversal behavior of magnetically capped nanospheres', *Phys. Rev. B* **81**, 064411 (2010), DOI: 10.1103/PhysRevB.81.064411 (cit. on pp. 6, 17, 53, 109, 110).

[Gü11] C. M. Günther, B. Pfau, R. Mitzner, et al., 'Sequential femtosecond X-ray imaging', *Nat. Photon.* **5**, 99–102 (2011), DOI: 10.1038/nphoton.2010.287 (cit. on pp. 16, 17, 112).

[HGS12a] HGST, *Deskstar 7K4000*, Mar. 7, 2012, URL: http://www.hitachigst.com/deskstar-7k4000 (cit. on p. 51).

[HGS12b] HGST, *Deskstar 7K4000*, Mar. 19, 2012, URL: http://www.seagate.com/ww/v/index.jsp?locale=en-US&name=terabit-milestone-storage-seagate-pr&vgnextoid=295d922d58716310VgnVCM1000001a48090aRCRD (cit. on p. 52).

[Hau08] T. Hauet, C. M. Günther, B. Pfau, M. E. Schabes, J.-U. Thiele, R. L. Rick, P. Fischer, S. Eisebitt, and O. Hellwig, 'Direct observation of field and temperature induced domain replication in dipolar coupled perpendicular anisotropy films', *Phys. Rev. B* **77**, 184421 (2008), DOI: 10.1103/PhysRevB.77.184421 (cit. on pp. 6, 110).

[Hau09] T. Hauet, E. Dobisz, S. Florez, J. Park, B. Lengsfield, B. D. Terris, and O. Hellwig, 'Role of reversal incoherency in reducing switching field and switching field distribution of exchange coupled composite bit patterned media', *Appl. Phys. Lett.* **95**, 262504 (2009), DOI: 10.1063/1.3276911 (cit. on pp. 54, 113).

[Hei11] R. Heine, T. Gorniak, T. Nisius, C. Christophis, M. Pettitt, F. Staier, T. Wilhein, S. Rehbein, M. Grunze, and A. Rosenhahn, 'Digital in-line X-ray holography with zone plates', *Ultramicroscopy* **111**, 1131 –1136 (2011), DOI: 10.1016/j.ultramic.2011.02.002 (cit. on p. 8).

[Hel07a] O. Hellwig, A. Berger, T. Thomson, E. Dobisz, Z. Z Bandic, H. Yang, D. S. Kercher, and E. E. Fullerton, 'Separating dipolar broadening from the intrinsic switching field distribution in perpendicular patterned media', *Appl. Phys. Lett.* **90**, 162516–3 (2007), DOI: 10.1063/1.2730744 (cit. on pp. 53, 72, 75).

[Hel08] O. Hellwig, A. Moser, E. Dobisz, Z. Z. Bandic, H. Yang, D. S. Kercher, J. D. Risner-Jamtgaard, D. Yaney, and E. E. Fullerton, 'Suppression of magnetic trench material in bit patterned media fabricated by blanket deposition onto prepatterned substrates', *Applied Physics Letters* **93**, 192501 (2008), DOI: 10.1063/1.3013857 (cit. on pp. 56, 57).

[Hel09] O. Hellwig, T. Hauet, T. Thomson, E. Dobisz, J. D. Risner-Jamtgaard, D. Yaney, B. D. Terris, and E. E. Fullerton, 'Coercivity tuning in Co/Pd multilayer based bit patterned media', *Appl. Phys. Lett.* **95**, 232505–3 (2009), DOI: 10.1063/1.3271679 (cit. on p. 56).

[Hel06] O. Hellwig, S. Eisebitt, W. Eberhardt, W. F. Schlotter, J. Lüning, and J. Stöhr, 'Magnetic imaging with soft x-ray spectroholography', *J. Appl. Phys.* **99**, 08H307 (2006), DOI: 10.1063/1.2165925 (cit. on p. 68).

[Hel07b] O. Hellwig, A. Berger, J. B. Kortright, and E. E. Fullerton, 'Domain structure and magnetization reversal of antiferromagnetically coupled perpendicular anisotropy films', *J. Magn. Magn. Mater.* **319**, 13–55 (2007), DOI: 10.1016/j.jmmm.2007.04.035 (cit. on p. 68).

[Hil11] M. Hilbert and P. López, 'The World's Technological Capacity to Store, Communicate, and Compute Information', *Science* **332**, 60–65 (2011), DOI: 10.1126/science.1200970 (cit. on p. 51).

[Hu05a] G. Hu, T. Thomson, C. T. Rettner, S. Raoux, and B. D. Terris, 'Magnetization reversal in Co/Pd nanostructures and films', *J. Appl. Phys.* **97**, 10J702 (2005), DOI: 10.1063/1.1849572 (cit. on pp. 68, 97).

[Hu05b] G. Hu, T. Thomson, C. Rettner, and B. Terris, 'Rotation and wall propagation in multidomain Co/Pd islands', *IEEE Transactions on Magnetics* **41**, 3589–3591 (2005), DOI: 10.1109/TMAG.2005.854733 (cit. on p. 53).

[Hub98] A. Huber and R. Schäfer, 'Magnetic Domains', Springer-Verlag Berlin Heidelberg, 1998 (cit. on p. 109).

[Ins12] P. Instruments, *Festplattenlaufwerk*, June 1, 2012, URL: http://www.princetoninstruments.com/products/xraycam/pimte/dsheet.aspx (cit. on p. 61).

[Jos65] R. I. Joseph and E. Schlömann, 'Demagnetizing Field in Nonellipsoidal Bodies', *J. Appl. Phys.* **36**, 1579–1593 (1965) (cit. on p. 77).

[Kel09] D. P. Kelly, B. M. Hennelly, N. Pandey, T. J. Naughton, and W. T. Rhodes, 'Resolution limits in practical digital holographic systems', *Opt. Eng.* **48**, 095801–13 (2009) (cit. on p. 25).

[Kre02a] T. M. Kreis, 'Frequency analysis of digital holography with reconstruction by convolution', *Opt. Eng.* **41**, 1829–1839 (2002) (cit. on pp. 25–27).

[Kre02b] T. M. Kreis, 'Frequency analysis of digital holography', *Opt. Eng.* **41**, 771–778 (2002) (cit. on p. 25).

[Kro09] P. Krone, D. Makarov, T. Schrefl, and M. Albrecht, 'Effect of the anisotropy distribution on the coercive field and switching field distribution of bit patterned media', *J. Appl. Phys.* **106**, 103913 (2009), DOI: 10.1063/1.3260240 (cit. on p. 98).

[Kro10a] P. Krone, D. Makarov, M. Albrecht, and T. Schrefl, 'Magnetization reversal of bit patterned media: Role of the angular orientation of the magnetic anisotropy axes', *J. Appl. Phys.* **108**, 013906 (2010), DOI: 10.1063/1.3457037 (cit. on p. 98).

[Kro10b] P. Krone, D. Makarov, M. Albrecht, T. Schrefl, and D. Suess, 'Magnetization reversal processes of single nanomagnets and their energy barrier', *J. Magn. Magn. Mater.* **322**, 3771–3776 (2010), DOI: 10.1016/j.jmmm.2010.07.041 (cit. on pp. 84, 89).

[Kur72] J. Kurkijärvi, 'Intrinsic Fluctuations in a Superconducting Ring Closed with a Josephson Junction', *Phys. Rev. B* **6**, 832–835 (1972), DOI: 10.1103/PhysRevB.6.832 (cit. on p. 86).

[Lau07] J. W. Lau, R. D. McMichael, M. A. Schofield, and Y. Zhu, 'Correlation of edge roughness to nucleation field and nucleation field distribution in patterned Permalloy elements', *J. Appl. Phys.* **102**, 023916 (2007), DOI: 10.1063/1.2761850 (cit. on p. 98).

[Lau08] J. W. Lau, R. D. McMichael, S. H. Chung, J. O. Rantschler, V. Parekh, and D. Litvinov, 'Microstructural origin of switching field distribution in patterned Co/Pd multilayer nanodots', *Appl. Phys. Lett.* **92**, 012506–3 (2008), DOI: 10.1063/1.2822439 (cit. on pp. 53, 89, 98, 100).

[Lee11] J. Lee, C. Brombacher, J. Fidler, B. Dymerska, D. Suess, and M. Albrecht, 'Contribution of the easy axis orientation, anisotropy distribution and dot size on the switching field distribution of bit patterned media', *Appl. Phys. Lett.* **99**, 062505 (2011), DOI: 10.1063/1.3623752 (cit. on p. 98).

[Len01] B. Lengeler, 'Coherence in X-ray physics', *Naturwissenschaften* **88**, 249–260 (2001), DOI: 10.1007/s001140100221 (cit. on pp. 32, 37).

[Mar08] S. Marchesini, S. Boutet, A. E. Sakdinawat, et al., 'Massively parallel X-ray holography', *Nat. Photon.* **2**, 560–563 (2008), DOI: 10.1038/nphoton.2008.154 (cit. on pp. 48, 107).

[McN92] I. McNulty, J. Kirz, C. Jacobsen, E. H. Anderson, M. R. Howells, and D. P. Kern, 'High-Resolution Imaging by Fourier Transform X-ray Holography', *Science* **256**, 1009–1012 (1992), DOI: 10.1126/science.256.5059.1009 (cit. on pp. 6, 9).

[Mer04] H.-C. Mertins, S. Valencia, D. Abramsohn, A. Gaupp, W. Gudat, and P. M. Oppeneer, 'X-ray Kerr rotation and ellipticity spectra at the 2p edges of Fe, Co, and Ni', *Phys. Rev. B* **69**, 064407– (2004), DOI: 10.1103/PhysRevB.69.064407 (cit. on pp. 20, 24, 25).

[Mor05] J. Moritz, B. Dieny, J. P. Nozières, Y. Pennec, J. Camarero, and S. Pizzini, 'Experimental evidence of a 1/H activation law in nanostructures with perpendicular magnetic anisotropy', *Phys. Rev. B* **71**, 100402 (2005), DOI: 10.1103/PhysRevB.71.100402 (cit. on p. 87).

[Pat01] D. Paterson, B. Allman, P. McMahon, et al., 'Spatial coherence measurement of X-ray undulator radiation', *Optics Communications* **195**, 79–84 (2001), DOI: 10.1016/S0030-4018(01)01276-7 (cit. on p. 37).

[Pfa10a] B. Pfau, C. M. Günther, S. Schaffert, et al., 'Femtosecond pulse x-ray imaging with a large field of view', *New Journal of Physics* **12**, 095006 (2010) (cit. on pp. 15, 17, 30, 39, 40, 46, 113, 133).

[Pfa11] B. Pfau, C. M. Günther, E. Guehrs, et al., 'Origin of magnetic switching field distribution in bit patterned media based on pre-patterned substrates', *Appl. Phys. Lett.* **99**, 062502 (2011), DOI: 10.1063/1.3623488 (cit. on pp. 6, 17, 24, 53, 63, 97, 133).

[Pfa12] B. Pfau, S. Schaffert, L. Müller, et al., 'Ultrafast optical demagnetization manipulates nanoscale spin structure in domain walls', *Nat. Commun.* **3**, 1100– (2012), DOI: 10.1038/ncomms2108 (cit. on pp. 111, 113).

[Pfa10b] B. Pfau, C. M. Günther, R. Könnecke, E. Guehrs, O. Hellwig, W. F. Schlotter, and S. Eisebitt, 'Magnetic imaging at linearly polarized x-ray sources', *Opt. Express* **18**, 13608–13615 (2010), DOI: 10.1364/OE.18.013608 (cit. on p. 111).

[Pie05] U. Pietsch, T. Panzner, W. Leitenberger, and I. Vartanyants, 'Coherence experiments using white synchrotron radiation', *Physica B: Condensed Matter* **357**, 45–52 (2005), DOI: 10.1016/j.physb.2004.11.017 (cit. on p. 36).

[Pre07] W. H. Press, S. A. Teukolsky, W. T. Vetterling, and B. P. Flannery, 'Numerical Recipes 3rd Edition: The Art of Scientific Computing', Cambridge University Press, 2007 (cit. on pp. 30, 31).

[Ric07] H. J. Richter, 'The transition from longitudinal to perpendicular recording', *J. Phys. D* **40**, R149 (2007) (cit. on pp. 51, 52).

[Ros08] A. Rosenhahn, R. Barth, F. Staier, T. Simpson, S. Mittler, S. Eisebitt, and M. Grunze, 'Digital in-line soft x-ray holography with element contrast', *J. Opt. Soc. Am. A* **25**, 416–422 (2008) (cit. on p. 8).

[Ros01] C. A. Ross, 'Patterned Magnetic Recording Media', *Annu. Rev. Mater. Res.* **31**, 203–235 (2001) (cit. on pp. 78, 92, 97).

[Sac12] M. Sacchi, H. Popescu, N. Jaouen, M. Tortarolo, F. Fortuna, R. Delaunay, and C. Spezzani, 'Magnetic imaging by Fourier transform holography using linearly polarized x-rays', *Opt. Express* **20**, 9769–9776 (2012), DOI: 10.1364/OE.20.009769 (cit. on p. 21).

[Sch13] S. Schaffert, F. Büttner, J. Geilhufe, C. M. Günther, B. Pfau, C. v. Korff-Schmising, M. Schneider, and S. Eisebitt, 'Realization of Fourier transform holography at VUV energies exploiting magnetic dichroism', *accepted in New Journal of Physics* (2013) (cit. on p. 8).

[Sch07a] A. Scherz, W. F. Schlotter, K. Chen, et al., 'Phase imaging of magnetic nanostructures using resonant soft x-ray holography', *Phys. Rev. B* **76**, 214410–5 (2007), DOI: 10.1103/PhysRevB.76.214410 (cit. on p. 22).

[Sch07b] W. F. Schlotter, 'Lensless Fourier Transform Holography With Soft X-Rays', *phdthesis*, Stanford University, 2007 (cit. on pp. 15, 17, 55, 61).

[Sch06] W. F. Schlotter, R. Rick, K. Chen, et al., 'Multiple reference Fourier transform holography with soft x rays', *Appl. Phys. Lett.* **89**, 163112 (2006), DOI: 10.1063/1.2364259 (cit. on pp. 15, 17).

[Sch07c] W. F. Schlotter, J. Lüning, R. Rick, K. Chen, A. Scherz, S. Eisebitt, C. M. Günther, W. Eberhardt, O. Hellwig, and J. Stöhr, 'Extended field of view soft x-ray Fourier transform holography: toward imaging ultrafast evolution in a single shot', *Opt. Lett.* **32**, 3110–3112 (2007) (cit. on pp. 15, 17, 113).

[Sha94] M. P. Sharrock, 'Time dependence of switching fields in magnetic recording media (invited)', *J. Appl. Phys.* **76**, 6413–6418 (1994), DOI: 10.1063/1.358282 (cit. on pp. 52, 86, 87).

[Sha07] J. M. Shaw, W. H. Rippard, S. E. Russek, T. Reith, and C. M. Falco, 'Origins of switching field distributions in perpendicular magnetic nanodot arrays', *J. Appl. Phys.* **101**, 023909–4 (2007) (cit. on p. 98).

[Sha08] J. M. Shaw, S. E. Russek, T. Thomson, M. J. Donahue, B. D. Terris, O. Hellwig, E. Dobisz, and M. L. Schneider, 'Reversal mechanisms in perpendicularly magnetized nanostructures', *Phys. Rev. B* **78**, 024414– (2008) (cit. on p. 98).

[Sha09] J. M. Shaw, H. T. Nembach, T. J. Silva, S. E. Russek, R. Geiss, C. Jones, N. Clark, T. Leo, and D. J. Smith, 'Effect of microstructure on magnetic properties and anisotropy distributions in Co/Pd thin films and nanostructures', *Phys. Rev. B* **80**, 184419– (2009) (cit. on p. 98).

[Sha10] J. M. Shaw, M. Olsen, J. W. Lau, M. L. Schneider, T. J. Silva, O. Hellwig, E. Dobisz, and B. Terris, 'Intrinsic defects in perpendicularly magnetized multilayer thin films and nanostructures', *Phys. Rev. B* **82**, 144437– (2010), DOI: 10.1103/PhysRevB.82.144437 (cit. on pp. 53, 89, 98, 103).

[Shi09] Y. Shiroishi, K. Fukuda, I. Tagawa, H. Iwasaki, S. Takenoiri, H. Tanaka, H. Mutoh, and N. Yoshikawa, 'Future Options for HDD Storage', *Magnetics, IEEE Transactions on* **45**, 3816 –3822 (2009), DOI: 10.1109/TMAG.2009.2024879 (cit. on p. 52).

[Sin08] A. Singer, I. A. Vartanyants, M. Kuhlmann, S. Düsterer, R. Treusch, and J. Feldhaus, 'Transverse-Coherence Properties of the Free-Electron-Laser FLASH at DESY', *Phys. Rev. Lett.* **101**, 254801 (2008), DOI: 10.1103/PhysRevLett.101.254801 (cit. on p. 37).

[Sko06] R. Skomski, J. Zhou, R. D. Kirby, and D. J. Sellmyer, 'Micromagnetic energy barriers', *J. Appl. Phys.* **99**, 08B906 (2006), DOI: 10.1063/1.2173228 (cit. on p. 87).

[Sta08] L.-M. Stadler, C. Gutt, T. Autenrieth, O. Leupold, S. Rehbein, Y. Chushkin, and G. Grübel, 'Hard X Ray Holographic Diffraction Imaging', *Phys. Rev. Lett.* **100**, 245503–4 (2008) (cit. on pp. 17, 22).

[Sta04] J. Stangl, V. Holý, and G. Bauer, 'Structural properties of self-organized semiconductor nanostructures', *Rev. Mod. Phys.* **76**, 725–783 (2004), DOI: 10.1103/RevModPhys.76.725 (cit. on p. 8).

[Sti11] D. Stickler, R. Frömter, H. Stillrich, et al., 'Domain size in systems with canted magnetization', *Phys. Rev. B* **84**, 104412 (2011), DOI: 10.1103/PhysRevB.84.104412 (cit. on p. 17).

[Sto06] J. Stoehr and H. C. Siegmann, 'Magnetism', Springer-Verlag Berlin Heidelberg, 2006 (cit. on pp. 19, 56, 68, 76, 79).

[SN09] S. Streit-Nierobisch, D. Stickler, C. Gutt, et al., 'Magnetic soft x-ray holography study of focused ion beam-patterned Co/Pt multilayers', *J. Appl. Phys.* **106**, 083909 (2009), DOI: 10.1063/1.3246724 (cit. on pp. 6, 17, 23, 42, 66).

[Str65a] G. Stroke, 'Lenseless Fourier-trensform method for optical holography', *Appl. Phys. Lett.* 202 (1965) (cit. on p. 5).

[Str64] G. Stroke and D. Falconer, 'Attainment of high resolutions in wavefront-reconstruction imaging', *Phys. Lett.* **13**, 306–309 (1964) (cit. on p. 5).

[Str65b] G. W. Stroke and R. C. Restrick, 'Holography With Spatially Noncoherent Light', *Appl. Phys. Lett.* **7**, 229 (1965), DOI: 10.1063/1.1754392 (cit. on p. 5).

[Thi08] P. Thibault, M. Dierolf, A. Menzel, O. Bunk, C. David, and F. Pfeiffer, 'High-Resolution Scanning X-ray Diffraction Microscopy', *Science* **321**, 379–382 (2008) (cit. on p. 11).

[Tho06] T. Thomson, G. Hu, and B. D. Terris, 'Intrinsic Distribution of Magnetic Anisotropy in Thin Films Probed by Patterned Nanostructures', *Phys. Rev. Lett.* **96**, 257204– (2006), DOI: 10.1103/PhysRevLett.96.257204 (cit. on pp. 53, 89, 97).

[Tra05] C. Q. Tran, A. G. Peele, A. Roberts, K. A. Nugent, D. Paterson, and I. McNulty, 'Synchrotron beam coherence: a spatially resolved measurement', *Opt. Lett.* **30**, 204–206 (2005), DOI: 10.1364/OL.30.000204 (cit. on p. 37).

[Tra07] C. Q. Tran, G. J. Williams, A. Roberts, S. Flewett, A. G. Peele, D. Paterson, M. D. de Jonge, and K. A. Nugent, 'Experimental Measurement of the Four-Dimensional Coherence Function for an Undulator X-Ray Source', *Phys. Rev. Lett.* **98**, 224801 (2007), DOI: 10.1103/PhysRevLett.98.224801 (cit. on p. 37).

[Wan04] H.-T. Wang, S. T. Chui, A. Oriade, and J. Shi, 'Temperature dependence of the fluctuation of the switching field in small magnetic structures', *Phys. Rev. B* **69**, 064417 (2004), DOI: 10.1103/PhysRevB.69.064417 (cit. on p. 88).

[Wan12] T. Wang, D. Zhu, B. Wu, et al., 'Femtosecond Single-Shot Imaging of Nanoscale Ferromagnetic Order in Co/Pd Multilayers Using Resonant X-Ray Holography', *Phys. Rev. Lett.* **108**, 267403 (2012), DOI: 10.1103/PhysRevLett.108.267403 (cit. on p. 111).

[Wel99] D. Weller and A. Moser, 'Thermal effect limits in ultrahigh-density magnetic recording', *Magnetics, IEEE Transactions on* **35**, 4423 –4439 (1999), DOI: 10.1109/20.809134 (cit. on p. 52).

[Wer97] W. Wernsdorfer, E. B. Orozco, K. Hasselbach, A. Benoit, B. Barbara, N. Demoncy, A. Loiseau, H. Pascard, and D. Mailly, 'Experimental Evidence of the Néel-Brown Model of Magnetization Reversal', *Phys. Rev. Lett.* **78**, 1791–1794 (1997), DOI: 10.1103/PhysRevLett.78.1791 (cit. on p. 88).

[Wik12] Wikipedia, *Festplattenlaufwerk*, Mar. 7, 2012, URL: http://de.wikipedia.org/wiki/Festplatte (cit. on p. 52).

[Win65] J. Winthrop and C. Worthington, 'X-ray microscopy by successive Fourier transformation', *Phys. Lett.* **15**, 2–4 (1965) (cit. on p. 5).

[Win66] J. Winthrop and C. Worthington, 'X-ray microscopy by successive Fourier transformation II. An optical analogue experiment', *Phys. Lett.* **21**, 413–415 (1966) (cit. on p. 5).

[Zhu10] D. Zhu, M. Guizar-Sicairos, B. Wu, et al., 'High-Resolution X-Ray Lensless Imaging by Differential Holographic Encoding', *Phys. Rev. Lett.* **105**, 043901 (2010), DOI: 10.1103/PhysRevLett.105.043901 (cit. on pp. 48, 54, 107).

Publications

Methodical x-ray FTH development

S. Flewett, C. M. Günther, C. von Korff Schmising, B. Pfau, J. Mohanty, F. Büttner, M. Riemeier, M. Hantschmann, M. Kläui, and S. Eisebitt "Holographically aided iterative phase retrieval" *Optics Express* **20**, 29210 (2012). http://dx.doi.org/10.1364/OE.20.029210

S. Flewett, S. Schaffert, J. Mohanty, E. Guehrs, J. Geilhufe, C. M. Günther, B. Pfau, and S. Eisebitt "Method for Single-Shot Coherent Diffractive Imaging of Magnetic Domains" *Phsical Review Letters* **108**, 223902 (2012). http://dx.doi.org/10.1103/PhysRevLett.108.223902

E. Guehrs, A. M. Stadler, S. Flewett, S. Frömmel, J. Geilhufe, B. Pfau, T. Rander, S. Schaffert, G. Büldt, and S. Eisebitt "Soft x-ray tomoholography" *New Journal of Physics* **14**, 013022 (2012). http://dx.doi.org/10.1088/1367-2630/14/1/013022

B. Pfau, C. M. Günther, R. Könnecke, E. Guehrs, O. Hellwig, W. F. Schlotter, and S. Eisebitt "Magnetic imaging at linearly polarized x-ray sources" *Optics Express* **18**, 13608 (2010). http://dx.doi.org/10.1364/OE.18.013608

E. Guehrs, C. M. Günther, B. Pfau, T. Rander, S. Schaffert, W. F. Schlotter, and S. Eisebitt "Wavefield back-propagation in high-resolution X-ray holography with a movable field of view" *Optics Express* **18**, 18922 (2010). http://dx.doi.org/10.1364/OE.18.018922

E. Guehrs, C. M. Günther, R. Könnecke, B. Pfau, and S. Eisebitt "Holographic soft X-ray omni-microscopy of biological specimens" *Optics Express* **17**, 6710 (2009). http://dx.doi.org/10.1364/OE.17.006710

Nano-magnetism research

F. Büttner, C. Moutafis, A. Bisig, P. Wohlhüter, C. M. Günther, J. Mohanty, J. Geilhufe, M. Schneider, C. v. Korff Schmising, S. Schaffert, B. Pfau, M. Hantschmann, M. Riemeier, M. Emmel, S. Finizio, G. Jakob, M. Weigand, J. Rhensius, J. H. Franken, R. Lavrijsen, H. J. M. Swagten, H. Stoll, S. Eisebitt, and M. Kläui "Magnetic states in low-pinning high-anisotropy material nanostructures suitable for dynamic imaging"

Physical Review B **87**, 134422 (2013). http://dx.doi.org/10.1103/PhysRevB.87.134422

M. Ewerlin, B. Pfau, C. M. Günther, S. Schaffert, S. Eisebitt, R. Abrudan, and H. Zabel "Exploration of magnetic fluctuations in PdFe films" *Journal of Physics: Condensed Matter* **25**, 266001 (2013). http://dx.doi.org/10.1088/0953-8984/25/26/266001

B. Pfau, C. M. Günther, E. Guehrs, T. Hauet H. Yang, L. Vinh, X. Xu, D. Yaney, R. Rick, S. Eisebitt, and O. Hellwig "Origin of magnetic switching field distribution in bit patterned media based on pre-patterned substrates" *Applied Physics Letters* **99**, 062502 (2011). http://dx.doi.org/10.1063/1.3623488

C. M. Günther, O. Hellwig, A. Menzel, B. Pfau, F. Radu, D. Makarov, M. Albrecht, A. Goncharov, T. Schrefl, W. F. Schlotter, R. Rick, J. Lüning, and S. Eisebitt "Microscopic reversal behavior of magnetically capped nanospheres" *Physical Review B* **81**, 064411 (2010). http://dx.doi.org/10.1063/1.2968305

T. Hauet, C. M. Günther, O. Hovorka, A. Berger, M.-Y. Im, P. Fischer, T. Eimüller, and O. Hellwig "Field driven ferromagnetic phase nucleation and propagation in antiferromagnetically coupled multilayer films with perpendicular anisotropy" *Applied Physics Letters* **93**, 042505 (2008). http://dx.doi.org/10.1063/1.2961001

FEL science

L. Müller, C. Gutt, B. Pfau, S. Schaffert, J. Geilhufe, F. Büttner, J. Mohanty, S. Flewett, R. Treusch, S. Düsterer, H. Redlin, A. Al-Shemmary, M. Hille, A. Kobs, R. Frömter, H. P. Oepen, B. Ziaja, N. Medvedev, S.-K. Son, R. Thiele, R. Santra, B. Vodungbo, J. Lüning, S. Eisebitt, and G. Grübel "Breakdown of the X-Ray Resonant Magnetic Scattering Signal during Intense Pulses of Extreme Ultraviolet Free-Electron-Laser Radiation" *Physical Review Letters* **110**, 234801 (2013). http://dx.doi.org/10.1103/PhysRevLett.110.234801

L. Müller, C. Gutt, S. Streit-Nierobisch, M. Walther, S. Schaffert, B. Pfau, J. Geilhufe, F. Buttner, S. Flewett, C. M. Günther, S. Eisebitt, A. Kobs, M. Hille, D. Stickler, R. Frömter, H. P. Oepen, J. Lüning, and G. Grübel "Endstation for ultrafast magnetic scattering experiments at the free-electron laser in Hamburg" *Review of Scientific Instruments* **84**, 013906 (2013). http://dx.doi.org/10.1063/1.4773543

B. Pfau, S. Schaffert, L. Müller, C. Gutt, A. Al-Shemmary, F. Büttner, R. Delaunay, S. Düsterer, S. Flewett, R. Frömter, J. Geilhufe, E. Guehrs, C. Günther, R. Hawaldar, M. Hille, N. Jaouen, A. Kobs, K. Li, J. Mohanty, H. Redlin, W. Schlotter, D. Stickler, R. Treusch, B. Vodungbo, M. Kläui, H. Oepen, J. Lüning, G. Grübel, and S. Eisebitt "Ultrafast optical demagnetization manipulates

nanoscale spin structure in domain walls" *Nature Communications* **3**, 1100 (2012). http://dx.doi.org/10.1038/ncomms2108

T. Wang, D. Zhu, B. Wu, C. Graves, S. Schaffert, T. Rander, L. Müller, B. Vodungbo, C. Baumier, D. P. Bernstein, B. Bräuer, V. Cros, S. de Jong, R. Delaunay, A. Fognini, R. Kukreja, S. Lee, V. López-Flores, J. Mohanty, B. Pfau, H. Popescu, M. Sacchi, A. B. Sardinha, F. Sirotti, P. Zeitoun, M. Messerschmidt, J. J. Turner, W. F. Schlotter, O. Hellwig, R. Mattana, N. Jaouen, F. Fortuna, Y. Acremann, C. Gutt, H. A. Dürr, E. Beaurepaire, C. Boeglin, S. Eisebitt, G. Grübel, J. Lüning, J. Stöhr, and A. O. Scherz "Femtosecond Single-Shot Imaging of Nanoscale Ferromagnetic Order in *Co/Pd* Multilayers Using Resonant X-Ray Holography" *Physical Review Letters* **108**, 267403 (2012). http://dx.doi.org/10.1103/PhysRevLett.108.267403

C. M. Günther, B. Pfau, R. Mitzner, B. Siemer, S. Roling, H. Zacharias, O. Kutz, I. Rudolph, D. Schondelmaier, R. Treusch and S. Eisebitt "Sequential femtosecond X-Ray imaging" *Nature Photonics* **5**, 99 (2011). http://dx.doi.org/10.1038/nphoton.2010.287

B. Pfau, C. M. Günther, S. Schaffert, R. Mitzner, B. Siemer, S. Roling, H. Zacharias, O. Kutz, I. Rudolph, R. Treusch, and S. Eisebitt "Femtosecond pulse x-ray imaging with a large field of view" *New Journal of Physics* **12**, 095006 (2010). http://dx.doi.org/10.1088/1367-2630/12/9/095006

C. Gutt, S. Streit-Nierobisch, L.-M. Stadler, B. Pfau, C. M. Günther, R. Könnecke, R. Frömter, A. Kobs, D. Stickler, H. P. Oepen, R. R. Fäustlin, R. Treusch, J. Feldhaus, E. Weckert, I. A. Vartanyants, M. Grunze, A. Rosenhahn, T. Wilhein, S. Eisebitt, and G. Grübel "Single-pulse resonant magnetic scattering using a soft x-ray free-electron laser" *Physical Review B* **81**, 100401 (2010). http://dx.doi.org/10.1103/PhysRevB.81.100401

C. Gutt, L.-M. Stadler, S. Streit-Nierobisch, A. P. Mancuso, A. Schropp, B. Pfau, C. M. Günther, R. Könnecke, J. Gulden, B. Reime, J. Feldhaus, E. Weckert, I. A. Vartanyants, O. Hellwig, F. Staier, R. Barth, M. Grunze, A. Rosenhahn, D. Stickler, H. Stillrich, R. Frömter, H. P. Oepen, M. Martins, T. Nisius, T. Wilhein, B. Faatz, N. Guerassimova, K. Honkavaara, V. Kocharyan, R. Treusch, E. Saldin, S. Schreiber, E. A. Schneidmiller, M. V. Yurkov, S. Eisebitt, and G. Grübel "Resonant magnetic scattering with soft x-ray pulses from a free-electron laser operating at 1.59 nm" *Physical Review B* **79**, 212406 (2009). http://dx.doi.org/10.1103/PhysRevB.79.212406

A. Rosenhahn, F. Staier, T. Nisius, D. Schäfer, R. Barth, C. Christophis, L.-M. Stadler, S. Streit-Nierobisch, C. Gutt, A. Mancuso, A. Schropp, J. Gulden, B. Reime, J. Feldhaus, E. Weckert, B. Pfau, C. M. Günther, R. Könnecke, S. Eisebitt, M. Martins, B. Faatz, N. Guerassimova, K. Honkavaara, R. Treusch, E. Saldin, S. Schreiber,

E. A. Schneidmiller, M. V. Yurkov, I. Vartanyants, G. Grübel, M. Grunze, and T. Wilhein "Digital In-line Holography with femtosecond VUV radiation provided by the free-electron laser FLASH" *Optics Express* **17**, 8220 (2009). http://dx.doi.org/10.1364/OE.17.008220

A. P. Mancuso, A. Schropp, B. Reime, L.-M. Stadler, A. Singer, J. Gulden, S. Streit-Nierobisch, C. Gutt, G. Grübel, J. Feldhaus, F. Staier, R. Barth, A. Rosenhahn, M. Grunze, T. Nisius, T. Wilhein, D. Stickler, H. Stillrich, R. Frömter, H.-P. Oepen, M. Martins, B. Pfau, C. M. Günther, R. Könnecke, S. Eisebitt, B. Faatz, N. Guerassimova, K. Honkavaara, V. Kocharyan, R. Treusch, E. Saldin, S. Schreiber, E. A. Schneidmiller, M. V. Yurkov, E. Weckert, and I. A. Vartanyants "Coherent-Pulse 2D Crystallography Using a Free-Electron Laser X-Ray Source" *Physical Review Letters* **102**, 035502 (2009). http://dx.doi.org/10.1103/PhysRevLett.102.035502

Materials science

M. Leitner, B. Sepiol, L.-M. Stadler, and B. Pfau "Time-resolved study of the crystallization dynamics in a metallic glass" *Physical Review B* **86**, 064202 (2012). http://dx.doi.org/10.1103/PhysRevB.86.064202

M. Leitner, B. Sepiol, L.-M. Stadler, B. Pfau, and G. Vogl "Atomic diffusion studied with coherent X-rays" *Nature Materials* **8**, 717 (2009). http://dx.doi.org/10.1038/nmat2506

R. Reitinger, B. Sepiol, G. Vogl, B. Pfau, L.-M. Stadler, S. Stankov, F. Zontone, N. Spiridis, and J. Korecki "Morphology of Fe/MgO(001) ultrathin films", *Journal of Applied Physics*, **102**, 034310 (2007). http://dx.doi.org/10.1063/1.2760844

B. Pfau, L.-M. Stadler, B. Sepiol, R. Weinkamer, J. W. Kantelhardt, F. Zontone, and G. Vogl "Coarsening dynamics in elastically anisotropic alloys" *Physical Review B* **73**, 180101 (2006). http://dx.doi.org/10.1103/PhysRevB.73.180101

L.-M. Stadler, B. Sepiol, B. Pfau, J. W. Kantelhardt, R. Weinkamer, and G. Vogl "Detrended fluctuation analysis in x-ray photon correlation spectroscopy for determining coarsening dynamics in alloys" *Physical Review E* **74**, 041107 (2006). http://dx.doi.org/10.1103/PhysRevE.74.041107

Experimental orthopedics

A.-S. Silber, B. Pfau, T. Tan, R. Jacob, D. Jones, and T. Meyer "Dynamic redistribution of paxillin in bovine osteoblasts stimulated with adenosine 5'-triphosphate" *Journal of Molecular Histology*, **43**, 571 (2012). http://dx.doi.org/10.1007/s10735-012-9419-x

L. Tan, T. Meyer, B. Pfau, T. Hofmann, T. W. Tan, and D. Jones "Rapid vinculin exchange dynamics at focal adhesions in primary osteoblasts following shear flow stimulation" *Journal of musculoskeletal & neuronal interactions* **10**, 92 (2010).

Acknowledgements

As being typical for modern experimental physics, the experimental work in this thesis was carried out as a collaboration of scientists from different places. In particular, science at synchrotrons and free-electron lasers needs an experienced team to achieve successful results. Furthermore, the studies involved experts in sample preparation, characterization and analysis methods.

The first part of this thesis partly goes back to ideas that have been published in Ref. [Pfa10a]. The manuscript of the publication was written by the author (BP) of this thesis, with correction from all co-authors listed. The simulations presented in the publication were performed by BP and Stefan Schaffert. The experiment described in the publication was conducted by BP, Christian M. Günther (CMG), Stefan Eisebitt (SE), Rolf Mitzner, Sebastian Roling, Björn Siemer and Rolf Treusch at the FLASH facility in Hamburg, Germany. The sample was prepared by Oliver Kutz and Ivo Rudolph at the BESSY laboratories[1] in Berlin, Germany.

The experiment presented in the second part of the thesis was conceived at the Hitachi Global Storage Technologies (HGST)[2] laboratories in San José, USA by Olav Hellwig (OH). Part of the results from this study was published as Ref. [Pfa11]. The manuscript of the publication was written by BP, with input and correction from all co-authors listed. The patterned substrate and the magnetic layer were prepared at the HGST labs by Thomas Hauet, OH, H. Yang, and Xiaoyu Xu. The magnetic characterization was done by Tyler Hennen from HGST. The holographic mask was produced by Ramon Rick from the SLAC National Accelerator Laboratory in Menlo Park, USA. The magnetic imaging experiments at the BESSY II synchrotron source were carried out by BP, CMG, OH, Erik Gührs, and SE. The transmission electron microscopy and related sample preparation was conducted by Deborah Yaney, and Loc Vinh again at HGST.

I would like to thank all the contributing researches for their assistance and commitment to the experiments and for the fruitful discussions. In particular, I greatly appreciate the help of *Olav Hellwig* who is the father of the bit-patterned media experiment and who guided me through the whole project.

During my time as a PhD student at the BESSY synchrotron facility and later at the TU Berlin, I have had the special pleasure of being part of a work group that is distinctly open-minded, communicative, cooperative and creative. I did and still do enjoy the collective work, the continuous progress, and the scientific successes as well as the

1 In 2009 BESSY was transfered to the Helmholtz-Zentrum Berlin for Materials and Energy (HZB).
2 Since 2012 HGST belongs to Western Digital.

after-work beer and the hiking trips. Last but not least, the group forms one of the most experienced, but also entertaining teams for beamtimes at synchrotrons and free-electron lasers (and we had a lot of those).

I am deeply grateful to *Stefan Eisebitt* who is heading, organizing, motivating and inspiring the group. Stefan was the supervisor of my PhD as well as my mentor in the world of science. With him I have entered the exciting free-electron laser business. I would like to thank Stefan for his continuous support, the unique scientific opportunities and his patience regarding my thesis.

Christian Günther is the second colleague with whom I am working together since my arrival in Berlin. Most of the time since then we were sharing the office. We had countless discussions about science and about anything and everything else. When a problem gets too difficult for me, he always offers a talk that indeed clears my mind. I really appreciate the efficient, calm and systematic way he works at the beamline. I am genuinely thankful for Christian's unselfish and resolute support that has saved our lives at a beamtime in so many situations.

I want to thank *Erik Gührs* for his special support regarding the bit-patterned media project. With him I had the joy of manually going through all the images and recording the magnetic state of every single island. I want to also acknowledge the help of *Stefan Schaffert*. When time was getting short, he was there to assist me in performing simulations and producing figures for our publication. It is always fun to be in company with Erik or Stefan at the beamline. Both Erik and Stefan are known for being always ready to help and for taking responsibility.